Year : 2014

Time-lapse and probabilistic inversion strategies for plane-wave electromagnetic data

CARBAJAL MARINA ANDREA ROSAS

UNIL | Université de Lausanne

Faculté des géosciences et de l'environnement
Institut des Sciences de la Terre

Time-lapse and probabilistic inversion strategies for plane-wave electromagnetic data

Thèse de doctorat

Présentée à la
Faculté des géosciences et de l'environnement de
l'Université de Lausanne

par

MARINA ANDREA ROSAS CARBAJAL

Geophysicist
National University of La Plata (Argentina)

Jury

Prof. Dr. René Véron, Président
Prof. Dr. Niklas Linde, Directeur de thèse
Prof. Dr. Juan José Ledo, Expert
Prof. Dr. Klaus Holliger, Expert

Lausanne, 2014

UNIL | Université de Lausanne
Décanat Géosciences et de l'Environnement
bâtiment Géopolis
CH-1015 Lausanne

IMPRIMATUR

Vu le rapport présenté par le jury d'examen, composé de

Président de la séance publique :	M. le Professeur René Véron
Président du colloque :	M. le Professeur René Véron
Directeur de thèse :	M. le Professeur Niklas Linde
Expert interne :	M. le Professeur Klaus Holliger
Expert externe :	M. le Professeur Juan José Ledo

Le Doyen de la Faculté des géosciences et de l'environnement autorise l'impression de la thèse de

Madame Marina A. ROSAS CARBAJAL

Titulaire d'un
Licenciate in Geophysics
Universidad Nacional de La Plata

intitulée

TIME-LAPSE AND PROBABILISTIC INVERSION STRATEGIES FOR PLANE-WAVE ELECTROMAGNETIC DATA

Lausanne, le 9 décembre 2014

Pour le Doyen de la Faculté des géosciences et de l'environnement

Professeur René Véron, Vice-doyen

Dedicated to my father

Contents

Résumé

L'utilisation efficace des systèmes géothermaux, la séquestration du CO_2 pour limiter le changement climatique et la prévention de l'intrusion d'eau salée dans les aquifères costaux ne sont que quelques exemples qui démontrent notre besoin en technologies nouvelles pour suivre l'évolution des processus souterrains à partir de la surface. Un défi majeur est d'assurer la caractérisation et l'optimisation des performances de ces technologies à différentes échelles spatiales et temporelles. Les méthodes électromagnétiques (EM) d'ondes planes sont sensibles à la conductivité électrique du sous-sol et, par conséquent, à la conductivité électrique des fluides saturant la roche, à la présence de fractures connectées, à la température et aux matériaux géologiques. Ces méthodes sont régies par des équations valides sur de larges gammes de fréquences, permettant détudier de manières analogues des processus allant de quelques mètres sous la surface jusqu'à plusieurs kilomètres de profondeur. Néanmoins, ces méthodes sont soumises à une perte de résolution avec la profondeur à cause des propriétés diffusives du champ électromagnétique. Pour cette raison, l'estimation des modèles du sous-sol par ces méthodes doit prendre en compte des informations a priori afin de contraindre les modèles autant que possible et de permettre la quantification des incertitudes de ces modèles de façon appropriée.

Dans la présente thèse, je développe des approches permettant la caractérisation statique et dynamique du sous-sol à l'aide d'ondes EM planes. Dans une première partie, je présente une approche déterministe permettant de réaliser des inversions répétées dans le temps (time-lapse) de données d'ondes EM planes en deux dimensions. Cette stratégie est basée sur l'incorporation dans l'algorithme d'informations a priori en fonction des changements du modèle de conductivité électrique attendus. Ceci est réalisé en intégrant une régularisation stochastique et des contraintes flexibles par rapport à la gamme des changements attendus en utilisant les multiplicateurs de Lagrange. J'utilise des normes différentes de la norme l_2 pour contraindre la structure du modèle et obtenir des transitions abruptes entre les régions du model qui subissent des changements dans le temps et celles qui n'en subissent pas. Aussi, j'incorpore une stratégie afin d'éliminer les erreurs systématiques de données time-lapse. Ce travail a mis en évidence l'amélioration de la caractérisation des changements temporels par rapport aux approches classiques qui réalisent des inversions indépendantes à chaque pas de temps et comparent les modèles.

Dans la seconde partie de cette thèse, j'adopte un formalisme bayésien et je teste la possibilité de quantifier les incertitudes sur les paramètres du modèle dans l'inversion d'ondes EM planes. Pour ce faire, je présente une stratégie d'inversion probabiliste basée sur des pixels à deux dimensions pour des inversions de données d'ondes EM planes et de tomographies de résistivité électrique (ERT) séparées et jointes. Je compare les incertitudes des paramètres du modèle en considérant différents types d'information a priori sur la structure du modèle et différentes fonctions de vraisemblance pour décrire les erreurs sur les données. Les résultats indiquent que la régularisation du modèle est nécessaire lorsqu'on a à faire à un large nombre de paramètres car cela permet d'accélérer la convergence des chaînes et d'obtenir des modèles

plus réalistes. Cependent, ces contraintes mènent à des incertitudes d'estimations plus faibles, ce qui implique des distributions a posteriori qui ne contiennent pas le vrai modèledans les régions où la méthode présente une sensibilité limitée. Cette situation peut être améliorée en combinant des méthodes d'ondes EM planes avec d'autres méthodes complémentaires telles que l'ERT. De plus, je montre que le poids de régularisation des paramètres et l'écart-type des erreurs sur les données peuvent être retrouvés par une inversion probabiliste.

Finalement, j'évalue la possibilité de caractériser une distribution tridimensionnelle d'un panache de traceur salin injecté dans le sous-sol en réalisant une inversion probabiliste time-lapse tridimensionnelle d'ondes EM planes. Étant donné que les inversions probabilistes sont très coûteuses en temps de calcul lorsque l'espace des paramètres présente une grande dimension, je propose une stratégie de réduction du modèle où les coefficients de décomposition des moments de Legendre du panache de traceur injecté ainsi que sa position sont estimés. Pour ce faire, un modèle de résistivité de base est nécessaire. Il peut être obtenu avant l'expérience time-lapse. Un test synthétique montre que la méthodologie marche bien quand le modèle de résistivité de base est caractérisé correctement. Cette méthodologie est aussi appliquée à un test de traçage par injection d'une solution saline et d'acides réalisé dans un système géothermal en Australie, puis comparée à une inversion time-lapse tridimensionnelle réalisée selon une approche déterministe. L'inversion probabiliste permet de mieux contraindre le panache du traceur salin grâce à la grande quantité d'informations a priori incluse dans l'algorithme. Néanmoins, les changements de conductivités nécessaires pour expliquer les changements observés dans les données sont plus grands que ce qu'expliquent notre connaissance actuelle des phénomenès physiques. Ce problème peut être lié à la qualité limitée du modèle de résistivité de base utilisé, indiquant ainsi que des efforts plus grands devront être fournis dans le futur pour obtenir des modèles de base de bonne qualité avant de réaliser des expériences dynamiques.

Les études décrites dans cette thèse montrent que les méthodes d'ondes EM planes sont très utiles pour caractériser et suivre les variations temporelles du sous-sol sur de larges échelles. Les présentes approches améliorent l'évaluation des modèles obtenus, autant en termes d'incorporation d'informations a priori, qu'en termes de quantification d'incertitudes a posteriori. De plus, les stratégies développées peuvent être appliquées à d'autres méthodes géophysiques, et offrent une grande flexibilité pour l'incorporation d'informations additionnelles lorsqu'elles sont disponibles.

Abstract

The efficient use of geothermal systems, the sequestration of CO_2 to mitigate climate change, and the prevention of seawater intrusion in coastal aquifers are only some examples that demonstrate the need for novel technologies to monitor subsurface processes from the surface. A main challenge is to assure optimal performance of such technologies at different temporal and spatial scales. Plane-wave electromagnetic (EM) methods are sensitive to subsurface electrical conductivity and consequently to fluid conductivity, fracture connectivity, temperature, and rock mineralogy. These methods have governing equations that are the same over a large range of frequencies, thus allowing to study in an analogous manner processes on scales ranging from few meters close to the surface down to several hundreds of kilometers depth. Unfortunately, they suffer from a significant resolution loss with depth due to the diffusive nature of the electromagnetic fields. Therefore, estimations of subsurface models that use these methods should incorporate a priori information to better constrain the models, and provide appropriate measures of model uncertainty.

During my thesis, I have developed approaches to improve the static and dynamic characterization of the subsurface with plane-wave EM methods. In the first part of this thesis, I present a two-dimensional deterministic approach to perform time-lapse inversion of plane-wave EM data. The strategy is based on the incorporation of prior information into the inversion algorithm regarding the expected temporal changes in electrical conductivity. This is done by incorporating a flexible stochastic regularization and constraints regarding the expected ranges of the changes by using Lagrange multipliers. I use non-l_2 norms to penalize the model update in order to obtain sharp transitions between regions that experience temporal changes and regions that do not. I also incorporate a time-lapse differencing strategy to remove systematic errors in the time-lapse inversion. This work presents improvements in the characterization of temporal changes with respect to the classical approach of performing separate inversions and computing differences between the models.

In the second part of this thesis, I adopt a Bayesian framework and use Markov chain Monte Carlo (MCMC) simulations to quantify model parameter uncertainty in plane-wave EM inversion. For this purpose, I present a two-dimensional pixel-based probabilistic inversion strategy for separate and joint inversions of plane-wave EM and electrical resistivity tomography (ERT) data. I compare the uncertainties of the model parameters when considering different types of prior information on the model structure and different likelihood functions to describe the data errors. The results indicate that model regularization is necessary when dealing with a large number of model parameters because it helps to accelerate the convergence of the chains and leads to more realistic models. These constraints also lead to smaller uncertainty estimates, which imply posterior distributions that do not include the true underlying model in regions where the method has limited sensitivity. This situation can be improved by combining plane-wave EM methods with complimentary geophysical methods such as ERT. In addition, I show

that an appropriate regularization weight and the standard deviation of the data errors can be retrieved by the MCMC inversion.

Finally, I evaluate the possibility of characterizing the three-dimensional distribution of an injected water plume by performing three-dimensional time-lapse MCMC inversion of plane-wave EM data. Since MCMC inversion involves a significant computational burden in high parameter dimensions, I propose a model reduction strategy where the coefficients of a Legendre moment decomposition of the injected water plume and its location are estimated. For this purpose, a base resistivity model is needed which is obtained prior to the time-lapse experiment. A synthetic test shows that the methodology works well when the base resistivity model is correctly characterized. The methodology is also applied to an injection experiment performed in a geothermal system in Australia, and compared to a three-dimensional time-lapse inversion performed within a deterministic framework. The MCMC inversion better constrains the water plumes due to the larger amount of prior information that is included in the algorithm. The conductivity changes needed to explain the time-lapse data are much larger than what is physically possible based on present day understandings. This issue may be related to the base resistivity model used, therefore indicating that more efforts should be given to obtain high-quality base models prior to dynamic experiments.

The studies described herein give clear evidence that plane-wave EM methods are useful to characterize and monitor the subsurface at a wide range of scales. The presented approaches contribute to an improved appraisal of the obtained models, both in terms of the incorporation of prior information in the algorithms and the posterior uncertainty quantification. In addition, the developed strategies can be applied to other geophysical methods, and offer great flexibility to incorporate additional information when available.

Chapter 1

Introduction

1.1 Preface

Oil, natural gas and coal production are set to peak and start to decline within the next decades (Nelder, 2009). In Switzerland, 39.9% of the total production of electricity is generated from nuclear power but, after the Fukushima accident (e.g. www.world-nuclear.org, 2014), the federal government declared that nuclear power would be phased out gradually (www.swissworld.org, 2014). Existing nuclear power stations will continue to run as long as they are safe but will not be replaced. Novel technologies need to be developed to facilitate the switch in energy production from nuclear power and fossil fuels to renewable energy. Geothermal energy is one promising possibility to partially absorb the energy demand. Increasing interest exists in developing enhanced geothermal systems (Tester *et al.*, 2006) where fluids are pumped into the hot geological formations and recovered once they become hot enough to produce electricity (Fig. 1.1a). One significant complication in developing enhanced geothermal systems is to estimate where the injected fluids will flow.

There is currently a scientific and political interest in underground storage of CO_2 in geological formations as a geoengeneering approach to global climate change mitigation (Metz *et al.*, 2005). The approach consists in capturing CO_2 and storing it in the solid Earth or in ocean sediments (Fig. 1.1b) so that they do not contribute to the greenhouse effect. In coastal regions, it is imperative to monitor salt-water infiltration into freshwater aquifers used for potable or agricultural purposes (Fig. 1.1c). In areas with deteriorating or limited water resources, population pressure has also led to an increased demand for aquifer storage recovery (Fig. 1.1d), where excess freshwater is injected into subsurface aquifers for later recovery (e.g. during the dry season) with relatively small associated environmental costs.

All these engineering schemes involve fluid redistributions in geological formations on different temporal and spatial scales. One main geological and geophysical challenge is to assure optimal characterization and performance of such installations at varying resolutions, for different

geological formations, and budgets. In the case of enhanced geothermal systems, the main technique for monitoring reservoir development is microseismics (e.g. House, 1987), where tomographic techniques are used to locate earthquakes associated with fracture formation caused by hydraulic over-pressure. Note that the microseismic technique is not directly sensitive to fluid distribution nor to fracture connectivity.

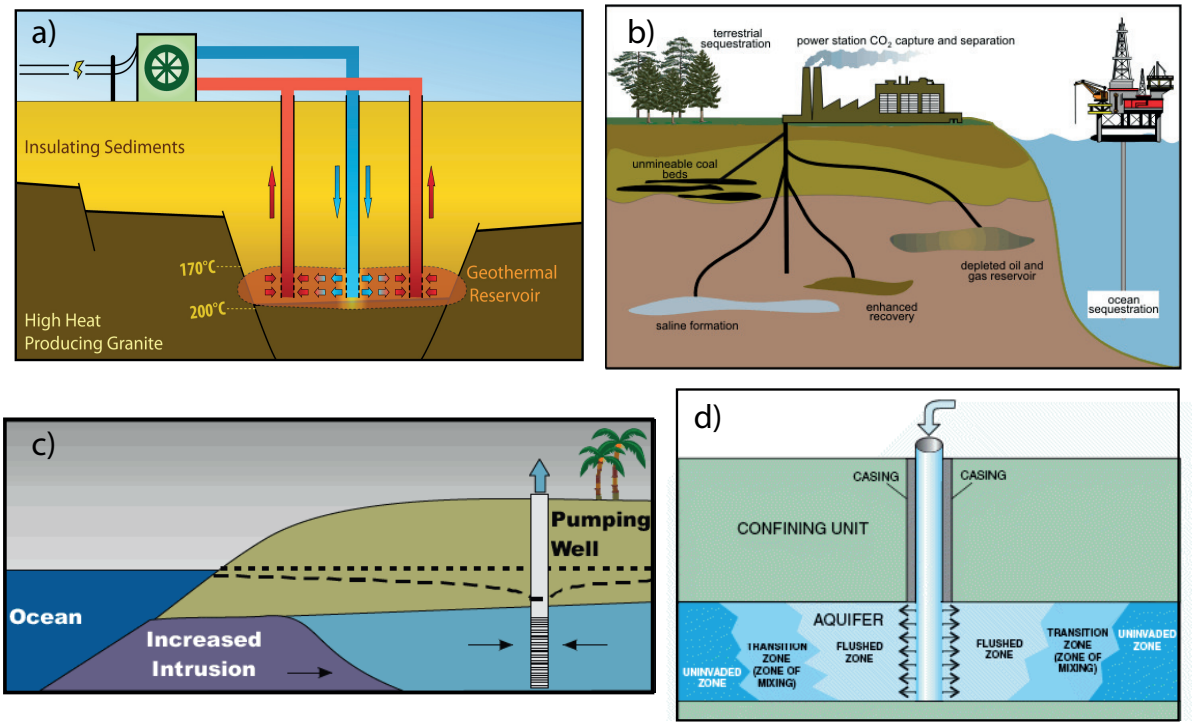

Figure 1.1: Examples of subsurface processes that require monitoring that could be addressed using plane-wave electromagnetic methods. (a) Injection and pumping in an enhanced geothermal system, adapted from Petratherm (2012). (b) CO_2 sequestration, adapted from www.e-education.edu (2014). (c) Seawater intrusion in a coastal aquifer, adapted from www.wrd.org (2007). (d) Aquifer storage recovery, adapted from USGS (2004).

Plane-wave electromagnetic methods are sensitive to the subsurface electrical conductivity distribution and consequently to fluid conductivity, temperature, fracture connectivity, and rock mineralogy. These methods have excellent scaling capabilities since the governing equations are the same over a large range of frequencies thus allowing to study, in an analogous manner, processes on scales ranging from few meters close to the surface down to several hundreds of kilometers depth. Unfortunately, they suffer from a significant resolution loss with depth due to the diffusive nature of the electromagnetic fields. Therefore, subsurface models inferred from these methods are not unique, and it is necessary to quantify the non-unicity by providing uncertainty estimates. This thesis aims at improving the inversion results of plane-wave electromagnetic methods, both as a means to characterize the static subsurface and as a monitoring tool. For this, I have conducted investigations related to the theory of the inverse problem, but I have also considered the particularities of this problem applied to plane-wave

electromagnetic methods. In the following, I provide a brief introduction of relevant studies previous to my work to better clarify the contributions of my thesis.

1.2 The inverse problem in geophysics

One of the aims in applied geophysics is to describe the structure and evolution of the Earth's subsurface from indirect measurements at its surface. For this purpose, different geophysical methods are used that are sensitive to different geophysical properties. The objective is thus to infer the spatial distribution of these properties from the collected data. Let the data be represented by a vector $\mathbf{d} = [d_1, d_2, ..., d_N]^{\mathrm{T}}$, where N is the number of data points collected and T denotes the transpose, and let the Earth be represented by a vector $\mathbf{m} = [m_1, m_2, ..., m_M]^{\mathrm{T}}$, where M is the number of model parameters used to describe the Earth. A set of equations which will be referred to as the physical model are used to relate these vectors,

$$\mathbf{d} = f(\mathbf{m}) + \mathbf{e}, \tag{1.1}$$

where $\mathbf{e}$ is a vector of dimension N that contains the measurement data errors and any errors in the physical model or its numerical implementation. The problem of predicting the data that would be measured provided explicit values of the model parameters is known as the *forward problem* and the predicted data is called the *forward response* of the model $\mathbf{m}$. The problem of finding the model $\mathbf{m}$ from the collected data $\mathbf{d}$ is called the *inverse problem*.

It is important to note that the choice of the model $\mathbf{m}$ used to represent the Earth is not unique. In practice, this model is chosen according to the physics of the problem under study, the amount of data that is available, and the available computational resources. The particular type of model used will be hereafter referred to as the model parameterization. For a given model parameterization, the number of model parameters used will be referred to as the degree of discretization or resolution of the model. For example, the three-dimensional electrical resistivity in the subsurface may be represented in terms of voxels with the model parameters being the constant values of electrical resistivity assigned to each voxel. Alternatively, it may be represented as continuous variations of electrical resistivity in terms of polynomials where the model parameters are the coefficients of these polynomials. These two types of model parameterizations will have a high or poor resolution depending on whether the size of the voxels (or the number of polynomial coefficients) used is small or large.

The type of model parameterization and discretization employed will influence the inversion results. In fact, there is a well known trade-off between the variance of the model parameters' estimates and the model resolution (Backus and Gilbert, 1970). The exact trade-off curve is problem-dependent, and a schematic representation is provided in Fig. 1.2.

Inverse problems can be classified into linear or non-linear inverse problems depending on the

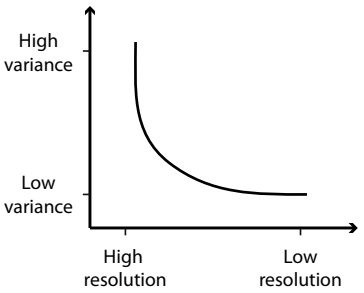

Figure 1.2: Typical trade-off between model resolution and variance for inverse problems. Adapted from Menke (1989).

properties of the physical model that links the model and the data. If this relation is linear, that is, if it can be written in the form

$$\mathbf{d} = \mathbf{F}\mathbf{m} + \mathbf{e}, \tag{1.2}$$

where $\mathbf{F}$ is a matrix of dimensions $N \times M$, then the inverse problem is said to be linear. Conversely, if this relation does not exist, the problem is said to be non-linear (see Eq. 1.1). More details about the characteristics of linear and non-linear inverse problems will be given in the following sections.

1.2.1 Static and time-lapse inversion

As previously stated, inverse problems are used to estimate model parameters describing the subsurface from a set of collected geophysical data. Here, a distinction can be made between problems where the model under study is assumed to be static, that is, where no relevant temporal changes are expected to occur, or time-lapse, where the interest is put in estimating the changes in subsurface properties over time. The types of approaches with which these two problems can be solved and the algorithms used to do so are common to both problems and they will be discussed together in the next section. However, a difference exists in the way data can be represented in the case of time-lapse inversions.

When monitoring temporal changes in subsurface properties, it is advantageous to leave the sensors in place during the monitoring period. The errors in the resulting time-lapse data for the same data sensor configuration are then likely to share a repeatable systematic component, which can be largely removed using a time-lapse inversion strategy. Following LaBrecque and Yang (2001), the observed data can be described more specifically in terms of two different sources of errors:

$$\mathbf{d}_t = f(\mathbf{m}_t) + \mathbf{e}_{\text{sys}} + \mathbf{e}_{\text{r},t}, \tag{1.3}$$

where the subscript t refers to the time when the measurement was done, $\mathbf{e}_{\text{r},t}$ is a random measurement error that is varying in time and is thus different for each data set, and $\mathbf{e}_{\text{sys}}$ is a

systematic contribution that is present at all times. Systematic errors can be related to modeling errors, bias introduced by ground coupling problems or improperly calibrated sensors and geometrical errors (e.g., incorrect station positioning or profiles that are not perfectly aligned).

Time-lapse inversion algorithms can be defined in different ways but aim generally at removing the systematic error contribution to improve the estimates of changes in subsurface properties. In a first step, the model at $t = 0$, $\mathbf{m}_0$, is obtained by means of a standard inversion (see section 1.2.2) using the data acquired before any perturbation to the system. This model is referred to as the base model in the following. Next, the residuals $\mathbf{r}_0 = \mathbf{d}_0 - f(\mathbf{m}_0) = \mathbf{e}_{\text{sys}} + \mathbf{e}_{\text{r},0}$, are removed from the data acquired at all subsequent times:

$$\tilde{\mathbf{d}}_t = \mathbf{d}_t - \mathbf{r}_0 = f(\mathbf{m}_t) + \mathbf{e}_{\text{r},t} - \mathbf{e}_{\text{r},0}. \tag{1.4}$$

Since the systematic component has been removed by differencing, the new corrected data sets have the advantage of being less error contaminated provided that the standard deviations of the different error sources satisfy $\sigma_{sys} > \sqrt{\sigma_{r,0}^2 + \sigma_{r,t}^2}$ (e.g. Doetsch *et al.*, 2010). In the next sections, a general symbol for the errors $\mathbf{e}$ and the data $\mathbf{d}$ is kept for the sake of simplicity, but it should be noticed that these could refer to either the static or time-lapse cases.

1.2.2 Deterministic inversion

Linear problem

There are two main approaches to tackle an inverse problem. One is the deterministic approach, in which the "best" estimate of the model parameters is sought and where different criteria for what is "best" may apply. The other one is the probabilistic approach, which is based on Bayes theorem and aims at finding the posterior probability density function (pdf) of the model parameters and, therefore, a complete description of the model parameters' uncertainty. Each of these approaches have their own advantages and disadvantages which will be briefly discussed.

The deterministic approach aims at finding a unique set of model parameters that satisfies a premise about what the optimal model should be. The most simple premise is to minimize the data errors, that is, to find the model which best explains the measured data. Still, in order to minimize these errors, a measure of distance or length has to be defined. The most common practice is to use the Euclidean distance, also referred to as the l_2-norm, to measure the distance between the data and the forward response of the model. Considering a linear inverse problem (see Eq. 1.2) with $\mathbf{C}_d$ being the data covariance matrix, an l_2-norm minimization of the errors weighted by the covariance matrix leads to the solution of the classical method of least squares:

$$\mathbf{m}_{est} = (\mathbf{F}^{\mathrm{T}}\mathbf{C}_d^{-1}\mathbf{F})^{-1}\mathbf{F}^{\mathrm{T}}\mathbf{C}_d^{-1}\mathbf{d}, \tag{1.5}$$

where usually errors are assumed to be uncorrelated and $\mathbf{C}_d^{-1} = \text{diag}[\sigma_1^{-2}, ..., \sigma_N^{-2}]$. In most practical cases, the inverse problem is under-determined, which means that the inverse of the matrix $(\mathbf{F}^{\mathrm{T}}\mathbf{F})$ is not uniquely determined. When this happens, it is necessary to add more information to the problem before it can be solved. In practice, this implies specifying that one seeks a particular "type" of model in the space of models that can explain the data. Because the incorporation of constraints helps to regularize the inverse problem in the sense that a unique solution can be found, this constraining of the inverse problem is often called *model regularization*. In terms of the mathematical problem, it means no longer minimizing the error length but an objective function that combines the error with a term that involves the model regularization (Tikhonov, 1963):

$$W_\lambda(\mathbf{m}) = \mathbf{u}^{\mathrm{T}}\mathbf{u} + \lambda^{-1}\mathbf{w}^{\mathrm{T}}\mathbf{w}, \tag{1.6}$$

$\mathbf{u}$ is the model regularization, $\mathbf{w} = \mathbf{C}_d^{-0.5}(\mathbf{d} - f(\mathbf{m}))$, and λ is a trade-off parameter defining the relative weight between the data fitting and the model regularization. The information about the model added in the model regularization is independent of the collected data and usually reflects a preconceived idea of the model, prior to the inversion. It is therefore usually referred to as *prior information*. The regularization may force the model estimates to be close to a reference model by making $\mathbf{u} = \mathbf{m} - \mathbf{m}_{ref}$. This constraint is referred to as "damping". Another popular constraint forces the models to be "simple", in the sense that spatial changes in the model properties should be smooth. This type of models are found by penalizing the gradient of the model parameters $\mathbf{u} = \mathbf{D}\mathbf{m}$, where $\mathbf{D}$ is the difference operator. Maurer *et al.* (1998) showed that these cases are the two extremes of a range of regularization schemes that impose stochastic properties on inverted models. In the case of a general covariance matrix $\mathbf{C}_m$ used to describe the preconceived properties of the model, with respect to a reference model $\mathbf{m}_{ref}$ and using an l_2-norm as a measure of length, the solution to the linear problem is given by (e.g. Menke, 1989)

$$\mathbf{m}(\lambda) = (\mathbf{F}^{\mathrm{T}}\mathbf{C}_d^{-1}\mathbf{F} + \lambda\mathbf{C}_m^{-1})^{-1}\mathbf{F}^{\mathrm{T}}\mathbf{C}_d^{-1}(\mathbf{d} - \mathbf{F}\mathbf{m}_{ref}) + \mathbf{m}_{ref}. \tag{1.7}$$

When the inverse problem is non-linear, the deterministic strategy is to iteratively linearize the problem by performing a Taylor's expansion of the forward operator, $\mathbf{F}[\mathbf{m}] \simeq \mathbf{F}[\mathbf{m}_{ref}] + \mathbf{J}(\mathbf{m} - \mathbf{m}_{ref})$, where $\mathbf{J}$ is the sensitivity matrix or Jacobian matrix. Using this approximation to minimize Eq. 1.6 with an l_2-norm, an iterative solution can be found, for example, using a Gauss-Newton approach (e.g. Parker, 1994):

$$\mathbf{m}_{k+1}(\lambda) = (\mathbf{J}_k^{\mathrm{T}}\mathbf{C}_d^{-1}\mathbf{J}_k + \lambda\mathbf{C}_m^{-1})^{-1}\mathbf{J}_k^{\mathrm{T}}\mathbf{C}_d^{-1}\hat{\mathbf{d}}_k + \mathbf{m}_{ref}, \tag{1.8}$$

where $\hat{\mathbf{d}}_k = \mathbf{d} - \mathbf{F}[\mathbf{m}_k] + \mathbf{J}_k\Delta\mathbf{m}_k$, $\Delta\mathbf{m}_k = \mathbf{m}_k - \mathbf{m}_{ref}$, and the subscripts k and $k+1$ denote the previous and present iterations. Alternatively, the non-linear conjugate gradient algorithm (e.g. Tarantola, 1987; Nocedal and Wright, 2006) can be used which does not require the computation and storage of the Jacobian matrix at each iteration. Independently of the local

descent method used to solve the problem, a *starting model* is necessary to initialize the iterative process of finding a best estimate. This starting model, which is often chosen to be the same as the reference model, should ideally be close to the global minimum of Eq. 1.6, otherwise the iterative solution risks to converge to a local minimum only. Figure 1.3 illustrates this problem.

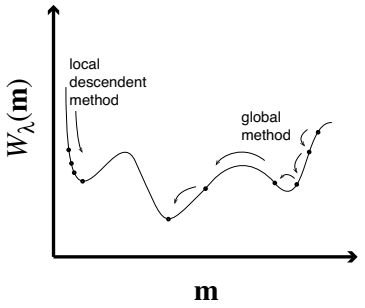

Figure 1.3: Local descendent methods can get trapped in local minima of the non-linear objective function $W_\lambda(\mathbf{m})$ (see Eq. 1.6) when an improper starting model is used . Global methods can "jump" out of the local minima. Adapted from Everett (2013).

Given a proper starting model, minimum values of Eq. 1.6 can be found for fixed λ. However, finding a proper λ is not easy. First, a desired level to which the data should be fitted has to be chosen. Based on the definition of $\mathbf{w}$ and using an l_2-norm, the root mean square (RMS) misfit:

$$\text{RMS} = \sqrt{\frac{1}{N}\sum_{1\leq n\leq N} w_n^2}, \tag{1.9}$$

is usually used to represent the data fit. The RMS should be close to 1 for a Gaussian distribution of errors. Then, to obtain a solution with minimum structure at a desired misfit, one needs to solve Eq. 1.6 for different values of λ and compare the results.

Occam's inversion

Constable *et al.* (1987) proposed an alternative approach so that λ does not need to be determined by trial and error. The approach consists in the minimization of the cost function

$$W_\lambda(\mathbf{m}) = \mathbf{u}^{\mathrm{T}}\mathbf{u} + \lambda^{-1}(\mathbf{w}^{\mathrm{T}}\mathbf{w} - \chi^*), \tag{1.10}$$

where χ^* is an a priori acceptable fit of the model parameters, often chosen as the number of data N since this is the expected value of $\mathbf{w}^{\mathrm{T}}\mathbf{w}$ when the errors follow a Gaussian distribution. Constable *et al.* (1987) proposed an iterative solution similar to the Gauss-Newton algorithm in Eq. 1.8, but incorporating a line search for the optimum value of λ at each iteration. During the first iterations, λ is chosen to reduce the misfit. When the desired misfit level is reached,

λ is chosen to maximize the weight of the regularization to find the smoothest possible model that can fit the data.

Iteratively reweighted least squares algorithm

Using the l_2-norm to quantify model structure, as in Occam inversion, strongly penalizes the spatial transitions of model properties over a number of model cells. This has the disadvantage that the models obtained may be unrealistically smooth (e.g. Ellis and Oldenburg, 1994; Farquharson, 2007). Likewise, the use the l_2-norm to quantify the data fit is very sensitive to the presence of outliers in the error distributions because of the large penalization applied for differences between the data and the model that, weighted by the standard deviation, are larger than 1. Iteratively reweighted least squares (IRLS) algorithms make it possible to use non l_2-norms both on model structure and data misfit quantification, while still solving a linear system at each iteration step (Last and Kubik, 1983; Portniaguine and Zhdanov, 1999; Pilkington, 1997; Farquharson and Oldenburg, 1998; Farquharson, 2007; Ajo-Franklin *et al.*, 2007). These algorithms rely on a least-square formulation similar to Eq. (1.8), but with the difference that reweighting matrices are defined after each iteration to approximate a given norm. This results in algorithms with similarly fast convergence characteristics as classical least-squares formulations, but allowing to resolve sharp interfaces and/or better assimilating the error outliers. The update to the IRLS solution of a non-linear inverse problem can be generalized as (e.g., Farquharson and Oldenburg, 1998; Menke, 1989; Siripunvaraporn and Egbert, 2000):

$$\begin{aligned}\mathbf{m}_{k+1}(\lambda) = \left[\left(\mathbf{C}_d^{-0.5}\mathbf{J}_k\right)^{\mathrm{T}}\mathbf{R}_{d,k}\mathbf{C}_d^{-0.5}\mathbf{J}_k + \lambda\left(\mathbf{C}_m^{-0.5}\right)^{\mathrm{T}}\mathbf{R}_{m,k}\mathbf{C}_m^{-0.5}\right]^{-1}\times \\ \left(\mathbf{C}_d^{-0.5}\mathbf{J}_k\right)^{\mathrm{T}}\mathbf{R}_{d,k}\mathbf{C}_d^{-0.5}\hat{\mathbf{d}}_k + \mathbf{m}_{\mathrm{ref}},\end{aligned} \tag{1.11}$$

where $\mathbf{R}_{i,k}$, $i = m, d$ is a reweighting matrix that is recalculated after each iteration and that depends on the chosen norm. Several norms have been tested in the literature, for which different expressions in $\mathbf{R}$ have to be used. Figure 1.4 shows the behavior of these norms for different scalar values of $\mathbf{u}$ or $\mathbf{w}$. Note that the l_2-norm is the one which increases the fastest for scalar values larger than 1. Applying non-l_2 norms makes it possible to obtain models with overall uniform regions separated by sharper interfaces.

Uncertainty estimates in deterministic inversion

Given a "best" model found by means of a deterministic inversion, a natural concern arises from the fact that the model was estimated using data that are error contaminated, and these errors propagate to the model estimate. A critical matter is therefore to quantify the uncertainty of estimated model parameters.

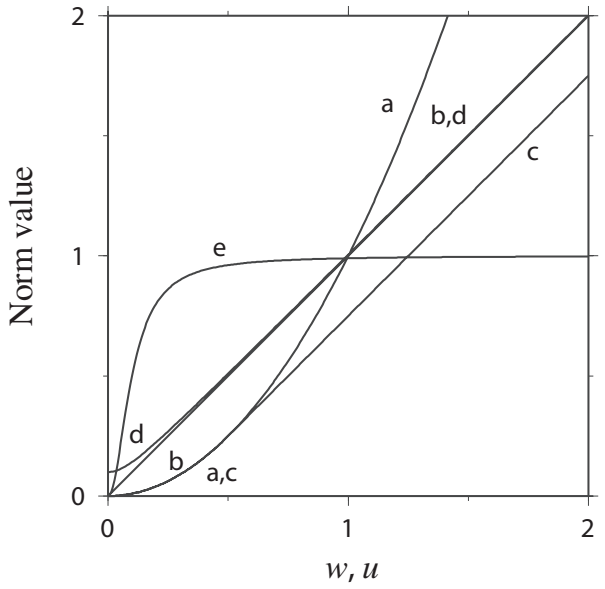

Figure 1.4: Behavior of different vector norms: (a) l_2-norm; (b) l_1-norm; (c) Huber M-measure; (d) Ekblom perturbed l_1-norm; and (e) support measure. Adapted from Farquharson (2007).

In the case of a linear over-determined inverse problem where errors follow a Gaussian distribution, the estimate of the model covariance matrix can be found by linear error propagation:

$$\mathbf{C}'_m = ((\mathbf{F}^{\mathrm{T}}\mathbf{F})^{-1}\mathbf{F}^{\mathrm{T}})\mathbf{C}_d((\mathbf{F}^{\mathrm{T}}\mathbf{F})^{-1}\mathbf{F}^{\mathrm{T}})^{\mathrm{T}} = \sigma_d^2(\mathbf{F}^{\mathrm{T}}\mathbf{F})^{-1}. \tag{1.12}$$

The situation is more difficult for non-linear inverse problems since a first order linearization is often insufficient to describe the complex dependence of the model with the data. Approximate uncertainty estimates can be obtained through linearization in the vicinity of the final model estimate (Alumbaugh and Newman, 2000). The uncertainty estimates are then highly dependent on this estimate, which in turn is an approximation of the solution due to linearization, and can be highly dependent on the starting model used. An alternative is to run repeated deterministic inversions using the same data set with different regularization constraints to obtain a collection of possible models (Oldenburg and Li, 1999). Features that appear in all models are interpreted as being well resolved by the data. A more formal approach is to construct extremal models that fit the data up to a given data misfit threshold with a most-squares inversion (Jackson, 1976; Meju and Hutton, 1992). This approach derives the extremal deviations of each model parameter from a best-fitting model.

The aforementioned methods partly account for model non-linearity but fail to provide formal uncertainty estimates. In fact, the inability to provide formal estimates of the model parameters' uncertainty is the most criticized aspect of deterministic inversion.

1.2.3 Probabilistic inversion

A different approach to solve inverse problems consists in considering a probabilistic framework and determining the posterior pdf of the model parameters (Tarantola and Valette, 1982). The application of Bayes theorem states that the posterior pdf of the model conditional on the data, $p(\mathbf{m}|\mathbf{d})$, is given by:

$$p(\mathbf{m}|\mathbf{d}) = \frac{p(\mathbf{m})p(\mathbf{d}|\mathbf{m})}{p(\mathbf{d})}, \tag{1.13}$$

where $p(\mathbf{d}|\mathbf{m})$ is the pdf of the data conditional on the model and is often referred to as likelihood function $L(\mathbf{m}|\mathbf{d})$, $p(\mathbf{m})$ is the model's prior pdf and $p(\mathbf{d})$ is the evidence. The evidence is needed when different model parameterizations and discretizations are considered (e.g. Malinverno, 2002). Otherwise, it is a constant and the following expression holds

$$p(\mathbf{m}|\mathbf{d}) \propto p(\mathbf{m})L(\mathbf{m}|\mathbf{d}). \tag{1.14}$$

The likelihood function is a measure of how well the model explains the data. The closer the values of $f(\mathbf{m})$ are to $\mathbf{d}$, the higher the likelihood. Under the assumption that the measurement data errors follow a normal distribution with zero mean, the likelihood function is given by (e.g., Tarantola, 2005)

$$L(\mathbf{m}|\mathbf{d}) = \frac{1}{(2\pi)^{N/2}\det(\mathbf{C}_d)^{1/2}} \exp\left(-\frac{1}{2}\left(f(\mathbf{m}) - \mathbf{d}\right)^{\mathrm{T}} \mathbf{C}_d^{-1} \left(f(\mathbf{m}) - \mathbf{d}\right)\right), \tag{1.15}$$

where $\det(\mathbf{C}_d)$ denotes the determinant of $\mathbf{C}_d$. The prior probability of the model vector, $p(\mathbf{m})$, represents the information known about the subsurface before collecting the actual data. It can be based on other types of geophysical measurements, geological information about the model structure, expected type of rocks and values of model parameters, etc. Thus, probabilistic inversion is based on the assumption that some information is known about the model, and the data will be used to update this information. Unfortunately, the availability of reliable prior information is not always granted and even more difficult is the task of translating this information into a formal pdf. Indeed, the use of the prior information is the most debated aspect of the probabilistic approach, since in practice, the prior pdf can be modified to retrieve models with particularly desired features (e.g. Scales and Sneider, 1997).

Markov chain Monte Carlo methods

In most practical applications, the posterior pdf cannot be derived analytically and it is necessary to extensively explore the space of possible models (Tarantola, 2005). Often times the number of model parameters is large and a simple grid search in this space becomes impossible. To solve these problems, random explorations methods often referred to as Monte Carlo (MC) methods have to be used. Let $g(\mathbf{m})$ be the desired probability distribution. The basic idea of MC methods is to randomly draw model proposals from a certain distribution over a sampling

space and obtain a collection of models that follows the distribution $g(\mathbf{m})$. A popular type of MC method, the rejection sampling or accept-reject method (Von Neumann, 1951), consists in providing an envelope function $ch(\mathbf{m})$, where c is a constant, of the desired distribution $g(\mathbf{m})$. The model proposals $\mathbf{m}_{\text{prop}}$ are drawn from the distribution h and are then "accepted" or "rejected" with a probability

$$P_{\text{accept}} = \frac{g(\mathbf{m}_{\text{prop}})}{ch(\mathbf{m}_{\text{prop}})}. \tag{1.16}$$

Provided enough samples, the set of accepted models will be distributed according to the desired distribution g. If the parameter space is low dimensional, MC simulation can provide a reasonable approximation of the posterior distribution pending that the ensemble of samples is sufficiently large. For higher dimensional spaces, exhaustive random sampling is inefficient, and more intelligent search methods, such as Markov chain Monte Carlo (MCMC) simulation, are required to speed up the exploration of the target distribution.

By definition, a MCMC method for the simulation of a distribution g is any method producing an ergodic Markov chain whose stationary distribution is g (Robert and Casella, 2004). The Markov property means that the "present" state of the chain depends on its immediate past state only. The stationary distribution is the distribution to which the Markov chain convergences and the ergodic property states that the stationary distribution does not depend on the chain's initial conditions. Therefore, the application of MCMC methods to probabilistic inversion consists in building Markov chains that converge to the posterior pdf of the model parameters.

A particular type of MCMC method is the Metropolis-Hastings algorithm (Metropolis and Ulam, 1949; Metropolis *et al.*, 1953; Hastings, 1970). This algorithm generates chains that sample the distribution g by drawing proposed chain states from a proposal distribution and "accepting" or "rejecting" these samples according to a probabilistic rule that involves the chain's immediate past state. At a given state $\mathbf{m}_{\text{old}}$, the proposal distribution $q(\mathbf{m}_{\text{new}}|\mathbf{m}_{\text{old}})$ proposes a new state $\mathbf{m}_{\text{new}}$. If

$$\frac{g(\mathbf{m}_{\text{new}})q(\mathbf{m}_{\text{old}}|\mathbf{m}_{\text{new}})}{g(\mathbf{m}_{\text{old}})q(\mathbf{m}_{\text{new}}|\mathbf{m}_{\text{old}})} \geq 1, \tag{1.17}$$

then the chain moves to the proposed state $\mathbf{m}_{\text{new}}$. If not, the proposal is not automatically rejected, but accepted with a probability equal to the ratio in the left side of Eq. 1.17. This can be summarized with an acceptance probability:

$$P_{\text{accept}}^{\text{old}\to\text{new}} = \min\left\{1, \frac{g(\mathbf{m}_{\text{new}})q(\mathbf{m}_{\text{old}}|\mathbf{m}_{\text{new}})}{g(\mathbf{m}_{\text{old}})q(\mathbf{m}_{\text{new}}|\mathbf{m}_{\text{old}})}\right\}. \tag{1.18}$$

In practice, a number α is drawn from a uniform distribution $\mathcal{U}[0,1]$ and compared to $P_{\text{accept}}^{\text{old}\to\text{new}}$. If $\alpha \leq P_{\text{accept}}^{\text{old}\to\text{new}}$, then the model $\mathbf{m}_{\text{new}}$ is accepted. Equation 1.18 is known as the Metropolis

rule.

It can be shown that the Metropolis-Hastings algorithm will asymptotically converge to samples of g. Note that an explicit expression for g is not necessary but only the possibility to calculate it for concrete models up to a normalizing constant. Thus, it is straightforward to adapt the Metropolis-Hastings algorithm to the inverse problem by making $g = p(\mathbf{m})L(\mathbf{m}|\mathbf{d}) \propto p(\mathbf{m}|\mathbf{d})$. To completely define a MCMC algorithm, it is necessary to (1) define the proposal distribution q, and (2) establish a "convergence test" to determine when an ensemble of the last X states of the chain follow the desired distribution. Mosegaard and Tarantola (1995) introduced an extended Metropolis algorithm, where it is not necessary to evaluate an explicit formulation of the prior $p(\mathbf{m})$ but only to generate proposals that follow the prior distribution thus making the acceptance probability:

$$P_{\text{accept}}^{\text{old}\rightarrow\text{new}} = \min\left\{1, \frac{L(\mathbf{m}_{\text{new}}|\mathbf{d})}{L(\mathbf{m}_{\text{old}}|\mathbf{d})}\right\}. \tag{1.19}$$

The acceptance rate of a MCMC algorithm is defined as the ratio of the number of models accepted over the number of models proposed. It is generally desirable to have proposal distributions that lead to acceptance rates between $20 - 50\%$ (e.g., Tarantola, 2005). Otherwise, if the acceptance rates are too large, the chain is inefficient at sampling other parts of the posterior (the proposed models are too close from each other). If it is too small, computer resources are misused in evaluating the forward response of models that are not going to be accepted (the proposed models are too far from each other).

Many convergence criteria exist depending on the particular MCMC algorithm used. When multiple Markov chains are run, Gelman and Rubin (1992) suggest to compare the statistics of the different chains. The variance of the model parameters are independently estimated for each chain using the last 50% (for example) of the chains' states. Chains that converged are expected to have perfectly matching distributions and should therefore provide equal variances for each model parameter. Gelman and Rubin (1992) compute ratios of the variance estimates among different chains for each model parameter, which are now often referred to as the Gelman-Rubin statistic. According to their criteria, when all the model parameters have Gelman-Rubin statistics smaller than 1.2, the chain can be stopped and the ensemble of models used to calculate these statistics are distributed according to the posterior pdf.

No linear approximations of the function $f(\mathbf{m})$ are required in MCMC methods. Rather, it is necessary that the forward solver is as fast as possible to allow for many forward response computations. Thus, probabilistic inversion not only quantifies joint and marginal parameter uncertainty but also provides a correct treatment of the non-linearity of the problem and effectively explores the space of possible model parameters. For this reason, it is often referred to as a global inversion method (see Fig. 1.3).

Adaptive Markov chain Monte Carlo methods

Even though MCMC methods have proven to be much more efficient than simple MC methods, they also suffer from the curse of dimensionality. This means that as the number of model parameters to estimate, (i.e. the dimension of the problem) increases, it becomes increasingly difficult to explore the complete space of the posterior pdf, thus leading to impractical computation times. Many variations of the Metropolis-Hastings algorithms exist, which aim at improving the proposal distributions in high dimensions. One of such strategies is the so-called multiple-try sampling (Liu *et al.*, 2000), where each Markov chain proposes more than 1 (typically 5; e.g. Laloy and Vrugt, 2012) models but accepts only one of those. Other strategies include the use of information about previous states of the chains to generate new proposals. These algorithms are known as adaptive MCMC algorithms (e.g. Robert and Casella, 2004). The use of previous states that are not the immediate past state of the chains implies that the Markov property does not hold any more. However, these algorithms can be shown to maintain detailed balance and ergodicity, which ensures their convergence to the desired posterior pdf (Roberts and Rosenthal, 2007; Laloy and Vrugt, 2012).

Global optimization methods

Other global search methods of stochastic nature, such as simulated annealing (Kirkpatrick *et al.*, 1983) and genetic algorithms (Holland, 1992), can be used in geophysical inverse problems (c.f. Sen and Stoffa, 1995). These methods fully account for the non-linear relation between model and data but are only concerned with finding the optimal model of a given objective function without recourse to estimating the underlying posterior parameter distribution. They can therefore be placed between the deterministic and probabilistic approaches for inversion. Post-processing of the sampled trajectories can provide some insights into model parameters' uncertainty, but this type of analysis lacks the statistical rigor of Bayesian approaches.

1.3 Subsurface characterization with electromagnetic methods

1.3.1 Electrical properties of rocks

Electromagnetic (EM) methods are applied to image the conductive and capacitive properties of the subsurface. These properties can be represented by a complex conductivity σ^*, a complex resistivity ρ^*, or a complex permittivity ε^*:

$$\sigma^* = \frac{1}{\rho^*} = i\omega\varepsilon^*, \tag{1.20}$$

where ω denotes the angular frequency and $i = \sqrt{-1}$. The underlying physical properties are the electrical conductivity σ [S/m], the electrical resistivity ρ [Ωm], and the electrical permittivity ε [F/m] (Lesmes and Friedman, 2005). Unfortunately there is not a direct correspondence

between rock types and their electrical properties since the latter depend on temperature, porosity, and fluid content, among others. A schematic representation of the variability of rocks' electrical properties can be observed in Fig. 1.5. Note the large range of variation of the electrical properties, which cover approximately 7 orders of magnitude.

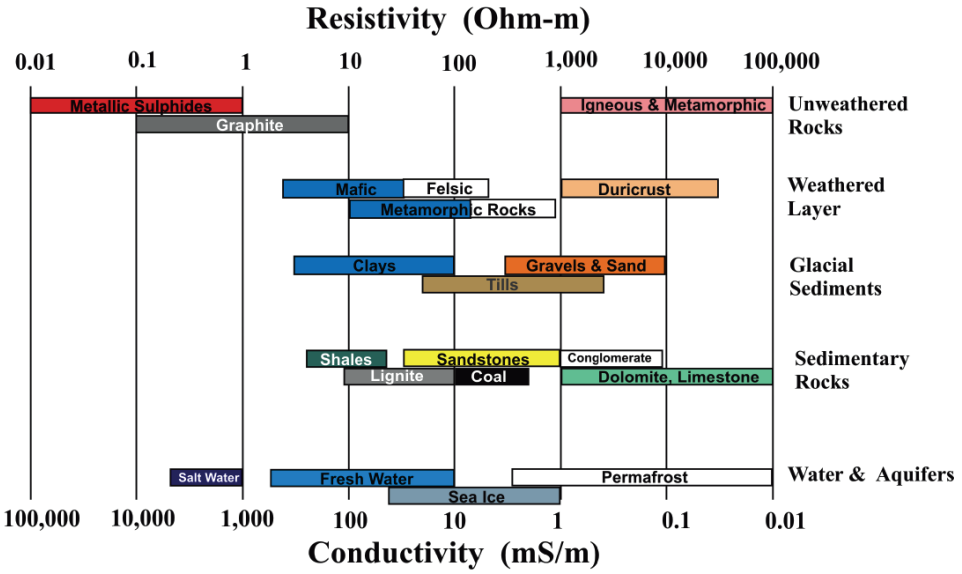

Figure 1.5: Typical electrical resistivity and conductivity values found for Earth materials. Adapted from Palacky (1988).

In the most general case, the electrical properties described in Eq. 1.20 are frequency dependent and anisotropic, that is, dependent on the direction they are measured, and are represented with a tensor (e.g. Martí, 2014). The electrical permittivity is often expressed in terms of a ratio:

$$\kappa = \frac{\varepsilon}{\varepsilon_0}, \tag{1.21}$$

where $\varepsilon_0 = 8.86 \times 10^{-12}$ F/m represents the vacuum permittivity.

1.3.2 Petrophysical relations

As previously mentioned, electrical properties of rocks depend on several factors. Although much effort has been put to identify universal laws that describe these dependences, the petrophysical relations used are often site- and scale-dependent. The most used relation continues to be Archie's law (Archie, 1942), which links the electrical conductivity to the rock porosity and fluid conductivity:

$$\sigma = \sigma_w \phi^m, \tag{1.22}$$

where σ_w is the fluid conductivity, ϕ the rock porosity, and m the cementation factor, which depends on the pores' connections. Different models have been proposed to extend Eq. 1.22 to account for partial fluid saturation and surface conductivity. One of this models is given by Linde *et al.* (2006):

$$\sigma = \phi^m (S_w^n \sigma_w + (\phi^{-m} - 1)\sigma_s), \tag{1.23}$$

where σ_s is the surface conductivity which is associated to the presence of clays, S_w is the fluid saturation, and n is the saturation exponent which depends on the geometry of the conductive phase. Since the fluid conductivity largely depends on the temperature, the rock conductivity is also dependent on this parameter. Sen *et al.* (1988) describe this dependence with an empirical formula. Also, a dependence with pressure arises from its influence on rock porosity or fracture aperture, when considering ϕ to be the volume of fractures relative to the total volume of rock (e.g. Brace *et al.*, 1965).

1.3.3 Electromagnetic geophysical methods

EM methods are sensitive to the electrical properties of the subsurface and they aim at characterizing changes in these properties by measuring one or more components of the electric and magnetic fields. The physics governing EM methods are completely described by Maxwell's equations:

$$\nabla \times \mathbf{E} = -\frac{\partial \mathbf{B}}{\partial t}, \tag{1.24a}$$

$$\nabla \times \mathbf{H} = \mathbf{j}_f - \frac{\partial \mathbf{D}}{\partial t}, \tag{1.24b}$$

$$\nabla . \mathbf{B} = 0, \tag{1.24c}$$

$$\nabla . \mathbf{D} = q_f\,, \tag{1.24d}$$

where $\mathbf{E}$ [V/m] is the electric field intensity, $\mathbf{B}$ [T] is the magnetic induction, $\mathbf{H}$ [A/m] is the magnetic field intensity, $\mathbf{D}$ [C/m^2] is the dielectric displacement, $\mathbf{j}_f$ [A/m^2] is the electric current density due to free charges and q_f [C/m^3] the electric charge density due to free charges.

The sensitivity of EM methods to electrical properties can be used at a wide range of spatial scales. This results in many EM techniques that are more or less suitable for each relevant scale, from borehole (i.e. well logging) to airborne and marine measurements. In the next section only on-land EM methods of relevance to this thesis are discussed. For a comprehensive description of other EM methods the reader is referred to Nabighian and Corbett (1988).

Plane-wave electromagnetic methods

Plane-wave EM methods use EM source fields that are distant to the measurement points and thus can be approximated as uniform, plane-polarized EM waves which impact the Earth's

surface with near vertical incidence (Cagniard, 1953). These methods also assume that displacement currents are negligible compared to time-varying conduction currents, which implies that the second term on the right side of Eq. 1.24b is zero.

For linear, isotropic media the following constitutive equations hold:

$$\mathbf{B} = \mu\mathbf{H}, \tag{1.25a}$$

$$\mathbf{D} = \varepsilon\mathbf{E}, \tag{1.25b}$$

$$\mathbf{j} = \sigma\mathbf{E}, \tag{1.25c}$$

where Eq.1.25c is Ohm's law. Assuming that variations in the electrical permittivities and magnetic permeabilities are negligible compared to variations in bulk rock conductivities, free-space values can be used for μ and ε.

Maxwell's equations can be rearranged when considering the aforementioned assumptions leading to diffusion equations for $\mathbf{B}$ and $\mathbf{E}$ (Jackson, 1962). In the particular case of a homogeneous half-space these can be written as:

$$(\nabla^2 - k^2)\mathbf{B} = 0 \tag{1.26a}$$

$$(\nabla^2 - k^2)\mathbf{E} = 0, \tag{1.26b}$$

where $k^2 = i\omega\mu\sigma$. These equations have solutions of the type:

$$\mathbf{B} = \mathbf{B}_0 e^{-i\mathbf{k}z} + \mathbf{B}_1 e^{i\mathbf{k}z}, \tag{1.27a}$$

$$\mathbf{E} = \mathbf{E}_0 e^{-i\mathbf{k}z} + \mathbf{E}_1 e^{i\mathbf{k}z}, \tag{1.27b}$$

where z denotes the vertical coordinate. Since the fields have to vanish when $z \to \infty$, $\mathbf{E}_1 = \mathbf{B}_1 = 0$ and Eqs. 1.27a and 1.27b become

$$\mathbf{B} = \mathbf{B}_0 e^{-i\mathbf{k}z} = \mathbf{B}_0 e^{-ivz} e^{-vz}, \tag{1.28a}$$

$$\mathbf{E} = \mathbf{E}_0 e^{-i\mathbf{k}z} = \mathbf{E}_0 e^{-ivz} e^{-vz}, \tag{1.28b}$$

where $\mathbf{E}_0$ and $\mathbf{B}_0$ are the EM fields at the Earth's surface and $v = \sqrt{\frac{\omega\mu\sigma}{2}}$. Thus, both fields vary sinusoidally with depth (e^{-ivz}) but are also attenuated (e^{-vz}). From the attenuating exponent a skin depth can be calculated as the depth at which the amplitude of the fields are reduced by $1/e$:

$$\delta = \sqrt{\frac{2}{\omega\mu\sigma}}. \tag{1.29}$$

This equation can be approximated using the magnetic permeability of free space $\mu_0 = 4\pi 10^{-7}$ Hm^{-1}, which leads to the following skin depth in meters:

$$\delta(T) \approx 500\sqrt{T\rho}, \tag{1.30}$$

where ρ is the resistivity of the half-space and T the wave period.

Considering the plane-wave EM assumptions in the more general case of isotropic conductivity varying in three dimensions leads to the following general relation between the **E** and **B** fields (Cantwell, 1960):

$$\begin{bmatrix} E_x(\omega) \\ E_y(\omega) \end{bmatrix} = \begin{bmatrix} Z_{xx}(\omega) & Z_{xy}(\omega) \\ Z_{yx}(\omega) & Z_{yy}(\omega) \end{bmatrix} \begin{bmatrix} H_x(\omega) \\ H_y(\omega) \end{bmatrix}, \tag{1.31}$$

where $\mathbf{E}_h(\omega) = [E_x(\omega), E_y(\omega)]^{\mathrm{T}}$ is the horizontal electric field, $\mathbf{H}_h(\omega) = [H_x(\omega), H_y(\omega)]^{\mathrm{T}}$ the horizontal magnetic field, and $\mathbf{Z}(\omega)$ the impedance tensor or transfer function. Apparent resistivities $\rho_{ij}^{\mathrm{app}}(\omega)$ and impedance phases $\varphi_{ij}^{\mathrm{app}}(\omega)$ can be obtained from the impedance components:

$$\rho_{ij}^{\mathrm{app}}(\omega) = \frac{1}{\omega\mu_0}|Z_{ij}(\omega)|^2, \tag{1.32}$$

$$\varphi_{ij}^{\mathrm{app}}(\omega) = \arctan\left(\frac{\mathrm{Im}Z_{ij}(\omega)}{\mathrm{Re}Z_{ij}(\omega)}\right), \tag{1.33}$$

where ij denote any combination of the horizontal components x and y. Also, a geomagnetic transfer function (so-called tipper pointer) **T** relates the vertical and horizontal magnetic fields as

$$\begin{bmatrix} H_z(\omega) \end{bmatrix} = \begin{bmatrix} A(\omega) & B(\omega) \end{bmatrix} \begin{bmatrix} H_x(\omega) \\ H_y(\omega) \end{bmatrix} = \mathbf{T}^{\mathrm{T}} \begin{bmatrix} H_x(\omega) \\ H_y(\omega) \end{bmatrix}. \tag{1.34}$$

Table 1.1 summarizes particular forms of the impedance tensor for different electrical conductivity distribution dimensionalities. Note that for two-dimensional conductivity models Maxwell's equations can be decoupled into two independent modes for an appropriate rotation of the coordinate system: transverse-electric (TE) and transverse-magnetic (TM) (e.g., Zhang *et al.*, 1987). Current flows parallel to the strike direction in the TE mode and perpendicular to it in the TM mode.

Although different types of plane-wave EM methods exist, the equations governing them are the same and the differences are given by the nature of the source they use and the frequency range considered. Table 1.2 summarizes these differences.

The magnetotelluric (MT) method (Vozoff, 1991; Chave and Jones, 2012) is the oldest among plane-wave EM methods. It uses natural fluctuations of the magnetic field of external (solar

wind-magnetosphere interaction) and internal (meteorological activity such as lightning discharges) origin as sources, and is therefore a passive method. Due to weak source fields at frequencies higher than 1kHz, the method is rarely used above this frequency. The name audio magnetotellurics (AMT) is often used for measurements at the highest frequencies (between 10 Hz and 1KHz). The three components of the magnetic field and the horizontal components of the electric field are usually measured, from which the transfer functions in Eqs. 1.31 and 1.34 are estimated.

The controlled source audio magnetotelluric (CSAMT) method (Goldstein and Strangway, 1975; Zonge *et al.*, 1991) uses a grounded dipole source to compensate the low energy frequency range found in natural sources. Provided that the source is sufficiently far away from the receivers, the plane-wave assumption is valid for this technique. Some studies suggest that a 4 skin depths distance should be sufficient (e.g., Goldstein and Strangway, 1975), but up to 20 skin depths may be necessary in the case a conductive layer overlaying a resistive body (Wannamaker, 1997).

The original very low frequency (VLF) method (Paal, 1965) measures the magnetic field tilt-angle or the vertical or horizontal magnetic field strengths created by VLF radio transmitters in the range 15-25 kHz. These measurements provide information about lateral variations of conductivity. The VLF resistivity (VLF-R) method uses the same VLF sources but also measures one or two electric field components, which can be used to estimate apparent resistivity and phase.

Finally, the radio magnetotelluric (RMT) method extends the use of VLF radio transmitters to long wave radio transmitters, thus covering a wider frequency range of 10-250 kHz. Usually displacement currents are neglected even for the highest frequencies used, however, some studies (e.g., Linde and Pedersen, 2004a; Kalscheuer *et al.*, 2008) suggest that these should be taken into account in presence of highly resistive ($\rho \geq 3000\ \Omega m$) media.

Table 1.1: Impedance tensor components for different electrical conductivity distribution dimensionalities. Conductivity is assumed isotropic.

	Dimensionality		
	1-D	2-D	3-D
Tensor components	$Z_{xx} = Z_{yy} = 0$ $Z_{xy} = -Z_{yx}$	$Z_{xx} = -Z_{yy}$ $Z_{xy} \neq -Z_{yx}$	$Z_{xx} \neq -Z_{yy}$ $Z_{xy} \neq -Z_{yx}$

Table 1.2: Summary of on land plane-wave electromagnetic methods. Modified from Bastani (2001).

Method	Source type	Frequency range	Application
MT	Natural	10^{-4} Hz - 1 kHz	Shallow crustal to lithosphere studies
CSAMT	Artificial controlled source	10^{-1} Hz - 100 kHz	Shallow environmental to deep crustal studies
Conventional VLF	VLF transmitters	15-25 kHz	Mapping structures
VLF resistivity	VLF transmitters	15-25 kHz	Low resolution shallow sounding
RMT	VLF and Radio transmitters	10-250 kHz	Shallow sounding for engineering and environmental studies

Forward modeling for plane-wave EM methods

The equations describing the link between the measured EM fields and the subsurface conductivity (Eqs. 1.24a, 1.24b, 1.24c, 1.24d) cannot be solved analytically for arbitrarily complex subsurface conductivity models. Here, a brief description of the most common methods used to predict the forward response of subsurface conductivity models is presented.

There are three essential approaches to numerically solve Maxwell's equations in an accurate manner: the finite difference approach, the finite element approach, and the integral equation approach (e.g. Avdeev, 2005). The finite difference approach consists in discretizing the three-dimensional domain in rectangular cuboids and approximating Maxwell's differential equations by their finite difference counterparts. It is arguably the most used approach to model EM forward responses, probably due to its relatively simple implementation. Examples of the finite difference approach applied to plane-wave EM in two-dimensions are given by Rodi (1976); Smith and Booker (1991); Siripunvaraporn and Egbert (2000) and Kalscheuer *et al.* (2010), and Mackie *et al.* (1993); Siripunvaraporn *et al.* (2005) and Egbert and Kelbert (2012) in three-dimensions.

In the finite element approach more flexibility is given to the model parameterization, which can be based on "unstructured" meshes that are particularly helpful to model topography. The downside of these methods is that they are more complicated to implement and computing times are usually longer. Examples of finite element plane-wave EM forward solvers with structured meshes are given by Wannamaker and Stodt (1987) in two dimensions and by Zyserman and Santos (2000) in three dimensions. Unstructured meshes for plane-wave EM modeling were presented not so long ago in two dimensions (e.g. Key and Weiss, 2006; Franke *et al.*, 2007) and even more recently in the three-dimensional case (e.g. Ren *et al.*, 2013).

Finally, the integral equation approach involves transforming Maxwell's differential equations

into integral equations by applying the Green's function technique and solving only for the anomalous field (e.g. Avdeev, 2005). In this formulation only the anomalous body needs to be discretized, but its implementation is challenging. Some examples of forward solvers using integral equations in three dimensions are given by Wannamaker *et al.* (1984), Wannamaker (1991), and Avdeev (2007).

Inversion of plane-wave EM data

The Occam inversion algorithm presented in section 1.2 was originally conceived to invert plane-wave EM data for one-dimensional cases where the subsurface properties vary only with depth. The method was then extended for two dimensions (deGroot Hedlin and Constable, 1990). Siripunvaraporn and Egbert (2000) introduced a more efficient formulation to avoid the large amount of memory and time needed to do operations with the Jacobian matrix. This method uses a Gauss-Newton approach in the so-called data space, which is made possible by a change of variables in the minimization problem. This allows to reduce the size of the matrices handled and thus requires less computing time and memory. The same technique was then applied for three-dimensional inversion by Siripunvaraporn *et al.* (2005). An alternative version of the two-dimensional code published by Siripunvaraporn and Egbert (2000) was developed by Kalscheuer *et al.* (2010). This algorithm applies object-oriented programming and dynamic allocation of variables, thus making it computationally efficient. Note that all the inversion algorithms mentioned thus far are freely available either from a website or upon request to the authors.

Rodi and Mackie (2001) and Newman and Alumbaugh (2000) presented two- and three-dimensional inversion algorithms, respectively, of plane-wave EM data based on the non-linear conjugate gradient method. Despite the progress that these algorithms represented in terms of speed, they require massively parallel computing architecture (Avdeev, 2005). Recently, Egbert and Kelbert (2012) presented a modular system grouping several inversion schemes for EM methods. This code makes it possible to choose between non-linear conjugate gradient and the data space Gauss-Newton schemes to perform deterministic inversions. The code is also freely available for academic purposes and is very likely to have a major impact on the plane-wave EM community in the coming years.

Monte Carlo methods applied to the inversion of plane-wave EM data are still rare. The first paper using Monte Carlo sampling for plane-wave EM methods was published by Tarits *et al.* (1994). The authors estimated the posterior pdf of the thicknesses and electrical conductivities of a fixed number of layers. Grandis *et al.* (1999) employed MCMC simulation sampling from a prior distribution that favors smooth conductivity variations in the one-dimensional model and with fixed layer thicknesses. The same authors presented a MCMC inversion to determine the laterally varying conductivity of an anomalous thin-sheet (Vasseur and Weidelt, 1977) embedded in a one-dimensional medium (Grandis *et al.*, 2002).

Hou *et al.* (2006) used a quasi-Monte Carlo method (Ueberhuber, 1997, p. 125) to find one-dimensional models of reservoir-fluid saturation and porosity by jointly inverting controlled source electromagnetic (CSEM) and seismic data. The same types of data were jointly inverted by Chen *et al.* (2007) using MCMC simulation to derive one-dimensional models of gas saturation. In a more recent contribution, Guo *et al.* (2011) compared deterministic and Bayesian one-dimensional inversions using synthetic and field MT data. Minsley (2011) presented a one-dimensional trans-dimensional MCMC inversion (Malinverno, 2000) algorithm for EM data, in which the number of layers was assumed unknown. Their approach favors model parsimony between models that equally fit the data (c.f. Malinverno, 2002). Ray and Key (2012) used the same type of method to determine one-dimensional anisotropic resistivity profiles from marine CSEM data. More recently, Buland and Kolbjørnsen (2012) jointly inverted synthetic CSEM and MT data in one-dimension. Khan *et al.* (2006) used EM data within a MCMC framework to constrain the composition and thermal state of the mantle beneath Europe.

After the work of Grandis *et al.* (2002) for thin-sheets, the first MCMC two-dimensional inversion of plane-wave EM data was presented by Chen *et al.* (2012). These authors fix the number of layers in the model but invert for the posterior pdf of the layers thicknesses and resistivities at given offsets and interpolated these values to obtain the two-dimensional conductivity distribution.

Monitoring with plane-wave EM methods

The last twenty years have seen tremendous advances in the use of geophysics to infer temporal changes in subsurface properties, especially for groundwater systems (e.g., Rubin and Hubbard, 2005), but surprisingly few published studies consider inductive electromagnetic techniques. A number of numerical studies have focused on the potential of using CSEM to monitor hydrocarbon reservoirs. Most of these studies (e.g. Lien and Mannseth, 2008; Orange *et al.*, 2009; Black *et al.*, 2009; Berre *et al.*, 2011; Kang *et al.*, 2012) considered CSEM monitoring for marine applications, while a few (e.g. Wirianto *et al.*, 2010; Schamper *et al.*, 2011; Zhdanov *et al.*, 2013) presented feasibility studies of land-based CSEM. They all conclude that monitoring is feasible, although not easy due to the diffusive character of EM signals and the low frequencies required to reach the reservoirs. For successful applications, this implies rather strong temporal contrasts and significant volumes experiencing temporally varying subsurface conditions. An innovative alternative has been recently considered for on land CSEM monitoring which uses boreholes to set up the sources at depth and thus perform borehole-to-surface measurements (e.g. Girard *et al.*, 2011; Bergmann *et al.*, 2012; Vilamajó *et al.*, 2013). These studies report an improvement in the method sensitivity when the sources are close to the target.

For groundwater applications, the targets of interest are typically located at shallower depths than for hydrocarbon reservoirs. In a rare case study, Falgàs *et al.* (2009) successfully used AMT to monitor saltwater intrusion dynamics in a coastal aquifer in Spain. As the repeated surveys were not taken at the same positions, a time-lapse strategy as presented in section 1.2.1 could not be used and they inverted for independent conductivity models at each time. Nix (2005) monitored the spreading of a conductive tracer using scalar RMT data. By performing independent inversions along the same profile location at different times, models were obtained that were in fair accordance with groundwater data.

For deeper environmental applications such as volcanic and geothermal studies, plane-wave EM methods represent prominent monitoring tools due to their large penetration depth and their sensitivity to fluid conductivity, temperature and fracture connectivity. Bedrosian *et al.* (2004) performed one of the first magnetotelluric studies aimed at monitoring a fluid injection in a geothermal system. They conducted separate two-dimensional inversions and compared the resulting models to infer the conductivity changes post injection but no changes could be detected due to the large noise present in the data. Aizawa *et al.* (2009) conducted a one-year monitoring study at a volcano in Japan using two MT stations. The data indicate large temporal changes, but the sparse information only allowed to invert for two-dimensional models that suggested that the conductivity changes occurred at the sea level.

Peacock *et al.* (2012, 2013) presented MT monitoring results of an injection experiment in an enhanced geothermal system in Paralana, Australia. In this experiment, 3100 m^3 of saline water, together with acids, were injected at 3.7 km depth to stimulate the opening of fractures and enable remote monitoring of the plume path. The authors observed consistent changes in apparent resistivity and phase at approximately 50 MT station, however, no attempt was made to invert these data.

Electrical Resistivity Tomography

The electrical resistivity tomography (ERT) or direct-current resistivity (DCR) method involves the stimulation of current flow into the subsurface by means of grounded electrodes and the measurement of resulting electrical potential differences. The physics of the problem is also described by Maxwell's equations, but in the the zero-frequency limit due to the continuous current injected. This leads to Poisson's equation:

$$\nabla.\left(\sigma\nabla U\right) = -I\delta(r), \tag{1.35}$$

where $\mathbf{E} = -\nabla U$, U is the electrical potential, I the injected current at a point r and δ the Dirac delta function. Many two- and three-dimensional forward and inversion codes exist for the ERT method including the one by Kalscheuer *et al.* (2010), which also comprises a joint-inversion strategy for ERT and RMT data. Although these two methods are sensitive

to electrical conductivity, they are considered complementary since ERT is generally more sensitive to resistors and RMT is more sensitive to conductors (e.g., Kalscheuer *et al.*, 2010).

1.4 Objectives and outline of the thesis

The previously summarized works indicate the strong potential of plane-wave EM methods to infer temporal changes in the subsurface. Furthermore, field studies have confirmed significant data sensitivity to these changes at different spatial scales. While most of the studies have focused on the interpretation of the raw data changes or the comparison of independently inverted models, much of the methods' potential improvements rely on the inversion strategies used to obtain the subsurface models. The aim of this thesis is to improve the inversion results obtained from plane-wave EM methods by applying advanced strategies to tackle the static and time-lapse inversion problems. Such strategies involve the application of state-of-the-art inversion methodologies and a tailored treatment of the time-lapse data. Within the many approaches that could improve the inversion results, I considered key elements the incorporation of as much prior information as possible in the inversion, and the uncertainty quantification of the model estimates, which should lead to a better interpretation of the available information.

In the first part of this thesis, which is described in Chapter 2, I present the development of a two-dimensional deterministic approach to perform time-lapse inversion with plane-wave EM methods. The strategy is based on the incorporation of prior information in the inversion algorithm regarding expected changes in the electrical conductivity. The use of non-l_2 norms to penalize the model structure is introduced to obtain sharp limits between regions of the model that experienced temporal changes and regions that did not. A time-lapse differencing strategy is presented to remove the systematic error contribution from the time-lapse inversion. The performance of different model norms are evaluated with numerical tests, showing that the perturbed l_1-norm leads to the best inversion results. This work evidences an improvement in the characterization of temporal changes with respect to the classical approach of performing separate inversions and comparing the models.

Despite the positive results presented in Chapter 2, much room for improvement was left considering that the deterministic framework used only allowed me to find one possible model among the many that could equally explain the data and satisfy the imposed constraints. This is why I then decided to adopt a Bayesian framework and test the possibility of quantifying model parameter uncertainty in plane-wave EM inversion. Thus, in Chapter 3 I present a two-dimensional pixel-based probabilistic MCMC inversion strategy for separate and joint inversions of plane-wave EM and ERT data. I compare the uncertainties of the model parameters when considering different types of prior information on the model structure, different likelihood functions to describe the data errors, and joint inversion of RMT and ERT data. In addition, I show that the regularization parameter and the standard deviation of the data

errors can be retrieved by the MCMC inversion.

After the separate works on time-lapse and MCMC inversions presented in Chapters 2 and 3, respectively, I decided to combine these strategies to quantify uncertainty in the estimation of subsurface temporal changes with plane-wave EM methods. In this case, I decided to tackle the more realistic problem of characterizing these changes in three-dimensions, since most of the monitoring applications do not allow for the two-dimensional simplification. As illustrated by tests on synthetic and real data in Chapter 3, even when implemented in computer clusters and with efficient forward solvers, MCMC inversion involves a significant computational burden. However, much of this burden is associated with the number of model parameters to estimate, that is, the smaller the number of parameters, the fastest the convergence of the MCMC inversions. Chapter 4 presents the development and results of a three-dimensional time-lapse probabilistic inversion strategy for plane-wave EM. The work is focused on the use of the MT method to infer mass transfer in an enhanced geothermal system following an injection experiment. To alleviate the computational burden of the three-dimension forward solvers, I propose a model reduction strategy where only the coefficients of a Legendre moment decomposition of the injected water plume and the position of this plume in the subsurface are estimated. For this purpose, a base resistivity model is needed which can be obtained prior to the time-lapse experiment. A synthetic test is presented which shows that the methodology works well when the base resistivity model is correctly characterized. The methodology is also applied to an injection experiment performed in a geothermal system in Australia, and compared to a three-dimensional time-lapse inversion performed within a deterministic framework. The probabilistic inversion retrieves better constrained water plumes due to the larger amount of prior information that was included in the algorithm. However the conductivity changes in the model needed to explain the measured data changes are much larger than physically possible. A discussion is presented about this issue, which may be related to the limited quality of the base resistivity model.

Finally, in Chapter 5 I provide general conclusions derived from the results of this thesis and an outlook on future improvements related to my work.

Chapter 2

Focused time-lapse inversion of radio and audio magnetotelluric data

Marina Rosas Carbajal, Niklas Linde, and Thomas Kalscheuer

published in *Journal of Applied Geophysics*[1]

[1]M. Rosas Carbajal, N. Linde, and T. Kalscheuer (2012). Focused time-lapse inversion of radio and audio magnetotelluric data. *Journal of Applied Geophysics*, **84**, 29–38.

2.1 Abstract

Geoelectrical techniques are widely used to monitor groundwater processes, while surprisingly few studies have considered audio (AMT) and radio (RMT) magnetotellurics for such purposes. In this numerical investigation, we analyze to what extent inversion results based on AMT and RMT monitoring data can be improved by (1) time-lapse difference inversion; (2) incorporation of statistical information about the expected model update (i.e., the model regularization is based on a geostatistical model); (3) using alternative model norms to quantify temporal changes (i.e., approximations of l_1 and Cauchy norms using iteratively reweighted least-squares), (4) constraining model updates to predefined ranges (i.e., using Lagrange Multipliers to only allow either increases or decreases of electrical resistivity with respect to background conditions). To do so, we consider a simple illustrative model and a more realistic test case related to seawater intrusion. The results are encouraging and show significant improvements when using time-lapse difference inversion with non-l_2 model norms. Artifacts that may arise when imposing compactness of regions with temporal changes can be suppressed through inequality constraints to yield models without oscillations outside the true region of temporal changes. Based on these results, we recommend approximate l_1-norm solutions as they can resolve both sharp and smooth interfaces within the same model.

2.2 Introduction

Reliable monitoring of fluid redistribution and mass transfer in the subsurface are key elements to maximize oil, gas, and geothermal production, to evaluate the performance of CO_2 sequestration, or to manage environmental risk, such as saltwater infiltration in coastal areas. Time-lapse inversions of geophysical data enable subsurface monitoring and have been explored widely for diverse applications using a range of geophysical techniques. Time-lapse inversions resolve temporal changes better than differencing models from separate inversions because of enhanced cancellation of errors that are constant over time and because the model regularizations can be defined with respect to temporal changes. For example, LaBrecque and Yang (2001) showed that time-lapse difference inversion of 3D electrical resistance tomography (ERT) data yield models with increased error cancellation, faster convergence and higher resolution with fewer artifacts compared to differencing of separately inverted models. Ajo-Franklin *et al.* (2007) inverted temporal differences in crosshole seismic traveltimes to better resolve subsurface variations related to CO_2 sequestration. Doetsch *et al.* (2010) jointly inverted time-lapse crosshole electrical resistance and ground penetrating radar traveltime data to obtain improved images of moisture content plumes.

The last twenty years have seen tremendous advances in the use of geophysics for inferring temporal changes in groundwater systems (e.g., Rubin and Hubbard, 2005), but surprisingly few published studies consider inductive electromagnetic techniques (e.g., Falgàs *et al.*, 2009;

Minsley *et al.*, 2011). This is even more puzzling given the very long tradition of inductive methods in groundwater resources evaluations (e.g., Fitterman and Stewart, 1986; Tezkan, 1999; d'Ozouville *et al.*, 2008). One possible reason relates to the success and flexibility of ERT for this type of applications (e.g., Kemna *et al.*, 2002). Nevertheless, inductive techniques, such as radio magnetotellurics (RMT), have some distinct advantages compared with ERT: they are more sensitive to conductors that often represent the monitoring target; they work well in regions of high contact resistance (e.g., Beylich *et al.*, 2003); they are better suited for investigating anisotropy (Linde and Pedersen, 2004b); and they might provide models with superior resolution (for conductive structures) compared with ERT (Kalscheuer *et al.*, 2010). The same properties hold for audio magnetotelluric (AMT) applications that work well at depth ranges that are typically out of reach for ERT.

One of the most widely used inversion strategies for geophysical inversion is minimum structure inversion, in which the model with the least structure is sought under the constraint that the model is consistent with the data and the estimated data errors (e.g., Constable *et al.*, 1987; deGroot Hedlin and Constable, 1990; Siripunvaraporn and Egbert, 2000). To quantify model structure, the l_2-norm is commonly used. This is because its minimization results in a linear system to be solved, but it has the disadvantage that the models obtained are unrealistically smooth for many types of applications (Ellis and Oldenburg, 1994). Iteratively reweighted least squares (IRLS) algorithms make it possible to use non l_2-norms, while still solving a linear system at each iteration step. With such strategies, it is possible to obtain models with overall uniform regions separated by sharper interfaces. Last and Kubik (1983) used an IRLS scheme to minimize the total cross-sectional area of anomalous bodies when inverting 2D gravity data. Portniaguine and Zhdanov (1999) inverted 3D magnetic and gravity data by minimizing the volume in which the gradient of the properties is nonzero. Farquharson and Oldenburg (1998) minimized an l_1-type measure of the horizontal and vertical derivatives in the 2D inversion of electrical resistance data. Farquharson (2007) minimized an approximate l_1-norm of a combination of horizontal and vertical model differences together with differences between diagonal cells to better image dipping structures when inverting gravity and magnetotelluric (MT) data. Pilkington (1997) used the Cauchy norm to obtain sparse 3D magnetic models. The IRLS scheme has been successfully applied for different types of geophysical data to obtain compact models, but has only rarely been used in time-lapse applications (Ajo-Franklin *et al.*, 2007).

The primary motivation of this paper is to evaluate, through numerical examples, to what extent inversion results based on AMT and RMT monitoring data can be enhanced by (1) time-lapse difference inversion; (2) incorporation of statistical information about the expected model updates; (3) using appropriate model norms to quantify temporal changes, (4) constraining model updates to predefined ranges. After presenting the theoretical background (section 2), we present the results of two numerical case studies (section 3). We then dis-

cuss the implications of these results for field-based applications (section 4) before making our conclusions (section 5).

2.3 Method

2.3.1 Basic magnetotelluric theory

Using distant source signals, the MT method measures the relations between frequency-dependent electric and magnetic field components that are sensitive to the resistivity structure of the Earth. Under the assumption of far field conditions, these fields are related through the impedance tensor **Z** Cantwell (1960):

$$\begin{bmatrix} E_x(\omega) \\ E_y(\omega) \end{bmatrix} = \begin{bmatrix} Z_{xx}(\omega) & Z_{xy}(\omega) \\ Z_{yx}(\omega) & Z_{yy}(\omega) \end{bmatrix} \begin{bmatrix} H_x(\omega) \\ H_y(\omega) \end{bmatrix}, \tag{2.1}$$

where $\mathbf{E}(\omega) = [E_x(\omega), E_y(\omega)]^{\mathrm{T}}$ is the horizontal electric field and $\mathbf{H}_h(\omega) = [H_x(\omega), H_y(\omega)]^{\mathrm{T}}$ the horizontal magnetic field at a given angular frequency ω, with T denoting transposition. The apparent resistivities $\rho_{ij}^{\mathrm{app}}(\omega)$ and impedance phases $\varphi_{ij}^{\mathrm{app}}(\omega)$ can be obtained from the impedance components, for example, for Z_{xy}:

$$\rho_{xy}^{\mathrm{app}}(\omega) = \frac{1}{\omega\mu_0}|Z_{xy}(\omega)|^2, \tag{2.2}$$

$$\varphi_{xy}^{\mathrm{app}}(\omega) = \arctan\left(\frac{\mathrm{Im}Z_{xy}(\omega)}{\mathrm{Re}Z_{xy}(\omega)}\right), \tag{2.3}$$

where $\mu_0 = 4\pi 10^{-7}\mathrm{Hm}^{-1}$ is the magnetic permeability of free space (analogous definitions hold for Z_{yx}). The geomagnetic transfer function (so-called tipper pointer) **T** relates the vertical and horizontal magnetic fields as

$$\begin{bmatrix} H_z(\omega) \end{bmatrix} = \begin{bmatrix} A(\omega) & B(\omega) \end{bmatrix} \begin{bmatrix} H_x(\omega) \\ H_y(\omega) \end{bmatrix} = T^{\mathrm{T}} \begin{bmatrix} H_x(\omega) \\ H_y(\omega) \end{bmatrix}. \tag{2.4}$$

When considering 2D structures, Maxwells equations can, for an appropriate rotation of the coordinate system, be decoupled into two independent modes: transverse-electric (TE) and transverse-magnetic (TM) (e.g., Zhang *et al.*, 1987). Current flows parallel to the strike direction in the TE mode and perpendicular to it in the TM mode. The RMT and AMT methods considered here differ from the MT technique in terms of the higher frequency range of the measurements and in terms of the origin of the sources used, but the governing equations generally remain the same. Classical MT modeling neglects the influence of displacement currents, but these must be included when considering high RMT frequencies acquired over very resistive formations (e.g., Linde and Pedersen, 2004a; Kalscheuer and Pedersen, 2007).

2.3.2 Discrete deterministic inversion

The inverse problem of deriving the multi-dimensional resistivity structure of the subsurface using impedance tensors and tipper pointers only, is both non-linear and underdetermined when considering finely discretized models. These challenges are most often addressed by using iterative methods based on successive linearization and by incorporating regularization constraints that strongly penalize model structure that deviates from a preconceived morphology. A number of inversion algorithms are available that are based on different numerical approaches (e.g. deGroot Hedlin and Constable (1990); Siripunvaraporn and Egbert (2000); Rodi and Mackie (2001)). Solutions based on smoothness-constrained least-squares formulations are often referred to as Occam inversion (Constable *et al.*, 1987) and aim at finding the smoothest model that can explain the observed data within the assumed data errors. Given N observed data $\mathbf{d}^{\text{obs}} = [d_1, d_2, ..., d_N]^{\text{T}}$ and M resistivity blocks $\mathbf{m} = [m_1, m_2, ..., m_M]^{\text{T}}$ of constant properties with typically $M > N$, the inverse problem can in the 2D case be solved by minimizing the functional

$$W_\lambda(\mathbf{m}) = \alpha_y \|\delta_y(\mathbf{m}-\mathbf{m}_{ref})\|_2^2 + \alpha_z \|\delta_z(\mathbf{m}-\mathbf{m}_{ref})\|_2^2 + \lambda^{-1}\left\{\|\mathbf{C}_d^{-0.5}\left(\mathbf{d}^{obs} - \mathbf{F}[\mathbf{m}]\right)\|_2^2 - \chi_*^2\right\}, \quad (2.5)$$

where y and z denote the horizontal and vertical directions of the 2D profile, respectively, $\alpha_i i = y, z$ is the desired weight of smoothing in each direction, $\delta_i i = y, z$ is the difference operator, $\mathbf{m}_{ref}$ is a reference model, $\mathbf{C}_d^{-0.5} = \text{diag}[\sigma_1^{-1}, ..., \sigma_N^{-1}]$ aims at weighting the data with respect to their quality, $\mathbf{F}[\mathbf{m}]$ is the forward response of $\mathbf{m}$, $\chi_d^2 = \|\mathbf{C}_d^{-0.5}\left(\mathbf{d}^{obs} - \mathbf{F}[\mathbf{m}]\right)\|_2^2$ is the data misfit, χ_*^2 is the desired data misfit and λ is a trade-off parameter defining the weight in given to minimizing the model roughness. The desired model is found by iteratively solving:

$$\mathbf{m}_{k+1}(\lambda) = \left[\left(\mathbf{C}_d^{-0.5}\mathbf{J}_k\right)^{\text{T}}\mathbf{C}_d^{-0.5}\mathbf{J}_k + \lambda\left(\alpha_y\delta_y^{\text{T}}\delta_y + \alpha_z\delta_z^{\text{T}}\delta_z\right)\right]^{-1}\left(\mathbf{C}_d^{-0.5}\mathbf{J}_k\right)^{\text{T}}\mathbf{C}_d^{-0.5}\hat{\mathbf{d}}_k + \mathbf{m}_{\text{ref}}, \quad (2.6)$$

where $\hat{\mathbf{d}}_k = \mathbf{d}^{\text{obs}} - \mathbf{F}[\mathbf{m}_k] + \mathbf{J}_k\Delta\mathbf{m}_k$, $\Delta\mathbf{m}_k = \mathbf{m}_k - \mathbf{m}_{ref}$, the subscripts k and $k+1$ denote the previous and present iterations, $\mathbf{J}$ is the sensitivity matrix or Jacobian matrix, and λ is determined through a line search. In the first iterations, λ is chosen to minimize χ_d^2 . When $\chi_d^2 \leq \chi_*^2$, λ is maximized under the constraint of satisfying $\chi_d^2 \leq \chi_*^2$. The inverse of the matrix in square brackets in Eq. (2.6) is referred to as the generalized inverse. The data misfit of inversion models is often represented in terms of the root mean square (RMS) misfit:

$$RMS = \sqrt{\frac{1}{N}\sum_{1\leq n\leq N} w_n^2}, \quad (2.7)$$

where $\mathbf{w} = \mathbf{C}_d^{-0.5}\left(\mathbf{d}^{obs} - \mathbf{F}[\mathbf{m}]\right)$. Given a Gaussian distribution of errors, the expected value of χ^2 is N, which corresponds to an RMS misfit of 1. Using the l_2-norm to quantify model

structure, as in Occam inversion, favors smooth transitions of model properties over a number of model cells (e.g., Farquharson, 2007). If sharp transitions between geological units or anomalies with small spatial supports are expected, it is necessary to work with other model norms to obtain models in agreement with such pre-supposed properties. One numerically efficient way to do this is through iteratively reweighted least squares (IRLS) algorithms (e.g., Farquharson and Oldenburg, 1998; Portniaguine and Zhdanov, 1999; Ajo-Franklin *et al.*, 2007; Pilkington, 1997). These algorithms rely on a least-square formulation similar to Eq. (2.6), but with the difference that reweighting matrices are defined after each iteration to approximate a given norm. This results in algorithms with similarly fast convergence characteristics as gradient-based formulations, but they allow resolving sharp interfaces or compact anomalies. The update to the IRLS solution of a non-linear inverse problem can be generalized as (e.g., Farquharson and Oldenburg, 1998; Menke, 1989; Siripunvaraporn and Egbert, 2000):

$$\mathbf{m}_{k+1}(\lambda) = \left[\left(\mathbf{C}_d^{-0.5}\mathbf{J}_k\right)^{\mathrm{T}}\mathbf{R}_{d,k}\mathbf{C}_d^{-0.5}\mathbf{J}_k + \lambda\left(\mathbf{C}_m^{-0.5}\right)^{\mathrm{T}}\mathbf{R}_{m,k}\mathbf{C}_m^{-0.5}\right]^{-1}\left(\mathbf{C}_d^{-0.5}\mathbf{J}_k\right)^{\mathrm{T}}\mathbf{R}_{d,k}\mathbf{C}_d^{-0.5}\hat{\mathbf{d}}_k + \mathbf{m}_{\mathrm{ref}}, \tag{2.8}$$

where $\mathbf{C}_m^{-0.5}$ indicates a more general and flexible model regularization matrix than the difference operator in Eq. (2.5), and $\mathbf{R}_i, i = m, d$ is a reweighting matrix that is recalculated after each iteration and that depends on the norm chosen. In this work, the amount of model structure is quantified by considering a given norm of the vector $\mathbf{x} = \mathbf{C}_m^{-0.5}\Delta\mathbf{m}$. There are several norms that can be used to emphasize different aspects of model structure. For example, Ekbloms perturbed l_p-norm

$$\phi(x) = \sum_{1\leq m\leq M}\left(x_m^2 + \gamma^2\right)^{p/2}, \tag{2.9}$$

where γ is a small number with respect to x_m. Choosing $p = 1$ makes it possible to approximate the l_1-norm with the advantage that its derivative exists at $x = 0$. The l_1-norm imposes penalizations proportional to the values of x, contrary to the l_2-norm, which provides an enhanced penalization of large values. Ekbloms norm can be implemented in the IRLS algorithm by taking $\mathbf{R}$ as:

$$R_{ii} = p\left(x_i^2 + \gamma^2\right)^{p/2-1}. \tag{2.10}$$

Last and Kubik (1983) and Portniaguine and Zhdanov (1999) use a minimum support measure defined as

$$\phi(x) = \sum_{1\leq m\leq M}\frac{x_m^2}{\left(x_m^2 + \gamma^2\right)}, \tag{2.11}$$

with a corresponding $\mathbf{R}$:

$$R_{ii} = \frac{2\gamma^2}{\left(x_i^2 + \gamma^2\right)^2}, \tag{2.12}$$

This norm is proportional to the number of non-zero elements of x. The Cauchy norm

$$\phi(x) = \sum_{1 \leq m \leq M} \ln\left(1 + \frac{x_m^2}{\gamma^2}\right), \tag{2.13}$$

with

$$R_{ii} = \frac{1}{\left(x_i^2 + \gamma^2\right)}, \tag{2.14}$$

is another norm used to obtain an x with few values different from zero (Sacchi and Ulrych, 1996; Pilkington, 1997). The norm decreases as more elements of x_m are smaller than γ. The choice of γ controls the amplitudes and the fractions of non-zero values. For the numerical experiments considered in this work, we have found that taking $\gamma = \sum_{1 \leq m \leq M} |\frac{x_m}{M}|$ leads to satisfactory solutions for all cases considered. Schemes based on IRLS must allow for several model iterations before the final model is computed, such that the reweighting of the regularization term is consistent with the final model. As shown in Eq. (2.8), the IRLS scheme can also be used to apply different norms to quantify data misfit. In these numerical investigations, we assume and impose a Gaussian distribution of the data residuals. The data misfit was consequently quantified with a classical l_2-norm (c.f., Eq. (2.7)), which is optimal for Gaussian errors.

2.3.3 Time-lapse inversion

When monitoring temporal changes in subsurface properties it is advantageous to leave the sensors in place during the monitoring period. The errors in the resulting time-lapse data acquired for the same sensor configuration are likely to share a repeatable systematic component, which can be largely removed in the time-lapse inversion. Following LaBrecque and Yang (2001), the observed data at time-lapse t can be expressed as:

$$\mathbf{d}_t^{obs} = \mathbf{F}[\mathbf{m}_t] + \boldsymbol{\varepsilon}_{\text{sys}} + \boldsymbol{\varepsilon}_{\text{r},t}, \tag{2.15}$$

where $\boldsymbol{\varepsilon}_{\text{r},t}$ is a random observational error that is varying in time and is thus different for each data set and $\boldsymbol{\varepsilon}_{\text{sys}}$ is a systematic contribution that is present at all times. Systematic errors can be related to modeling errors, bias introduced by ground coupling problems or improperly calibrated sensors, deviations from 2D assumptions or geometrical errors (e.g., incorrect electrode positioning or profiles that are not perfectly aligned). Time-lapse inversion algorithms can be defined in different ways but aim generally at removing the systematic contribution to allow resolving minute changes in subsurface properties over time. In a first step, the model at $t = 0$, $\mathbf{m}_0$, is obtained by means of a standard inversion (see section

2.2.) using the data acquired before any perturbation to the system. Next, the residuals $\mathbf{r}_0 = \mathbf{d}_0^{obs} - \mathbf{F}[\mathbf{m}_0] = \boldsymbol{\varepsilon}_{\text{sys}} + \boldsymbol{\varepsilon}_{\text{r},0}$, are removed from the data acquired at all subsequent times:

$$\tilde{\mathbf{d}}_t^{obs} = \mathbf{d}_t^{obs} - \mathbf{r}_0 = \mathbf{F}[\mathbf{m}_t] + \boldsymbol{\varepsilon}_{\text{r},t} - \boldsymbol{\varepsilon}_{\text{r},0}, \tag{2.16}$$

Since the systematic component has been removed by differencing, the new corrected data sets have the advantage of being less error contaminated, provided the common situation concerning the standard deviations of the different error sources that $\sigma_{sys} > \sqrt{\sigma_{r,0}^2 + \sigma_{r,t}^2}$ (e.g., Doetsch *et al.*, 2010). Furthermore, $\mathbf{m}_0$ can be used as the reference model $\mathbf{m}_{ref}$ for the following inversions, so that the model regularization is applied to the model update with respect to the model reference.

2.3.4 Stochastic regularization

Statistical information of the expected model update with respect to $\mathbf{m}_{ref}$ can be used to constrain time-lapse inversions and thereby accurately include statistical properties as a priori information. Maurer *et al.* (1998) showed that regularization based on model covariance models, so-called stochastic regularizations, uniquely define the relative contribution of penalizing roughness (i.e., to obtain smooth models) with respect to damping (i.e., to obtain models that are close to $\mathbf{m}_{ref}$). A given covariance function is used to compute the model covariance matrix, which is then inverted to obtain the regularization matrix $\mathbf{C}_m^{-0.5}$. When the correlation function is stationary throughout a uniform grid, the covariance matrix can be inverted efficiently through circulant embedding and using the diagonalization theorem of circulant matrices (Dietrich and Newsam, 1997; Linde *et al.*, 2006). Here we consider the exponential correlation function for a two-dimensional domain that is defined as

$$r(l) = c\exp(-l), \tag{2.17}$$

where c is the variance and l is

$$l = \sqrt{\left(\frac{h_y}{I_y}\right)^2 + \left(\frac{h_z}{I_z}\right)^2}, \tag{2.18}$$

where $h_i, i = y, z$ is the separation between two points and $I_i, i = y, z$ is the integral scale that characterizes the spatial correlation in each direction (e.g., Rubin, 2003). When the distance between two points equals the integer scale, their correlation is $1/e \simeq 37\%$. As the same constant c is assumed for all model parameters, the multiplication of $\mathbf{C}_m^{-0.5}$ in Eq. (2.8) results in the inverse of the constant c being multiplied with λ. As we perform a line search for λ, we set $c = 1$.

2.3.5 Guiding the model update

Constraints regarding model parameter updates can be incorporated through Lagrange multipliers (e.g., Menke, 1989, Chapter 3.10). If the model values are only expected to decrease with respect to $\mathbf{m}_{\text{ref}}$ (e.g., electrical resistivity is expected to decrease due to the application of a saline tracer), one can guide the inversion by penalizing model parameters exhibiting positive deviations from$\mathbf{m}_{\text{ref}}$ in iteration k, to have values closer to $\mathbf{m}_{\text{ref}}$ in iteration $k+1$ by adding the constraint $\mathbf{H}_k \Delta\mathbf{m}_{k+1} = \mathbf{0}$, where $\mathbf{H}_k$ is of size $M_v \times M$, and M_v is the number of elements of $\Delta\mathbf{m}_k$ that are positive and should be guided to be zero. In iteration $k+1$, $\mathbf{H}_k$ is generated from $\Delta\mathbf{m}_k$ as

$$H_k^{ij} = \begin{cases} 1, & \text{if } \Delta m_k^j > 0 \text{ is the } i\text{-th value to penalize,} \\ 0, & \text{otherwise.} \end{cases} \tag{2.19}$$

The constraint equation must be solved simultaneously with Eq. (2.8) (Menke, 1989), which results in an augmented system of equations:

$$\begin{bmatrix} \mathbf{m}_{k+1}(\lambda) \\ \mathbf{v}(\lambda) \end{bmatrix} = \begin{bmatrix} \left(\mathbf{C}_d^{-0.5}\mathbf{J}_k\right)^{\mathrm{T}} \mathbf{R}_{d,k} \mathbf{C}_d^{-0.5}\mathbf{J}_k + \lambda \left(\mathbf{C}_m^{-0.5}\right)^{\mathrm{T}} \mathbf{R}_{m,k} \mathbf{C}_m^{-0.5} & \mathbf{H}_k^{\mathrm{T}} \\ \mathbf{H}_k & \mathbf{0} \end{bmatrix}^{-1} \times \begin{bmatrix} \left(\mathbf{C}_d^{-0.5}\mathbf{J}_k\right)^{\mathrm{T}} \mathbf{R}_{d,k} \mathbf{C}_d^{-0.5} \hat{\mathbf{d}}_k \\ \mathbf{0} \end{bmatrix} + \begin{bmatrix} \mathbf{m_{ref}} \\ \mathbf{0} \end{bmatrix}, \tag{2.20}$$

where $\hat{\tilde{\mathbf{d}}}_k = \tilde{\mathbf{d}}_t^{\text{obs}} - \mathbf{F}[\mathbf{m}_k] + \mathbf{J}_k \Delta\mathbf{m}_k$, and we solve for the M new model parameters in vector $\mathbf{m}_{k+1}$, plus the M_v unknown Lagrange multipliers in vector $\mathbf{v}$.

2.4 Numerical examples

2.4.1 A shallow prism

A very simple synthetic test case was considered to investigate the influence of the different regularizations and norms presented in section 2 on the time-lapse inversions results. The test case consists of a model that changes between time instance $t = 0$ (Fig. 2.1a) and $t = 1$ (Fig. 2.1b), in which the only difference is a conductive prism with a cross-sectional area of 66 m^2 that appears at $t = 1$.

The forward responses of the models were computed for both the TE and TM modes including the real and imaginary parts of the tipper pointer, at 7 stations with a separation of 5 m. A total of 10 frequencies regularly spaced in logarithmic scale (two frequencies per octave) were used in the RMT frequency range of 10 to 226 kHz, which resulted in 420 data points. A mesh of 58104 cells was used for the forward computations and the inversions, including 10 rows needed to model the air. The central part of the mesh, which is shown in Fig.2.1 and

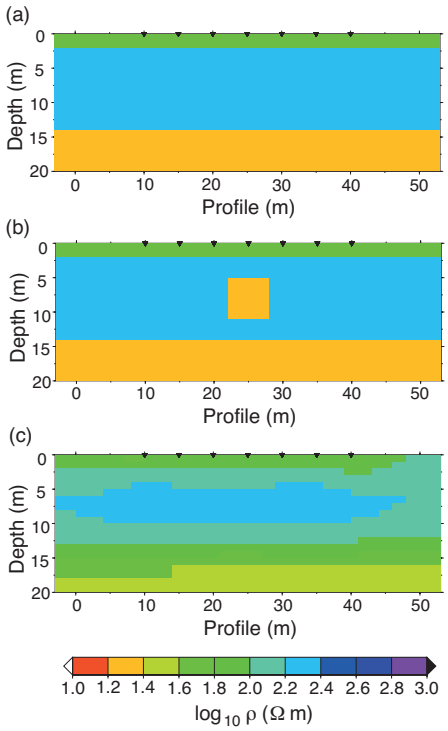

Figure 2.1: Synthetic 2D models used to generate the data at (a) $t = 0$ and (b) $t = 1$ for the shallow prism model. (c) Reference model for the time-lapse inversions obtained by inverting the data at $t = 0$ with an Occam algorithm. The triangles at the top of the figures indicate station locations.

2.2, has a 11 m^2 discretization. All the forward calculations and inversions presented here were calculated using a modified version (cf. Kalscheuer *et al.*, 2010) of the REBOCC code (Siripunvaraporn and Egbert, 2000).

To simulate the time-lapse data, two types of errors were added to the forward responses of the synthetic models (see section 2.3.). Uncorrelated Gaussian noise with zero mean was considered in all cases. For the impedances, standards deviations of $\sigma_{sys} = 10\%$ and $\sigma_{r,0} = \sigma_{r,1} = 2\%$ were considered, whereas for the real and imaginary part of the tipper $\sigma_{sys} = 0.02$ and $\sigma_{r,0} = \sigma_{r,1} = 0.005$ were used. Inversions of the synthetic data were performed using the different inversion and regularization schemes defined in sections 2.2-2.3. To allow for more iterations before convergence of the IRLS inversions, a maximum of five points were evaluated to determine λ and thereby decrease the convergence rate.

A standard smoothness-constrained least squares inversion, referred to as Occam in the following (see Eq. (2.6)), was used to obtain independently inverted models at each time. The errors assumed were 10.2% (i.e., $\sqrt{10^2 + 2^2}$) for the impedance elements and 0.0206 (i.e., $\sqrt{0.02^2 + 0.005^2}$) for the tipper components, and a half-space of 100 Ωm was used as the starting model. For the time-lapse inversions, new time-lapse corrected data sets were created

using Eq. (2.16)). The reference model used was the one obtained with an Occam inversion for $t = 0$ (Fig. 1c). The errors assumed were corresponding to the random components of the noise added.

Figure 2.2 2 shows the true model update (Fig. 2.2a) together with the model updates obtained with the different inversion schemes (Fig. 2.2b-h). All the models in Fig. 2.2 fit the data with RMS ≤ 1.05. Figure 2.2b shows the model update obtained by differencing the two separate Occam inversions. The region of change is approximately detected, but it is resolved as a smoothly varying feature of strongly overestimated extent that is centered below the actual anomaly. Furthermore, positive updates representing artifacts appear on the sides of the model. Figure 2.2c shows the result of applying the time-lapse inversion to the traditional Occam inversion (i.e., time-lapse corrected data, but with smoothness constraints using an l_2 measure). The lower error-level in the time-lapse corrected data helps to better constrain the geometry of the model update, which is considerably more focused than the previous example. However, the model update is still rather smooth due to the l_2 measure of model structure and oscillations representing inversion artifacts are still visible. Figure 2.2d shows the model update obtained using stochastic regularization with the l_2-norm in the time-lapse scheme. Assuming that points more than 6 m apart are poorly correlated, the integral scales were chosen as $I_y = I_z = 3$m (correlation is less than 14% for separations larger than two integral scales, see Sec. 2.4). The model obtained is very similar to that of Fig. 2.2c. Figure 2.2e-g show the results of applying the stochastic regularization to the time-lapse inversion using the perturbed l_1-norm, minimum support norm and Cauchy norm as measures of model structure, respectively. The delineations of the anomalous region are much sharper and the oscillations shown in Fig. 2.2b-d have essentially been removed. Some cells with positive resistivity changes can be seen in the three models, close to the receiver stations in Fig. 2.2e and g and inside the prism in Fig. 2.2f. These features disappear when penalizing positive changes to the model through Lagrange multipliers (see Eq. 2.20). The model update obtained with the penalized inversion using the l_1-norm is shown in Fig. 2.2h. Similar results were found with the Cauchy and minimum support measures. A feature that is common to all the cases where non l_2-norms were used is an overestimation of the inferred magnitude of the model update in the center of the prism.

Figure 2.3 shows horizontal slices at a depth of 8 m through the models in Fig. 2.2. The sharp changes and large amplitudes obtained with the non l_2-norms contrast strongly with the smoothly oscillating updates obtained with the l_2-norm inversions. The rather small amplitude observed in the curve representing the Cauchy norm model (Fig. 2.2g) is due to the maximum value not being found at 8 m, but at a depth of 7 m.

We define two measures to quantify the similarity between the proposed model updates and the true model update. The first one is an average of the final Δm for the cells located in the

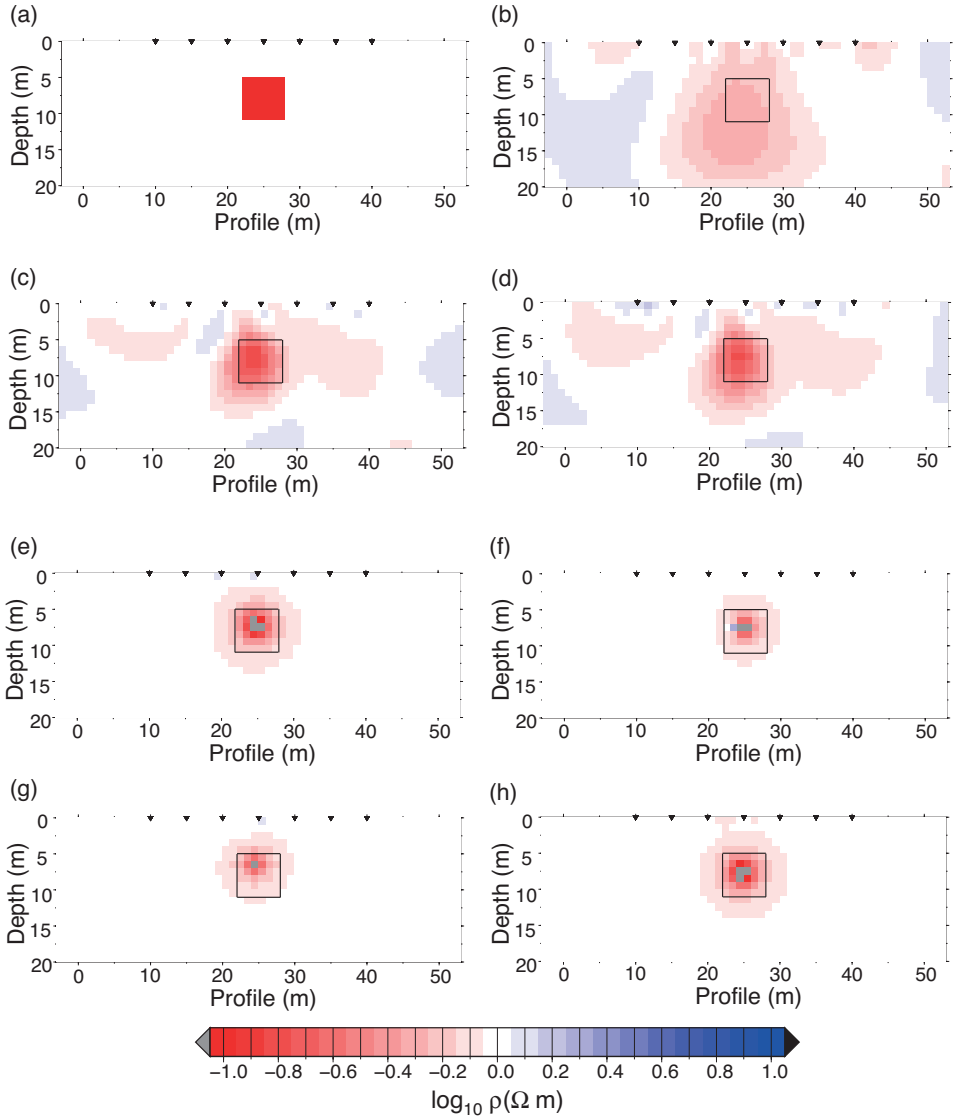

Figure 2.2: Model differences at $t = 1$ for the shallow prism example. (a) True difference between the synthetic models at $t = 1$ and $t = 0$. Model differences obtained using (b) differencing of Occam inversion models at $t = 1$ and $t = 0$, (c) time-lapse Occam inversion, time-lapse inversion with stochastic regularization using the (d) l_2-norm, (e) perturbed l_1-norm, (f) minimum support, (g) Cauchy norm, and (h) perturbed l_1-norm with negativity constraints applied to the model update. Grey color-coding indicates overestimated differences with respect to the true differences.

region where the true prism is located. Since inversions of electromagnetic data are essentially always working with logarithms of resistivity (or conductivity), the same units were used to compute the average. The second measure is an average of the amplitudes of $\Delta \boldsymbol{m}$ outside the region of the prism, which is zero for the true difference. It quantifies how much structure a certain solution is adding outside the region where the true changes occur.

The values of the two measures together with the RMS for the different inversion cases are

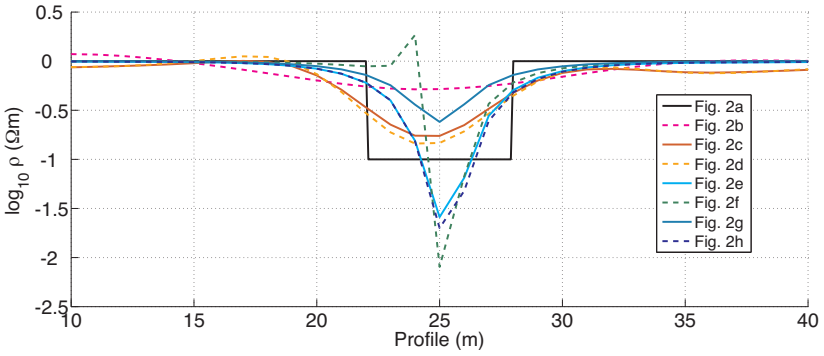

Figure 2.3: Horizontal slices through the model differences in Fig. 2.2 at a depth of 8 m.

Table 2.1: Statistics of performance measures for the model differences shown in Fig. 2.2.

Inversion strategy	Mean of Δm inside the true anomaly $\log_{10} \rho(\Omega\text{m})$	Mean of $\lvert\Delta m\rvert$ inside the true anomaly $\log_{10} \rho(\Omega\text{m})$	RMS
True model difference	-1	0	0.97
Difference of Occam inversions	-0.27	0.078	0.97
TL Occam inversions	-0.54	0.058	1.00
TL stoch. reg. l_2-norm	-0.58	0.053	0.98
TL stoch. reg. perturbed l_1-norm	-0.5	0.015	0.99
TL stoch. reg. minimum support	-0.3	0.006	1.02
TL stoch. reg. Cauchy norm	-0.3	0.007	1
TL stoch. reg. Cauchy norm + negativity contraints	-0.53	0.014	1.04

given in Table 2.1. For the true model difference, the means inside and outside the anomaly are -1 and 0, respectively. The traditional Occam scheme has a mean of -0.27 inside the anomaly and 0.078 in the outside region. For the time-lapse cases, the l_2-norm gives better estimates of the average magnitude of the update, with means of -0.54 and -0.58, but puts a lot of structure outside the region of changes (means of 0.058 and 0.053). On the other hand, the non l_2-norms have a smaller average update, but the structure outside the true anomaly has decreased with 1 or 2 orders of magnitude. When the update calculated using the Cauchy norm is constrained to be negative, the average value within the prism is closer to the actual value (-0.53).

2.4.2 Seawater intrusion example

The second more complex test case is inspired by the experiment of Falgàs *et al.* (2009), who monitored a seawater-freshwater mixing zone over time using AMT. The models at $t = 0$ and $t = 1$ are shown in Figs. 2.4a and b. The models comprise a 100 m thick 100 Ωm layer, in which seawater intrusion occurs in the lower 50 m. The aquifer overlies a 630 Ωm half-space. The sea is modeled in the rightmost upper corner with a resistivity of 0.3 Ωm. The seawater encroachment is represented with a linearly increasing resistivity, from 3 Ωm corresponding to a rock completely saturated with seawater to 100 Ωm corresponding to freshwater conditions. At $t = 1$, the seawater-freshwater interface has advanced 300 m inland with respect to the situation at $t = 0$.

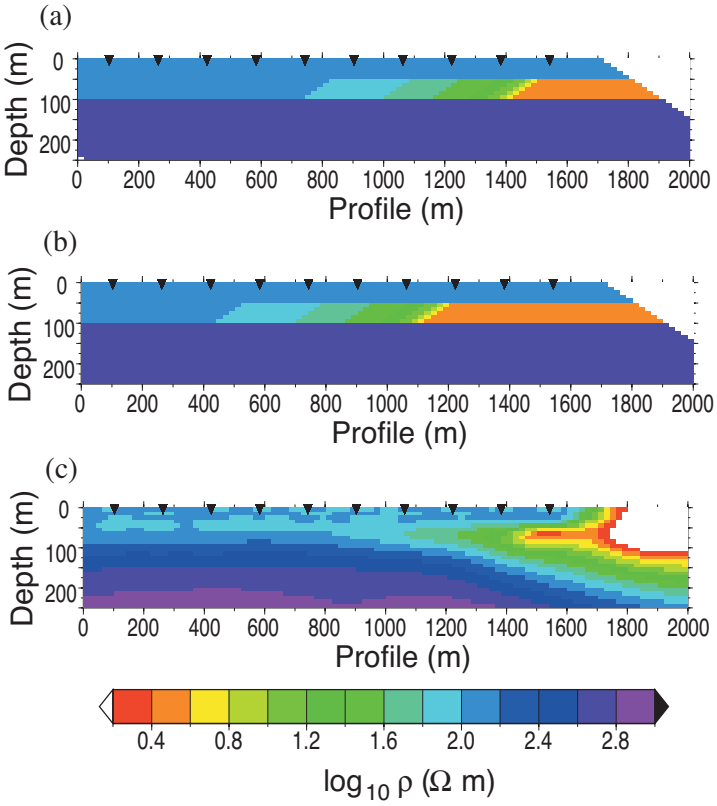

Figure 2.4: Synthetic 2D models used to generate the data at (a) $t = 0$ and (b) $t = 1$ for the seawater intrusion example. (c) Reference model for the time-lapse inversions obtained by inverting the data at $t = 0$ with an Occam algorithm. The triangles at the top of the figures indicate station locations.

The forward responses were simulated considering 10 stations with a spacing of 160 m and a frequency range of 10 Hz to 116 kHz (two frequencies per octave as in the prism example). Within the region of interest, the cell size is 2010 m^2. The simulated TE mode, TM mode and tipper data were noise contaminated with $\sigma_{sys} = 5\%$ and $\sigma_{r,0} = \sigma_{r,1} = 2\%$ for the impedances, and $\sigma_{sys} = 0.02$ and $\sigma_{r,0} = \sigma_{r,1} = 0.005$ for the tipper components.

Figure 2.4 c shows the result of Occam inversion using the noise-contaminated data. A half-space of 100 Ωm was used as the starting model and a five times larger regularization weight was applied in the horizontal direction to emphasize the layered nature of the model. The model obtained is similar to the one shown by Falgàs *et al.* (2009). The seawater encroachment is clearly detected and the upper part of the aquifer is well resolved, but the lower part is imaged with a gradual increase in the resistivity rather than a sharp transition.

Figure 2.5a shows the difference between the true models at times $t = 1$ and $t = 0$. Changes in the horizontal direction are smooth, while the transition between layers in the vertical direction is sharp. The model difference between the two independent Occam inversions is shown in Fig. 2.5b. The upper interface of the time-lapse anomaly is well resolved, whereas the lower interface is very diffuse and extends to large depths. The lateral extension of the anomalous region is well resolved, but a positive artifact is shown to the right. The model update given by the time-lapse inversion with stochastic regularization ($I_y = 200$ m and $I_z = 20$ m) using the l_2-norm (Fig. 2.5c) and the Occam inversion as reference model better defines the lower interface, but presents more regions of positive inversion artifacts. When the perturbed l_1-norm is used (Fig. 2.5d), the positive changes observed in the lo wer part of the profile disappear and the transitions get sharper, but the positive changes towards the seaside prevail. Figure2.5e and f show the model updates obtained when penalizing positive values using the perturbed l_1-norm and Cauchy norm, respectively. The time-lapse target is well resolved and no oscillations are observed outside the region of the time-lapse target. Furthermore, in the case of the perturbed l_1-norm, the smooth horizontal transition is respected and the lateral extent of the anomaly corresponds overall quite well with the time-lapse target. This is not the case for the Cauchy norm, which resolves the time-lapse change as being laterally more compact than it really is. Furthermore, some cells with positive resistivity updates can still be observed for this model. Inversions using the minimum support norm with and without penalizing positive changes did not converge for this model.

Horizontal and vertical cuts of the models shown in Fig. 2.5 are presented in Fig. 2.6a and b, respectively. The true difference (shown in black in Fig. 2.6a) is smoothly varying in the horizontal direction. All the inversion schemes reproduce this transition rather well, except for the constrained Cauchy norm, shown in blue, which presents very small updates at this depth of 80 m. The largest differences between the models can be seen in the right part of the figure, that is, the region closer to the sea. Artifacts are present when using both the l_2-norm and the non-constrained l_1-norm. These artifacts disappear only when penalizing the positive updates, which results in a curve that closely follows the true model update at all points in the case of the perturbed l_1-norm. In the vertical cut (Fig. 2.6b), the results are similar to those of the prism example: the time-lapse inversions better constrain the model update, the non l_2-norms make the transitions sharper and the negativity constraints reduce or completely

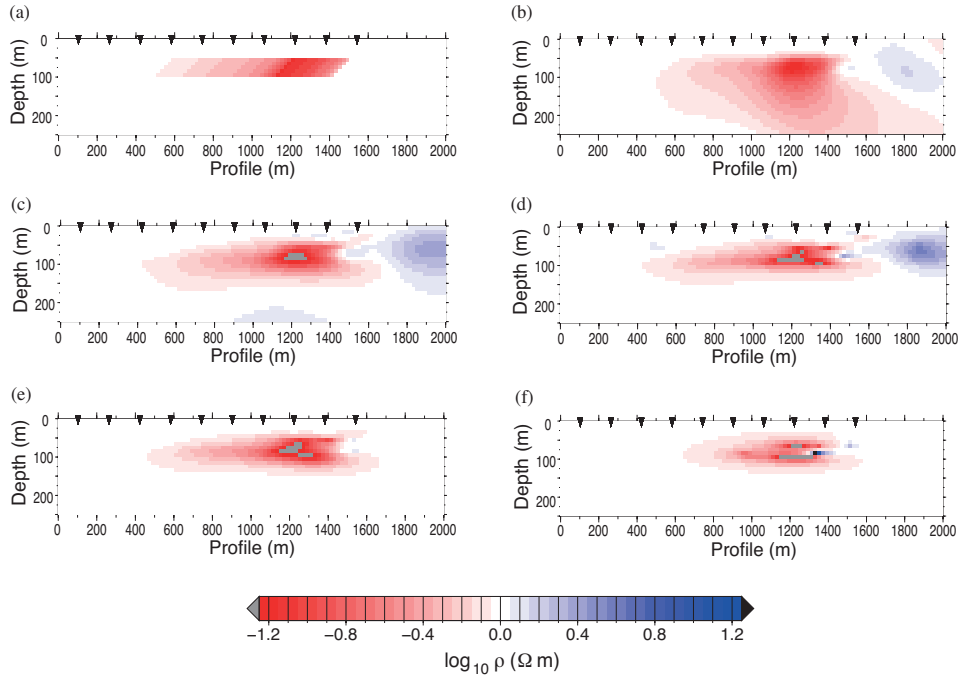

Figure 2.5: Model differences at $t = 1$ for the seawater intrusion example. (a) True difference between the synthetic models at $t = 1$ and $t = 0$. Model differences obtained using (b) differencing of Occam inversion models at $t = 1$ and $t = 0$, time-lapse inversion with stochastic regularization using the (c) l_2-norm, (d) perturbed l_1-norm, (e) perturbed l_1-norm with negativity constraints, and (f) Cauchy norm with negativity constraints. Grey color-coding indicates overestimated amplitudes with respect to the true differences.

eliminate positive value updates.

Table 2.2 shows the comparison statistics for each model in Fig. 2.5. The average value of the model update is -0.65 inside the true anomaly and 0 outside. Inside the anomaly, the mean magnitude is well estimated in all cases except for the Cauchy norm, which presents some positive updates inside the region of true change. Outside the anomaly, Occam inversion is again the method that puts the most structure (0.103) (c.f. table 2.1). The time-lapse inversion using the l_2-norm has a mean of absolute values of 0.098, and the perturbed l_1-norm 0.072. Only when the negativity constraints are added, the mean of the absolute values outside the anomalous region is reduced by one order of magnitude.

2.5 Discussion

Falgàs *et al.* (2009) demonstrated convincingly that AMT monitoring allows resolving seasonal seawater-freshwater dynamics. The aim of this work was to investigate through numerical examples to what extent these types of results could be further improved by using more refined inverse formulations.

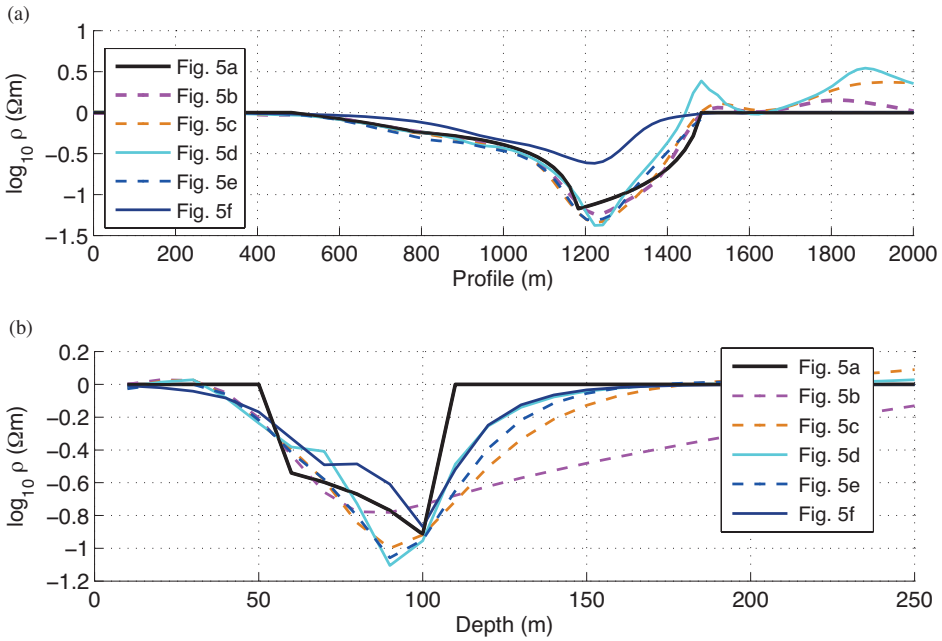

Figure 2.6: (a) Horizontal and (b) vertical slices of the model differences in Fig.2.5 at a depth of 80 m and a profile distance of 1200 m, respectively.

Table 2.2: Statistics of performance measures for the model differences shown in Fig.2.5.

Inversion strategy	Mean of Δm inside the true anomaly $\log_{10}\rho(\Omega\text{m})$	Mean of $\lvert\Delta m\rvert$ inside the true anomaly $\log_{10}\rho(\Omega\text{m})$	RMS
True model difference	-0.65	0	0.96
Difference of Occam inversions	-0.62	0.103	1.01
TL stoch. reg. l_2-norm	-0.67	0.098	1.04
TL stoch. reg. perturbed l_1-norm	-0.67	0.072	1.00
TL stoch. reg. perturbed l_1-norm + negativity constraints	-0.68	0.033	1.05
TL stoch. reg. Cauchy norm + negativity contraints	-0.44	0.021	1.04

As expected, removing errors that are constant over time (ε_{sys}) clearly yield improved models for the two case studies. The model updates provided by differencing independent Occam inversions (Fig. 2.2b and Fig. 2.5b) were unnecessarily diffuse compared with a difference inversion that otherwise is based on the same type of objective function (i.e., smoothness con-

straints and a l_2-norm). This improvement is explained by error cancellation in the difference inversion scheme as outlined by LaBrecque and Yang (2001).

Compared with smoothness constraints, stochastic regularization offers added flexibility in imposing statistical information of the expected model morphology (e.g., Linde *et al.*, 2006). In our case, this was used to add information about the expected scale of temporal changes in the model (Doetsch *et al.*, 2010). No specific integer scale can be defined for the model shown in Fig. 2.1b because of the superposition of geological layers and the time-lapse anomaly, while this is easier when inverting for the model update (Fig. 2.2a). For the examples considered in this study, we do not find any significant differences between the time-lapse inversion results based on an l_2-norm when using stochastic regularization (Fig. 2.1d) compared with smoothness constraints (Fig. 2.1c). In fact, both types of models are unsuitable as they are overly smooth and display oscillations in the region around the true anomaly.

To obtain sharper transitions, we applied non l_2-norms in a similar manner as Farquharson and Oldenburg (1998), Portniaguine and Zhdanov (1999), and Pilkington (1997), but to time-lapse data (Ajo-Franklin *et al.*, 2007). Using the perturbed l_1-norm, the Cauchy norm and the minimum support measures, we obtained compact model updates with a significant decrease in structure outside the true anomaly (Fig. 2.2e-g and Fig. 2.5d), but with the magnitude in some of the model cells being overestimated (Fig. 2.3 and Fig. 2.5).

The seawater on the right side in the saltwater intrusion example resulted in significant artifacts in the time-lapse inversions, especially for the non l_2-norms. Even if the values in this region at $t = 1$ were the same as at $t = 0$, large positive structures appeared for the three non-traditional norms used (only the perturbed l_1-norm example is shown in Fig. 2.5d). As we were considering a time at which the seawater-freshwater transition zone advances inland, it was natural to penalize positive changes in resistivity. Each cell with constraints adds a dimension to the matrix that has to be inverted, which can be computationally demanding in terms of memory and computing time. For the examples considered here, the number of elements of the model update that need to be penalized constitutes a significant percentage of the model blocks only in the first iterations. Note that penalizing positive values by adding Lagrange multipliers does not ensure that no positive cells are going to be found in the model update. Indeed, a few positive cells can be observed in the model update calculated with the Cauchy norm when applying the negativity constraints.

Another technical issue is that the reweighting needed for the non-traditional norm increases the condition number of the generalized inverse and also tends to increase the non-linearity of the inverse problem. Of the three norms considered, the perturbed l_1-norm was found to be the most robust in the sense that it did not significantly change the condition number of the matrices to be inverted compared with the l_2-norm case.

2.6 Conclusions

We find that inversion results based on monitoring of uniform inducing field electromagnetic data (RMT and AMT in the examples considered) can be much improved by using difference inversion and by incorporating information regarding the expected changes in model properties over time. Compact and sharper model updates were obtained by combining stochastic regularization and non l_2-norms implemented through an IRLS procedure. In particular, the perturbed l_1-norm was found to be both robust and allowing for smooth variations, not creating compact models when this was not the case. Penalizing model updates with non-physical variations (e.g., increases in resistivity when saltwater is intruding) was shown to be successful not only in avoiding inversion artifacts, but also, in the case of the perturbed l_1-norm, to better determine the magnitudes of the time-lapse changes. A characteristic of all model updates computed with non l_2-norms is the overestimation of the magnitudes of the changes in some cells. Such overestimations can be removed using Lagrange multipliers, similarly as for the negativity constraints, given that the expected maximum amplitudes of the true changes are known or can be adequately assessed. The presented inversion methodology will in the future be applied to field data, which will require the development of robust transfer function estimation procedures of time-lapse data.

2.7 Acknowledgments

This research was supported by the Swiss National Science Foundation under grant 200021-130200. We thank Juanjo Ledo and an anonymous reviewer for their useful comments. The original EM inversion code EMILIA, and the presented implementations, are available upon request by contacting Thomas Kalscheuer: thomas@aug.ig.erdw.ethz.ch.

Chapter 3

Two-dimensional probabilistic inversion of plane-wave electromagnetic data: Methodology, model constraints and joint inversion with electrical resistivity data

Marina Rosas-Carbajal, Niklas Linde, Thomas Kalscheuer and Jasper Vrugt

published in *Geophysical Journal International*[1]

[1]M. Rosas-Carbajal, N. Linde, T. Kalscheuer and J. Vrugt (2013). Two-dimensional probabilistic inversion of plane-wave electromagnetic data: Methodology, model constraints and joint inversion with electrical resistivity data. *Geophysical Journal International*, 196 (3), 1508-1524.

3.1 Abstract

Probabilistic inversion methods based on Markov chain Monte Carlo (MCMC) simulation are well suited to quantify parameter and model uncertainty of nonlinear inverse problems. Yet, application of such methods to CPU-intensive forward models can be a daunting task, particularly if the parameter space is high dimensional. Here, we present a 2-D pixel-based MCMC inversion of plane-wave electromagnetic (EM) data. Using synthetic data, we investigate how model parameter uncertainty depends on model structure constraints using different norms of the likelihood function and the model constraints, and study the added benefits of joint inversion of EM and electrical resistivity tomography (ERT) data. Our results demonstrate that model structure constraints are necessary to stabilize the MCMC inversion results of a highly discretized model. These constraints decrease model parameter uncertainty and facilitate model interpretation. A drawback is that these constraints may lead to posterior distributions that do not fully include the true underlying model, because some of its features exhibit a low sensitivity to the EM data, and hence are difficult to resolve. This problem can be partly mitigated if the plane-wave EM data is augmented with ERT observations. The hierarchical Bayesian inverse formulation introduced and used herein is able to successfully recover the probabilistic properties of the measurement data errors and a model regularization weight. Application of the proposed inversion methodology to field data from an aquifer demonstrates that the posterior mean model realization is very similar to that derived from a deterministic inversion with similar model constraints.

3.2 Introduction

Geophysical measurement methods make it possible to non-invasively sense the physical properties of the subsurface at different spatial and temporal resolutions. Inversion methods are required to interpret these indirect observations and derive a physical description of the subsurface, yet multiple descriptions can be found (also referred to as models) that fit the observed geophysical data equally well. This is in large part due to measurement errors, incomplete data coverage, the underlying physics and/or overparameterization of the subsurface models. Whereas the probabilistic properties of observation errors are relatively easy to describe, model structural errors are difficult to formulate in probabilistic terms. Arbitrary and subjective regularizations and parameterizations may significantly decrease model parameter uncertainty but they may also introduce a bias, meaning that some features of the true model may not be resolved.

Bayesian inference can help to explicitly treat input data, parameter, and model uncertainty, but successful implementation requires efficient sampling methods that explore the posterior target distribution. In this probabilistic approach, the inverse problem is stated as an inference problem where the solution is given by the posterior probability density function (pdf) of

the model parameters. This distribution quantifies joint and marginal parameter uncertainty. Unfortunately, in most practical applications, this posterior distribution cannot be derived analytically, and methods are required that use trial-and-error sampling to approximate the target distribution. Markov chain Monte Carlo (MCMC) simulation methods are well suited for this task, but suffer from poor efficiency, particularly when confronted with significant model nonlinearity, nonuniqueness and high-dimensional parameter spaces (Mosegaard and Tarantola, 1995).

The basic building block of MCMC sampling is Monte Carlo (MC) simulation. This approach randomly samples the prior parameter space, and evaluates the distance of the response of each candidate model to the respective data. If the parameter space is low dimensional, MC simulation can provide a reasonable approximation of the posterior distribution pending that the ensemble of samples is sufficiently large. Yet, for higher dimensional spaces, exhaustive random sampling is inefficient, and more intelligent search methods such as MCMC simulation are required to speed up the exploration of the target distribution. Monte Carlo methods have been applied to magnetotelluric (MT) data and other types of frequency-domain electromagnetic (FDEM) data in a number of studies for 1-D modeling problems (Tarits *et al.*, 1994; Grandis *et al.*, 1999, 2002; Hou *et al.*, 2006; Khan *et al.*, 2006; Chen *et al.*, 2007; Guo *et al.*, 2011; Minsley, 2011; Buland and Kolbjørnsen, 2012). We briefly summarize a few of these studies.

Tarits *et al.* (1994) used Monte Carlo sampling to estimate the posterior distribution of the thicknesses and electrical resistivity of different subsurface layers assuming that the number of layers is known a priori. Grandis *et al.* (1999) extended this 1-D approach by employing MCMC simulation with sampling from a prior distribution that favours smooth variations in the 1-D electrical resistivity model. Hou *et al.* (2006) used a quasi-Monte Carlo method (Ueberhuber, 1997, p. 125) for 1-D models of reservoir-fluid saturation and porosity to jointly invert controlled source electromagnetic (CSEM) and seismic data. The same types of data were jointly inverted by Chen *et al.* (2007) using MCMC simulation to derive 1-D models of gas saturation.

In a more recent contribution, Guo *et al.* (2011) compared deterministic and Bayesian MT data inversion using 1-D synthetic and field data. Data errors and regularization weight were treated as hyperparameters and determined by MCMC simulation (cf. Malinverno and Briggs, 2004). Results showed that the MT data contained sufficient information to accurately determine these latent variables. Minsley (2011) presented a 1-D trans-dimensional MCMC inversion (Malinverno, 2000) algorithm for FDEM data, in which the number of layers was assumed unknown. Their approach favours model parsimony between models that equally fit the data. This favouring of simple models is naturally accounted for in the so-called Ockham factor, which measures how much of the prior information is contained in the posterior pdf. With increasing number of parameters, the probability mass of the prior in the vicinity of

the posterior will typically decrease (and so will the Ockham factor), while the data fit will typically improve (Malinverno, 2002). Ray and Key (2012) used the same type of method to determine 1-D anisotropic resistivity profiles from marine CSEM data. Most recently, Buland and Kolbjørnsen (2012) jointly inverted synthetic CSEM and MT data and presented a real-world application for CSEM data. Khan *et al.* (2006) used EM data within a MCMC framework to constrain the composition and thermal state of the mantle beneath Europe.

The published contributions summarized thus far have demonstrated the ability of MCMC methods to (1) successfully converge to the global optimum of the parameter space, (2) treat nonlinear relationships between model and data and (3) adequately characterize parameter and model uncertainty. Yet, all these studies used relatively simple 1-D models to minimize the computational costs of the forward solution, and considered relatively low-dimensional parameter spaces to facilitate convergence of the MCMC sampler to the appropriate limiting distribution.

Grandis *et al.* (2002) presented the first published multidimensional MCMC inversion of MT data using a thin-sheet modelling code that is CPU-efficient, but only accurate for relatively thin anomalous bodies. Inversions were presented for a horizontal 2-D anomaly embedded in a known horizontally layered 1-D model. Chen *et al.* (2012) presented a MCMC algorithm to invert 2-D MT data. They fixed the number of layers in the model, yet allowed the depths to vary at given offsets. A 2-D resistivity structure was estimated at a geothermal site using 436 model parameters. This particular algorithm enables the inversion of 2-D data, but imposes strict constraints on the model parameterization in that only layered models with sharp boundaries are allowed.

Other global search methods of stochastic nature, such as simulated annealing (Kirkpatrick *et al.*, 1983) and genetic algorithms (Holland, 1992), have been used to produce 1-D and 2-D electrical resistivity models from MT data (Dosso and Oldenburg, 1991; Everett and Schultz, 1993; Pérez-Flores and Schultz, 2002). These methods fully account for the nonlinear relation between model and data, but are only concerned with finding the optimal model, without recourse to estimating the underlying posterior parameter distribution. Post-processing of the sampled trajectories can provide some insights into the remaining parameter uncertainty, but this type of analysis approach lacks statistical rigor.

More complex and highly parameterized 2-D or 3-D resistivity models are generally obtained through deterministic inversion (e.g. deGroot Hedlin and Constable, 1990; Siripunvaraporn and Egbert, 2000; Rodi and Mackie, 2001; Siripunvaraporn *et al.*, 2005). These algorithms are much more efficient but provide only a single "best" solution to the inverse problem (e.g. Menke, 1989). Approximate uncertainty estimates can be obtained through linearization in the vicinity of the final solution (Alumbaugh and Newman, 2000). As an alternative to such

approaches, Oldenburg and Li (1999) derived a set of different deterministic models using the same data set by running repeated deterministic inversions with different regularization constraints. Features that appear in all models are interpreted as being well resolved by the data. Jackson (1976) and Meju and Hutton (1992) constructed extremal models that fit the data up to a given data misfit threshold with a most-squares inversion. This approach derives the extremal deviations of each model parameter from a best-fitting model. Kalscheuer and Pedersen (2007) used truncated singular value decomposition (TSVD) to estimate the model parameter errors and resolution of models from radio magnetotelluric (RMT) data. Finally, Kalscheuer *et al.* (2010) used the same approach to compare the errors and resolution properties of the RMT data against those of a joint inversion with electrical resistivity tomography data (ERT) and ERT data alone. The aforementioned methods partly account for model nonlinearity but violate formal Bayesian principles, first, because the "best" model is found by minimizing an objective function rather than analyzing the variables marginal pdfs, and secondly because the estimated uncertainties are dependent on this best model, which in turn depends on the initial model used to find it (e.g. Chen *et al.*, 2008). This poses questions regarding the statistical validity of the estimated model and parameter uncertainty.

The purpose of the present paper is to investigate MCMC-derived parameter uncertainty and bias of a finely parameterized 2-D subsurface system for an increasing level of model constraints. In particular, we study how the posterior uncertainty changes when RMT data is inverted using (1) no constraints on the model structure, (2) smoothness constraints with different model norms and (3) joint inversion with ERT data. We also investigate the ability of the MCMC algorithm to retrieve the true measurement data errors and the regularization weight that provides appropriate weights to the model constraints.

The remainder of the paper is organized as follows: Section 3.3 presents the theoretical background of the proposed inversion approach. This is followed in Section 3.4 by the results of a synthetic model using different levels of model constraints and in Section 3.5 for a real world application using experimental data from an aquifer in Sweden. Section 3.6 discusses the implications of our results and highlights potential further developments. Finally, Section 3.7 concludes this paper with a summary of the presented work.

3.3 Methodology

3.3.1 Bayesian inversion

Let the physical system under investigation be described by a vector of M model parameters, $\mathbf{m} = (m_1, m_2, ..., m_M)$ and a set of N observations, $\mathbf{d} = (d_1, d_2, ..., d_N)$ which are theoretically related to the model via a set of equations,

$$\mathbf{d} = g(\mathbf{m}) + \mathbf{e}, \tag{3.1}$$

where $\mathbf{e}$ is a vector of dimension N, which contains measurement data errors and any discrepancies caused by the model parameterization, deficiencies in the forward function $g(\mathbf{m})$, etc. The posterior pdf $p(\mathbf{m}|\mathbf{d})$ of the model parameters, conditional on the data, can be obtained by applying Bayes theorem (Tarantola and Valette, 1982):

$$p(\mathbf{m}|\mathbf{d}) = \frac{p(\mathbf{m})p(\mathbf{d}|\mathbf{m})}{p(\mathbf{d})}, \tag{3.2}$$

where $p(\mathbf{d}|\mathbf{m})$ is the pdf of $\mathbf{d}$ conditional on $\mathbf{m}$, also called the likelihood function $L(\mathbf{m}|\mathbf{d})$, $p(\mathbf{m})$ is the prior pdf and $p(\mathbf{d})$ signifies the evidence. The evidence is a normalizing constant that is required for Bayesian model selection and averaging (e.g. Malinverno, 2002), but because our interests concern a fixed model parameterization, $p(\mathbf{m})$ can be removed without harm from eq. (3.2) leaving us with the following proportionality equality

$$p(\mathbf{m}|\mathbf{d}) \propto p(\mathbf{m})L(\mathbf{m}|\mathbf{d}), \tag{3.3}$$

The prior probability of the model vector, $p(\mathbf{m})$, represents the information known about the subsurface before collecting the actual data. It can be based on other types of geophysical measurements, geological information about the model structure, expected type of rocks and values of model parameters, etc. In the absence of detailed prior information about the subsurface properties, we assume a Jeffreys prior, that is, that the logarithm of each respective property is uniformly distributed(Jeffreys, 1998; Tarantola, 2005).

3.3.2 The likelihood function

The likelihood function summarizes the distance (typically a norm of a vector of residuals) between the model simulation and observed data. The larger the value of the likelihood, the closer the model response typically is to the experimental data. Under the assumption that the measurement data errors follow a normal distribution with zero mean, the likelihood function is given by (Tarantola, 2005)

$$L(\mathbf{m}|\mathbf{d}) = \frac{1}{(2\pi)^{N/2}\det(\Sigma)^{1/2}} \exp\left(-\frac{1}{2}\left(g(\mathbf{m}) - \mathbf{d}\right)^T \Sigma^{-1} \left(g(\mathbf{m}) - \mathbf{d}\right)\right), \tag{3.4}$$

where Σ is the data covariance matrix and $\det(\Sigma)$ denotes the determinant of Σ. If the errors are uncorrelated, then Σ is a diagonal matrix and $\det(\Sigma) = \prod_{1\leq i\leq N} \sigma_i^2$. The log-likelihood can then be expressed as

$$l(\mathbf{m}|\mathbf{d}) = -\frac{N}{2}\log(2\pi) - \frac{1}{2}\log\left(\prod_{1\leq i\leq N} \sigma_i^2\right) - \frac{1}{2}\phi_{d,2}, \tag{3.5}$$

where $\phi_{d,2} = \sum_{1\leq i\leq N} \left(\frac{g_i(\mathbf{m})-d_i}{\sigma_i}\right)^2$ represents the data misfit and σ_i denotes the standard deviation of the i-th measurement error. This misfit function is a measure of the distance between the forward response of the proposed model and the measured data, where the subscript 2

defines the l_2-norm. The first term in eq. (3.5) is a constant, and the measurement data errors can be assumed unknown and estimated jointly with the model parameters. This approach is also referred to as hierarchical Bayes (e.g. Malinverno and Briggs, 2004; Guo *et al.*, 2011). As the data misfit becomes smaller, the log-likelihood increases and the proposed model is more likely to be a realization from the posterior distribution. Given the assumptions of the data errors made thus far, the sum of squared errors should follow a chi-square distribution with expected value of N. To avoid data over- or underfitting, it is therefore necessary to have a posterior misfit pdf with the same expected value.

When the data errors deviate from normality, it is common to use an exponential distribution, which is consistent with an l_1-norm instead of an l_2-norm (Menke, 1989). Different publications have demonstrated that the l_1-norm is more robust against outliers, and often more realistic (e.g. Shearer, 1997; Farquharson and Oldenburg, 1998). When the measurement errors are independent, the corresponding exponential likelihood function is given by (Tarantola, 2005):

$$L(\mathbf{m}|\mathbf{d}) = \frac{1}{2^N \prod_{1\leq i\leq N} \sigma_i} \exp\left(-\sum_{1\leq i\leq N} \left|\frac{g_i(\mathbf{m}) - d_i}{\sigma_{d,i}}\right|\right), \tag{3.6}$$

which corresponds to the following formulation of the log-likelihood function

$$l(\mathbf{m}|\mathbf{d}) = -N\log(2) - \log\left(\prod_{1\leq i\leq N} \sigma_i\right) - \phi_{d,1}, \tag{3.7}$$

where the data misfit is now defined as $\phi_{d,1} = \sum_{1\leq i\leq N} \left|\frac{g_i(\mathbf{m})-d_i}{\sigma_i}\right|$. This distribution has much longer tails (e.g. Menke, 1989), thereby reducing the importance of outliers during parameter estimation.

3.3.3 Constraining the model structure

When strong a priori knowledge of a suitable model structure is lacking, one may invert for the model pdf by only providing each model parameter's likely range of variation as a priori information. An alternative is to also constrain the model structure to favour smooth spatial transitions. This is a common strategy in deterministic inversion (e.g. Constable *et al.*, 1987; deGroot Hedlin and Constable, 1990), where these constraints serve as a regularization term that decreases the ill-posedness of the inverse problem. In the Bayesian framework, the constraints can be included in the prior pdf (e.g. Besag *et al.*, 1995; Chen *et al.*, 2012).

To favour models with smoothly varying resistivity structures, we impose independent normal distributions to the horizontal and vertical model gradients. This results in the following constraint prior pdf (see Appendix A)

$$c_{m,2}(\mathbf{m}) = \frac{1}{(2\pi\alpha_y)^{M_y}} \frac{1}{(2\pi\alpha_z)^{M_z}} \exp\left[-\frac{1}{2}\left(\frac{1}{\alpha_y^2}\mathbf{m}^{\mathrm{T}}\mathbf{D}_y^{\mathrm{T}}\mathbf{D}_y\mathbf{m} + \frac{1}{\alpha_z^2}\mathbf{m}^{\mathrm{T}}\mathbf{D}_z^{\mathrm{T}}\mathbf{D}_z\mathbf{m}\right)\right], \tag{3.8}$$

where $\mathbf{D}_y$ and $\mathbf{D}_z$ signify the difference operators in the horizontal and vertical directions with rank M_y and M_z, respectively, $(M_y + 1)$ and $(M_z + 1)$ denote the number of horizontal and vertical grid cells, respectively, and α_y and α_z are the standard deviations of the model gradients in each spatial direction. If their expected values are similar for both directions, the constraint function becomes

$$\log(c_{m,2}(\mathbf{m})) = -(M_y + M_z)\log(2\pi\lambda^2)\frac{1}{2}\phi_{m,2}, \tag{3.9}$$

where $\phi_{m,2} = \frac{1}{\lambda^2}\left(\mathbf{m}^{\mathrm{T}}\mathbf{D}_y^{\mathrm{T}}\mathbf{D}_y\mathbf{m} + \mathbf{m}^{\mathrm{T}}\mathbf{D}_z^{\mathrm{T}}\mathbf{D}_z\mathbf{m}\right)$ and $\lambda = \alpha_z = \alpha_y$ is a hyperparameter to be determined using MCMC simulation. This latter variable bears much resemblance with model regularization weights used in deterministic inversions, and hence will be referred to as such hereafter. Note also that the right-hand side term in eq. (3.9) is essentially the model regularization term proposed by deGroot Hedlin and Constable (1990). The smaller the value of λ, the higher the weight given to the regularization term.

Sharper spatial model transitions than those obtained by the least-squares smoothness constraints may be sought. In classical deterministic inversions, sharp transitions are usually imposed by applying alternative model norms (e.g. Farquharson, 2007; Rosas Carbajal *et al.*, 2012). Similar to how an exponential pdf was used to obtain more robust data misfit measures, here we apply it to increase the likelihood of models whose properties change abruptly from one cell to the next:

$$c_{m,1}(\mathbf{m}) = \frac{1}{(2\alpha_y)^{M_y}}\frac{1}{(2\alpha_z)^{M_z}}\exp\left[-\left(\frac{\|\mathbf{D}_y\mathbf{m}\|_1}{\alpha_y} + \frac{\|\mathbf{D}_z\mathbf{m}\|_1}{\alpha_z}\right)\right], \tag{3.10}$$

where a l_1-norm is used (subscript) for the smoothness constraints. In the case that $\alpha_z = \alpha_y = \lambda$, the log-distribution of eq. (3.10) becomes

$$\log(c_{m,1}(\mathbf{m})) = -(M_y + M_z)\log(2\lambda)\frac{1}{\lambda}\left(\|\mathbf{D}_y\mathbf{m}\|_1 + \|\mathbf{D}_z\mathbf{m}\|_1\right), \tag{3.11}$$

The l_1-norm linearly weights the differences of the properties of adjacent cells. This is different from an l_2-norm that squares these differences, and hence an l_1-norm is less sensitive to sharp transitions between neighbouring cells.

3.3.4 Forward computations

To compute the likelihood functions described in the previous section, a numerical solver is needed to simulate the geophysical response of each proposed model. For both geophysical methods considered herein, the RMT and ERT responses are described by Maxwell's equations. In the general case, the model parameters and electromagnetic field vary dynamically in a 3-D space. The higher the resolution of the resolved spatial dimension and the larger the number of model parameters, the more demanding the forward problem. Despite significant advances in computational power, 3-D MCMC inversion remains a daunting computational task. We

therefore focus our attention on a 2-D model of the subsurface and compute the 2.5D ERT and RMT forward responses using finite-difference approximation. A detailed description of the forward solvers can be found in Kalscheuer *et al.* (2010), and interested readers are referred to this publication for additional details about the numerical setup and solution.

3.3.5 MCMC strategy for high-dimensional problems

For high-dimensional and non-linear inverse problems, it is practically impossible to analytically derive the posterior distribution. We therefore resort to MCMC sampling methods that iteratively search the space of feasible solutions. In short, MCMC simulation proceeds as follows. An initial starting point, mold is drawn randomly by sampling from the prior distribution. The posterior density of this point is calculated by evaluating the product of the likelihood of the corresponding simulation and prior density. A new (candidate) point, $\mathbf{m}_{new}$ is subsequently created from a proposal distribution that is centred around the current point. This proposal is accepted with probability (Mosegaard and Tarantola, 1995):

$$P_{accept} = \min\left\{1, \exp[l(\mathbf{m}_{new}|\mathbf{d}) - l(\mathbf{m}_{old}|\mathbf{d})]\right\}, \tag{3.12}$$

If the proposal is accepted the Markov chain moves to $\mathbf{m}_{new}$, otherwise the chain remains at its old location. After many iterations, the samples that are generated with this approach are distributed according to the underlying posterior distribution. The efficiency of sampling is strongly determined by the scale and orientation of the proposal distribution. If this distribution is incorrectly chosen, then the acceptance rate of candidate points might be unacceptably low, resulting in a very poor efficiency. On the contrary, if the proposal distribution is chosen accurately, the MCMC sampler will rapidly explore the posterior target distribution.

In this work, we use the MT-DREAM$_{(ZS)}$ algorithm (Laloy and Vrugt, 2012), which was especially designed to efficiently explore high-dimensional posterior distributions. This is an adaptive MCMC algorithm (e.g. Roberts and Rosenthal, 2007), which runs multiple chains in parallel and combines multiple-try sampling (Liu *et al.*, 2000) with sampling from an archive of past states (Vrugt *et al.*, 2009, see also Vrugt *et al.*, 2008) to accelerate convergence to a limiting distribution. Furthermore, it is fully parallelized and especially designed to run on a computer cluster. The MT-DREAM$_{(ZS)}$ algorithm satisfies detailed balance and ergodicity, and is generally superior to existing MCMC algorithms (Laloy and Vrugt, 2012). To assess convergence, the Gelman-Rubin statistic (Gelman and Rubin, 1992) is periodically computed using the last 50 percent of the samples in each of the chains. Convergence to a limiting distribution is declared if the GelmanRubin statistic is less than 1.2 for all parameters. After convergence, we use the last 25 percent of the samples in each chain to summarize the posterior distribution.

3.3.6 Uncertainty estimation with most-squares inversion

Most-squares inversion (Jackson, 1976; Meju and Hutton, 1992) is a deterministic inversion approach where extremal models are sought that fit the data up to a given threshold. First, a best-fitting model $\mathbf{m}_0$ is calculated. Next, a particular cell of the model is chosen and the most-squares inversion is used to find the extremal values of this cell that satisfy a data misfit threshold $\phi^2_{d,2} = \phi_{d,2}[\mathbf{m}_0] + \Delta\phi$. All model cells are allowed to vary and two different searches are initiated to derive the smallest and largest acceptable resistivities. If we choose $\Delta\phi = 1$ it can be shown that this results in extremal values that deviate one standard deviation from the best-fitting model (e.g. Kalscheuer *et al.*, 2010). Most-squares inversion has been used to test the validity of other non-linear yet deterministic variance estimates, such as inversion schemes based on singular value decomposition (Kalscheuer and Pedersen, 2007). Furthermore, it can also be applied with regularization constraints using the same model regularization weight used to derive the best-fitting model and modifying the threshold misfit to $\phi^t_{d,2} = \phi_{d,2}[\mathbf{m}_0] + (1/\lambda^2)\phi_{m,2} + \Delta\phi$. The mean and uncertainty of the different cells derived from the most-squares inversion results are compared against their estimates from MCMC simulation.

3.4 Synthetic Examples

To evaluate the impact of the model constraints and data on the posterior pdf, we consider a synthetic 2-D resistivity model. This study is similar to the one presented by Kalscheuer *et al.* (2010). Two resistors and two conductors with thicknesses of 10 m (Fig. 3.1 a) are immersed in a homogeneous medium of 100 Ωm. A conductor of 10 Ωm and 50m length overlays a 1000 Ωm and 30-m long resistor at symmetric positions, and a resistor of 1000 Ωm and 50m length overlays a 10 Ωm and 30-m long conductor, respectively. The transverse electric (TE) and transverse magnetic (TM) mode responses of this configuration were computed for the 17 different stations shown in Fig. 3.1 (a). A total of 8 frequencies, regularly spaced on a logarithmic scale in the frequency range of 22-226 kHz were used, which resulted in a total of 544 data points. These synthetic observations were subsequently corrupted with a Gaussian measurement data error with standard deviation equal to 3 percent of the simulated impedances. To explicitly investigate the effect of the probabilistic properties of the measurement data errors, we also created a second data set by perturbing the error-free simulated forward responses with a zero-mean exponential distribution and a similar mean deviation of 3 percent of the modelled impedances. Unless stated differently, we refer to the RMT data as the data set contaminated with Gaussian noise in the remainder of this paper. To generate the synthetic ERT data, forward and reverse poledipole configurations were considered with electrodes placed at the positions of the 17 different RMT stations. Similarly to Kalscheuer *et al.* (2010), four expansion factors (1, 2, 4 and 6) and a basic potential electrode distance of 10 m, and level values of $n = 1, ..., 7$ for a fixed potential electrode distance were used. This resulted in a data set consisting of 306 different artificial observations. To mimic the effect

of measurement data errors, the simulated data were again perturbed with a Gaussian error using a standard deviation of 3 percent of the simulated apparent resistivities. The model discretization used in the MCMC inversions is shown in Fig. 3.1(a). Each cell has dimensions of 5 × 10 m^2, but the cells located at the left, right and bottom edges of the domain extend until "infinity" (i.e. to accommodate the imposed boundary conditions). This results in a total of 228 different resistivity values that need to be estimated from the experimental data.

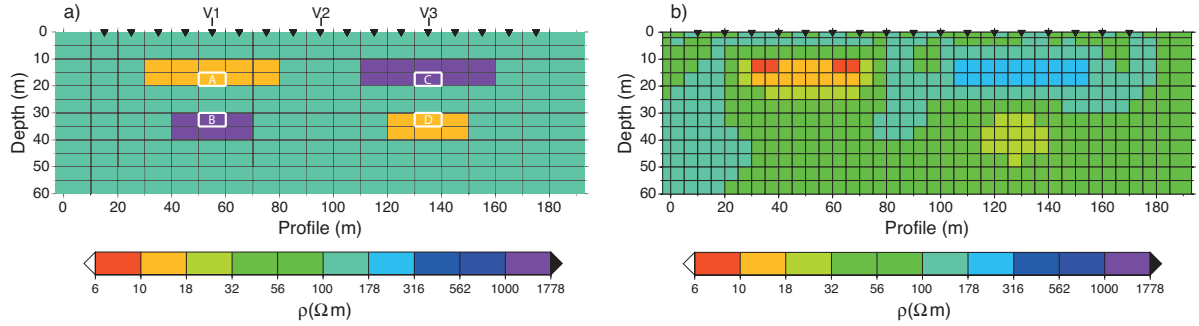

Figure 3.1: (a) Synthetic test model with the MCMC model discretization highlighted. Letters A, B, C and D indicate cells for which the inversion results are evaluated against those of deterministic most-squares inversions. Numbered letters V1, V2 and V3 indicate the offsets at which the resistivity marginal posterior pdfs are presented. (b) Model obtained by inverting RMT data (3 percent error on the impedance elements) with a smoothness constrained deterministic inversion. The mesh in (b) corresponds to the model discretization of the deterministic inversions and the forward modelling mesh. The triangles at the top of the figures indicate the locations of the RMT stations and the ERT electrodes.

Fig. 3.1 (b) plots the final model derived from the RMT data using a classical deterministic inversion with smoothness constraints (cf. deGroot Hedlin and Constable, 1990). This model was obtained after three iterations and has a misfit of $\phi_{d,2} = 533$, assuming a 3 percent error of the impedance values. A homogenous half-space of 100 Ωm was used as the starting model. The inversion successfully retrieves the two shallow blocks, and indicates the presence of the deep conductor. However, it shows no evidence of the deep resistor. The resistivity value of the shallow conductor is well defined, but the magnitude of the resistor is underdetermined.

We now summarize the results of MCMC simulation using the different penalties of the model structure described previously in Section 3.3. Following recommendations made by Laloy and Vrugt (2012), we use three different chains and simultaneously create and evaluate five candidate points in each individual chain. To maximize computational efficiency, we run MT-DREAM$_{(ZS)}$ in parallel using 16 different processors. Fifteen processors are used to simultaneously evaluate the different proposals, and achieve a linear speed up, whereas the remaining processor serves to execute the main algorithmic tasks of MT-DREAM$_{(ZS)}$. We invert for the log-resistivity values, and use a Jeffreys prior in the range of 100.5 to 103.5 m. We also invert for the hyperparameter r, which represents the standard deviation of the measurement data

errors as a percentage of the measured impedances. We use a Jeffreys prior for r as well, and define its upper and lower bound as half and double its true value (i.e. 1.5-6 percent). Appendix B details the log-likelihood that is used to estimate r from the RMT data.

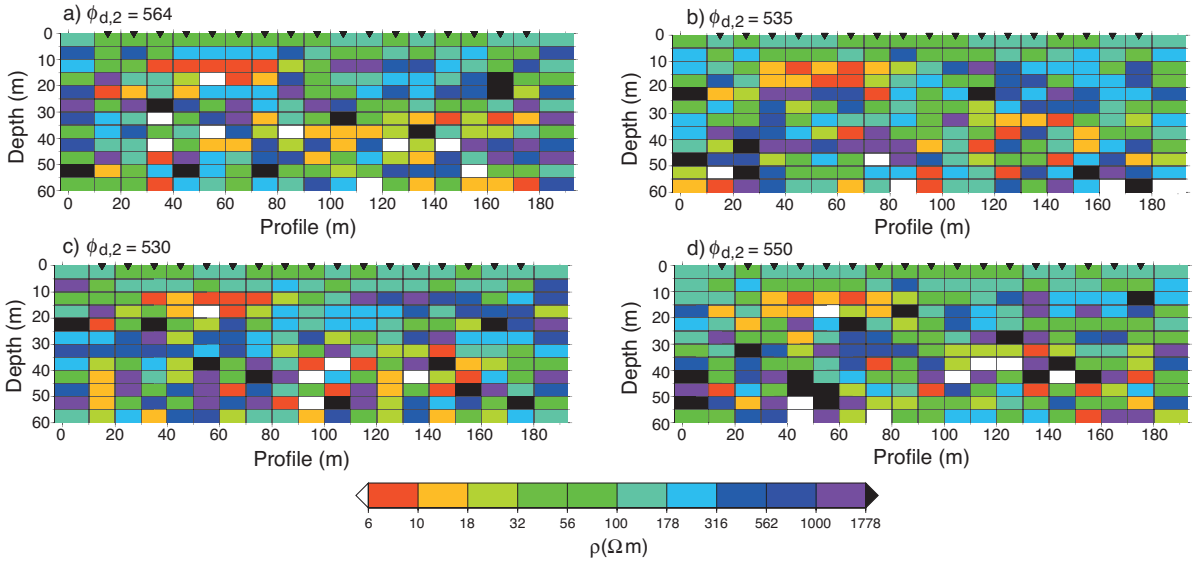

Figure 3.2: (a-d) Posterior MCMC realizations from the inversion of RMT data with no model constraints other than minimal and maximal parameter bounds of $\rho = 100.5$ and 103.5 m, respectively. It is very difficult to identify a clear correlation between these realizations and the true underlying model in Fig. 3.1 (a).

In the first MCMC trial, no constraints on the model structure (see eq. 3.23) were specified. Convergence of the chains was reached after about 100 000 computational time units (CTUs, cf. Laloy and Vrugt, 2012). Note that a single update of each of the parallel chains requires two CTUs, one for the evaluation of the candidate points, and one for the calculation of the posterior density of the reference set. To provide insights into the properties of the posterior resistivity distribution, Fig. 3.2 displays four randomly chosen posterior models. The corresponding data misfit is also listed. The models exhibit an extreme variability and the only structure that is clearly persistent in all four realizations is the shallow conductor. Figs 3.3(a-c) depict ranges of the marginal posterior pdf of the resistivity of three vertical profiles. As expected, these results illustrate that model variability increases with depth. The first 20 m appear rather well constrained by the data, but the uncertainty of the resistivity significantly increases beyond this depth. The data misfit and marginal posterior pdfs of the impedance error are represented with histograms in Figs 3.3(d) and (e), respectively. The marginal distribution of the data misfit is centred on its a priori expected value of N, a finding that inspires confidence in the ability of MT-DREAM$_{(ZS)}$ to converge to the adequate parameter values. In other words, the proposed models do not systematically over or under fit the calibration data. Note also that the standard deviation of the relative data error is well resolved with mean value of $r = 0.03$ and standard deviation of 0.001 (see Fig. 3.3e).

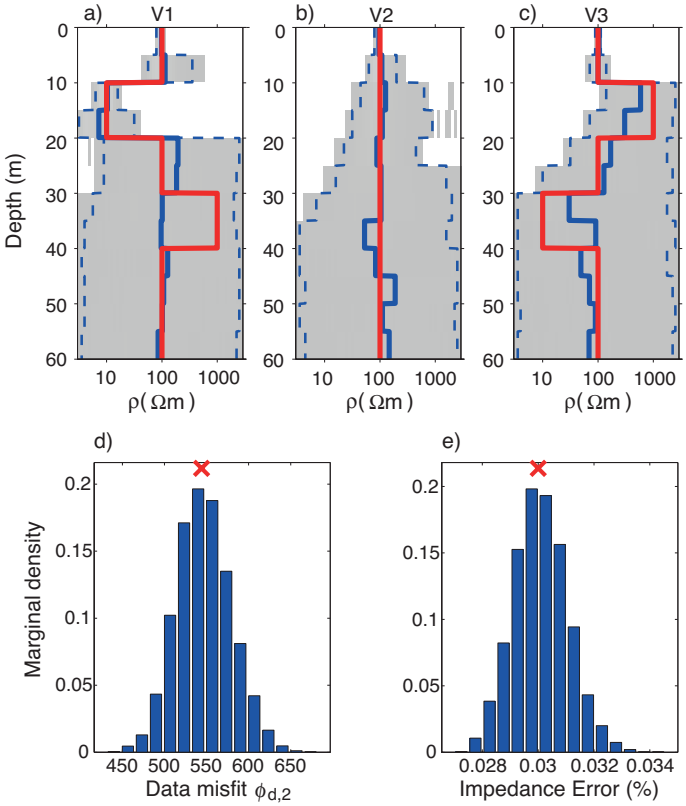

Figure 3.3: MCMC inversion of RMT data without model constrains. (a-c) Marginal posterior pdf of the vertical profiles V1, V2 and V3 corresponding to the offsets (a) 55 m, (b) 95 m and (c) 135 m. The red line represents the true values, while the solid and dashed blue lines represent the mean and P2.5 and P97.5 percentiles, respectively. It is seen that below 30 m the posterior models span the full prior range of resistivity. Grey colour-coding indicates the full posterior pdf range. Histograms of the (d) data misfit and (e) the inferred impedance error marginal posterior pdf. The red crosses at the top of the histograms depict the values corresponding to (d) the data misfit of the true model and (e) the true error standard deviation.

To determine whether model constraints about the considered subsurface influence the efficiency and robustness of MCMC simulation, a second inversion was performed in which smoothly varying resistivity structures were favoured by including eq. (3.9) in the prior pdf. The prior distribution in this case is then the same Jeffreys distribution as before with the same parameter ranges, but multiplied by the exponential of eq. (3.9). The regularization weight, λ was assumed to follow a Jeffreys prior with range of half and two times the optimal value derived by fitting a normal distribution (eq. A2) to the true log-resistivity model. For convenience, we further assumed a similar value of λ in both the vertical and horizontal direction.

Numerical results show that convergence was achieved after approximately 75 000 CTUs. Figure 3.4 illustrates that the posterior realizations exhibit far less spatial variability than those

previously derived for the unconstrained case without smoothness constraints, although the models are visually quite different. This is further confirmed by the vertical resistivity profiles depicted in Figs. 3.5(a-c). Model parameter uncertainty has significantly reduced, but with the side effect that some features of the true model are no longer accurately represented in the posterior pdf. Indeed, the two conductors and the shallow resistor are clearly detected, but the deep resistor is not adequately resolved. Yet, the MCMC inferred resistivity increases with depth, which is consistent with the observations. The marginal distribution of the data misfit presented in Fig. 3.5(d) again nicely centres on the true value, and is quite similar to the unconstrained inversion trial. The same is true for the data error estimation (Fig. 3.5f): the true value is obtained and the variability is similar to that previously observed in Fig. 3.3(e). The estimated value of λ is slightly larger than its previous counterpart derived from the true log-resistivity model. This finding is to be expected and is a direct consequence of the influence of the data misfit term in the estimation (i.e. less weight is put on the model constraints).

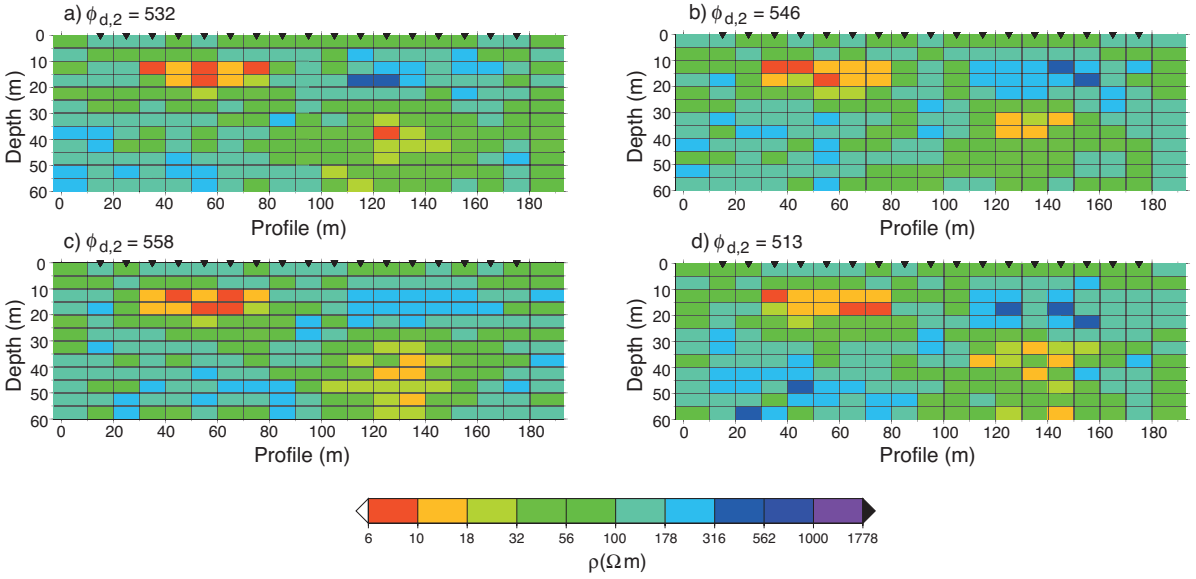

Figure 3.4: (a-d) Posterior MCMC realizations obtained by inverting the RMT data with least-squares smoothness constrains. All the four anomalous bodies are somewhat indicated, even if it is only the upper left conductive body that is well resolved.

We now summarize the MCMC results with an l_1 measure (see eq. 3.11) for the model constraints. For this inversion, we use a data set contaminated with exponentially distributed errors and log-likelihood function given by eq. (3.7). For consistency, we again use a Jeffreys prior for all regular model parameters (resistivities) and hyperparameters (regularization weight and impedance error). The resistivity and impedance error prior bounds remain the same as in the past examples, but the prior of the regularization weight ranges from half (0.055) to four (0.44) times the value found by fitting eq. (3.11) to the true resistivity model. We purposely increased the upper bound of λ so that the posterior pdf was unaffected by the

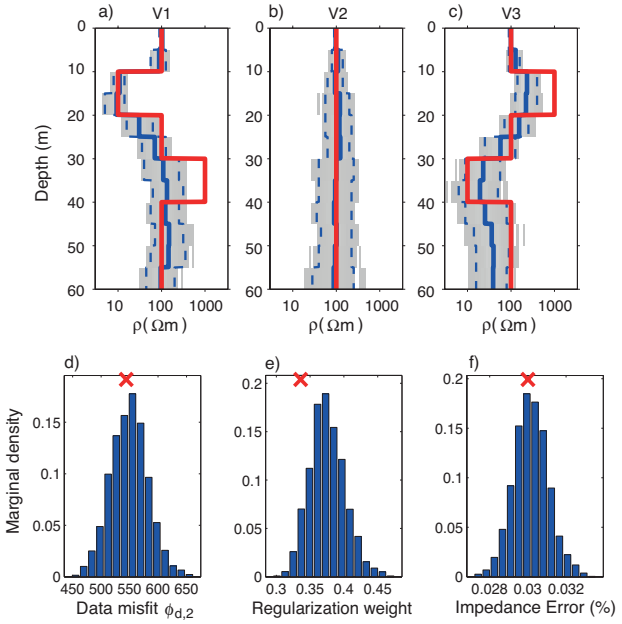

Figure 3.5: MCMC inversion of RMT data with least-squares smoothness constrains. (a-c) Marginal posterior pdfs of the vertical profiles V1, V2 and V3 corresponding to the offsets (a) 55 m, (b) 95 m and (c) 135 m. The red line represents the true values, while the solid and dashed blue lines represent the mean and P2.5 and P97.5 percentiles, respectively. Grey colour-coding indicates the full posterior pdf range. It is clear that the smoothness constraints have largely decreased model variability. Histograms of the (d) data misfit, (e) regularization weight and (f) impedance error marginal posterior pdf. The red crosses at the top of the histograms depict (d) and (f) the true values and (e) the value given by fitting eq. (3.9) to the true log-resistivity model.

a priori bounds.

About 67 000 CTUs were needed to declare convergence to a limiting distribution. The posterior realizations presented in Fig. 3.6 are rather homogeneous, and display even less variability than their counterparts previously depicted in Fig. 3.4 using the least-squares model constraints. The two shallow features are clearly identified, and a deep conductor can be seen in three of the four figures. The deep resistor however is not evident in any of the models. This becomes more evident if we plot the three depth profiles (Figs. 3.7a-c). The 95 percent posterior uncertainty ranges are comparable to those obtained with the inversion using the l_2 model constraints. The data misfit and the impedance errors are very well recovered. However, the posterior mean of λ is substantially larger than its value derived from fitting the true model structure to an exponential model (0.11).

Finally, we jointly invert the RMT and ERT data using least-squares smoothness constraints. In this particular case, the log-likelihood function is given by the sum of those corresponding to each data set. A derivation of the ERT likelihood is presented in Appendix C. This inversion includes the ERT data error, which constitutes a new hyperparameter to be estimated. We

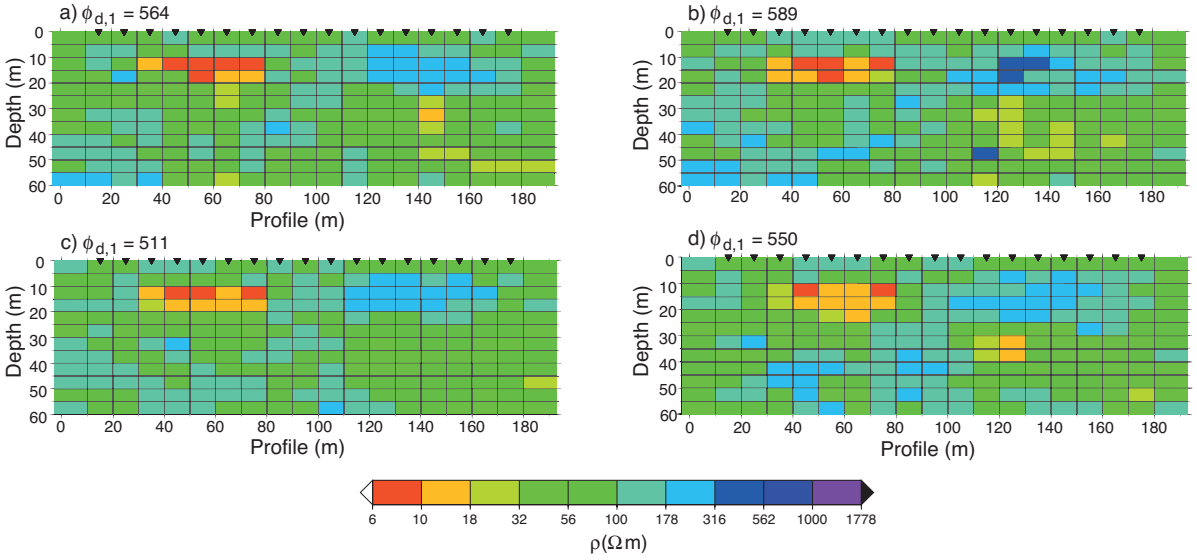

Figure 3.6: (a-d) Posterior MCMC realizations obtained by inverting the RMT data with l_1 smoothness constrains. The upper anomalous bodies are resolved, but not the lower ones.

use a Jeffreys prior for this parameter, with bounds given by half and twice its true value.

Convergence of the chains was achieved after about 60 000 CTUs. The posterior realizations shown in Fig. 3.8 clearly resolve the two conductors and the two resistors. The vertical resistivity profiles presented in Figs 3.9a-c confirm that joint inversion improves parameter convergence. Yet, the resistor below the conductor (Fig. 3.9a) is not particularly well resolved. However, its magnitude is much better estimated than in the previous inversions. The model constraints enforce smooth transitions from the conductor to the resistor and vice versa, which complicates estimation of the actual magnitudes in the vicinity of these transitions (e.g. Fig. 3.9c below the conductor). The posterior histograms of the RMT (Fig. 3.9d) and ERT data (Fig. 3.9e) misfits are closely centred on their true values, a desirable finding that indicates that both data types are equally important in the fitting of the parameters. The marginal posterior distribution of the regularization weight (Fig. 3.9f) demonstrates a tendency towards somewhat larger values than obtained from the RMT data. This is not surprising, as new data have been added to the likelihood function. For completeness, Figs 3.9(g) and (h) plot histograms of the impedance and apparent resistivity error. The posterior ranges encompass the synthetic true values, although the most likely (expected) values are somewhat smaller. This demonstrates that the measurement errors of both data types can be successfully retrieved from the joint inversion presented herein.

To provide more insights into the behaviour of the MT-DREAM$_{(ZS)}$ algorithm, Fig. 3.10 presents the evolution of the sampled model structure in one randomly chosen chain as a function of the number of MCMC realizations. The true value and those inferred from the different

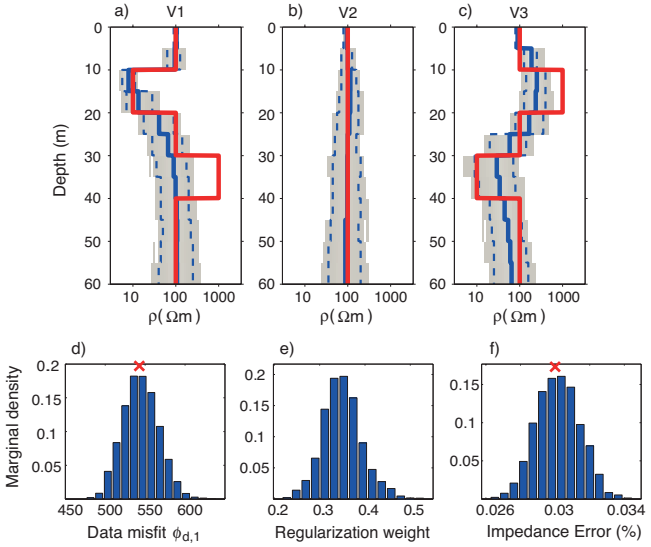

Figure 3.7: MCMC inversion of RMT data with l_1 smoothness constrains. (a-c) Resistivity marginal posterior pdf of the vertical profiles V1, V2 and V3 corresponding to the offsets (a) 55 m, (b) 95 m and (c) 135 m. The red line represents the true values, while the solid and dashed blue lines represent the mean and P2.5 and P97.5 percentiles, respectively. Grey colour-coding indicates the full posterior pdf range. The parameters' uncertainties are comparable to those of the l_2 smoothness constrains. Histograms of the (d) data misfit, (e) regularization weight and (f) impedance error marginal posterior pdf. The red crosses at the top of the histograms of (d) and (f) depict the true values. (e) The value given by fitting eq. (3.11) to the true log-resistivity model (0.11) is not comprised in the marginal posterior pdf.

MCMC trials are given by the l_2-norm of the difference operator applied to the model vector in the horizontal and vertical directions (i.e. the term enclosed in parentheses in eq. 3.9). We restrict our attention to the posterior samples, thus after burn-in (cf. Laloy and Vrugt, 2012) has been achieved.

The MCMC inversion without model constrains (Fig. 3.10a) converges to a model structure that overestimates the actual variability observed in the true model. The true model is not contained in the sampled posterior pdf. When smoothness constraints are explicitly included in the formulation of the log-likelihood function, the posterior models converge much closer to the true model, but with insufficient structure. This is particularly true if the l_1 norm is used. The average model structure in this case is 24, which is about half the true value. The correspondence between the true model and posterior realizations improves somewhat if an l_2 norm is used. Indeed, the sampled chain trajectory moves closer to the dashed black line, but nevertheless the actual model variability is still underestimated. Fortunately, a joint inversion of RMT and ERT data provides posterior realizations with properties similar to that of the true model, especially if an l_2 norm is used for the model constraints.

Table 3.1 lists the centre values and standard deviations estimated with the MCMC and

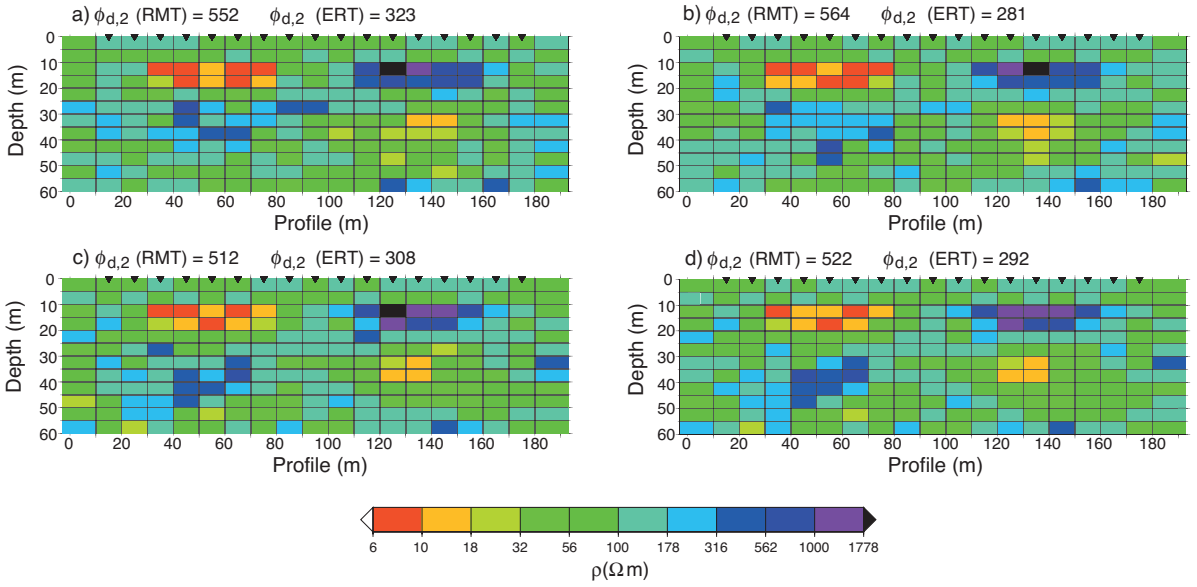

Figure 3.8: (a-d) Posterior MCMC realizations obtained by joint inversion of RMT and ERT data with least-squares smoothness constrains. The anomalous bodies are better defined compared with the inversions of RMT data alone (see Fig. 3.4).

most-squares inversions for the cells shown in Fig. 3.1(a). To enable a comparison between both methods, we calculate two different standard deviations from the posterior mean MCMC model: one for resistivity decrease and one for resistivity increase. We performed three most-squares inversions: one for the RMT data with smoothness constraints, one for the ERT data with smoothness constraints, and one for joint inversion with smoothness constraints. To find the best-fitting models, we locate that sample of the MCMC chains with largest value of the sum of eqs (3.5) and (3.9). This model was then used to initiate a deterministic inversion with additional Marquardt-Levenberg damping (cf. Kalscheuer *et al.*, 2010) to attempt to find a model with an even larger summed log-likelihood. This model was then used by the most-squares inversion to find the extremal values of each cell. In both inversion steps, we used the mean model regularization weight determined by the MCMC inversions. As seen in Fig. 3.1(b), the model discretization is finer in the horizontal direction for the most-squares inversion. At each iteration we therefore averaged the two resistivities involved in each particular cell to force a single resistivity value and make it comparable to the MCMC inversion cell.

The standard deviations summarized in Table 3.1 show that the two types of inversions provide similar uncertainty estimates. However, the standard deviations derived with the most-squares inversion are consistently larger than those derived with MCMC simulation. For example, in the single inversions of the RMT data, cell B has standard deviations of 0.18/0.19 for the MCMC inversion, and 0.24/0.24 for the most-squares inversion, respectively. These differences appear larger for the joint inversion. For instance, cell A has standard deviations of 0.08/0.08

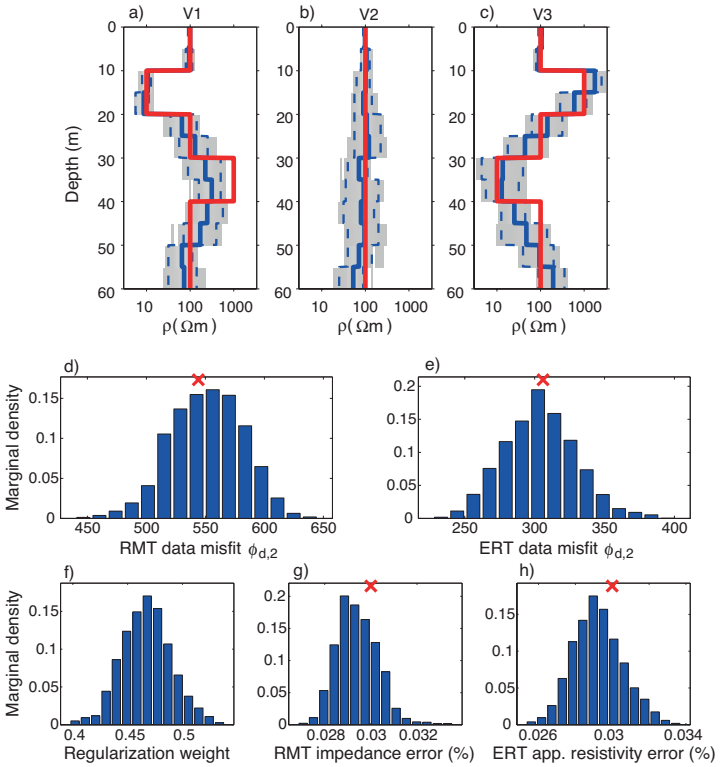

Figure 3.9: MCMC joint inversion of RMT and ERT data with least-squares smoothness constrains. (a-c) Resistivity marginal posterior pdfs of the vertical profiles V1, V2 and V3 corresponding to the offsets (a) 55 m, (b) 95 m and (c) 135 m. The red line represents the true values, while the solid and dashed blue lines represent the mean and P2.5 and P97.5 percentiles, respectively. Grey colour-coding indicates the full posterior pdf range. The range of the posterior pdf is rather small, but covers essentially the true model. Histograms of the (d) RMT data misfit, (e) ERT data misfit, (f) regularization weight, (g) RMT impedance error and (h) ERT apparent resistivity error marginal posterior pdfs. The red crosses at the top of the histograms depict (d), (e), (g) and (h) the true values and (f) the value given by fitting eq. (3.9) to the true log-resistivity model.

with the MCMC inversion, but with the most-squares inversion these values are doubled. Furthermore, we see that the mean value estimates are quite different for the two types of inversion. For example, the mean value of cell A for the ERT data and MCMC inversion is 1.0, whereas its counterpart derived from the most-squares inversion is 1.16. Thus, although the width of the uncertainty ranges can be quite similar, the mean value might induce shifts in the posterior distribution.

3.5 Field data Example: Skediga Area (Sweden)

We now apply our methodology to real-world RMT data. A tensor RMT survey was conducted in Skediga (Sweden) to determine the geometry of a glaciofluvial aquifer system composed of a sand/gravel formation overlying crystalline basement. The aquifer system is overlain by a

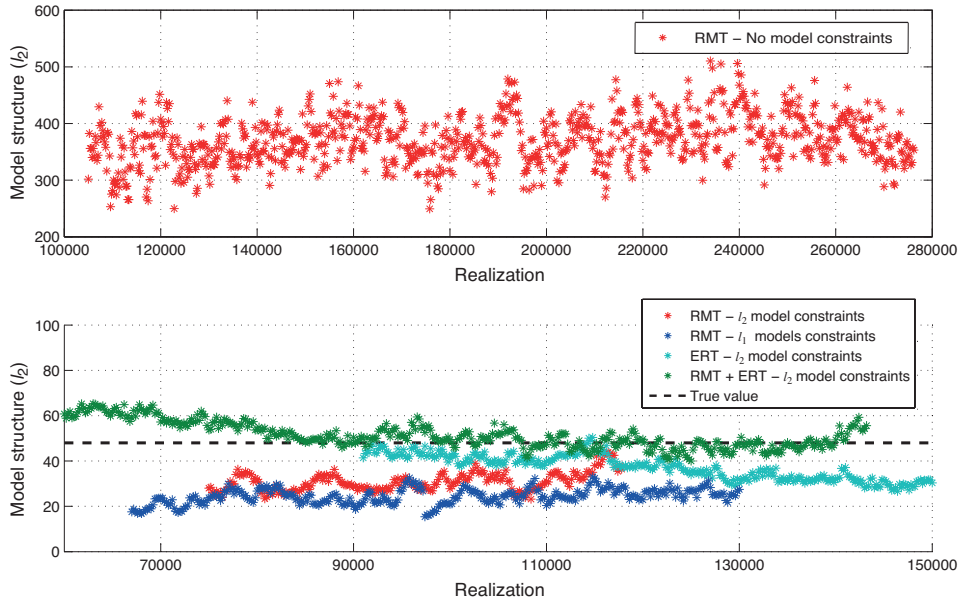

Figure 3.10: Posterior least-squares model structure metric as a function of realization number for the different types of MCMC inversions considered. (a) MCMC inversion of RMT data without model constrains. This inversion needs many more realizations to converge than all other cases and has a much larger average model structure. (b) MCMC inversions with model constraints. The dashed black line represents the true value. The joint inversion of RMT and ERT is the only case that proposes models with the same amount of model structure as the true model.

formation dominated by clay lenses. We use the same RMT data as Kalscheuer and Pedersen (2007), that is, 528 data points consisting of apparent resistivities and phases of the determinant mode (Pedersen and Engels, 2005), acquired at 22 different stations using 12 frequencies in the range of 4-181 kHz. An estimate of the data error was provided by the impedance estimation from the electric and magnetic field measurements and an error floor of 1.5 percent was used as in the previous studies (Pedersen *et al.*, 2005; Kalscheuer and Pedersen, 2007). The error floor constitutes a lower bound to the estimated data errors such that no single data has an error estimate smaller than this value.

Fig. 3.11(a) shows the model obtained by Kalscheuer and Pedersen (2007) derived from a deterministic inversion with smoothness constraints using a half-space of 1000 m as the initial model. The model was obtained after four iterations and has a data misfit of $\phi_{d,2} = 1141$. Pedersen *et al.* (2005) interpret the 30 Ωm isoline (i.e. the transition between the two greenish colours) as the lower bound of the clay lenses. According to boreholes in the vicinity of the profiles, the transition from the aquifer to the underlying crystalline basement occurs at about 30 m depth (Kalscheuer and Pedersen, 2007).

We ran the MT-DREAM$_{(ZS)}$ algorithm on a 2-D domain consisting of 288 model parameters using the l_2 smoothness constraints. Each resistivity cell is of size 5 ×10 m, except for the

Table 3.1: Mean values and standard deviations of the cells highlighted in Fig. 3.1(a) for individual and joint MCMC and most-squares (MS) inversions with different types of model constraints. The centre values are the mean values for the MCMC inversions and the parameter derived from the best-fitting MCMC model for the most-squares inversions (cf. Section 3.4 for details). The standard deviations (SD) are given in logarithmic units that are calculated individually for each side of the centre value (-/+).

Type of inversion	Model constraint	Cell A		Cell B		Cell C		Cell D	
		Centre $\log_{10}\rho(\Omega\text{m})$	SD(-/+) $\log_{10}\rho(\Omega\text{m})$	Centre $\log_{10}\rho(\Omega\text{m})$	SD(-/+) $\log_{10}\rho(\Omega\text{m})$	Centre $\log_{10}\rho(\Omega\text{m})$	SD(-/+) $\log_{10}\rho(\Omega\text{m})$	Centre $\log_{10}\rho(\Omega\text{m})$	SD(-/+) $\log_{10}\rho(\Omega\text{m})$
Individual RMT MCMC	l_2-diff.	0.97	0.12/0.11	2.04	0.18/0.19	2.36	0.11/0.15	1.36	0.21/0.21
Individual RMT MS	l_2-diff.	0.98	0.15/0.12	1.90	0.24/0.24	2.36	0.19/0.17	1.36	0.22/0.26
Individual ERT MCMC	l_2-diff.	1.00	0.10/0.09	2.00	0.12/0.10	2.65	0.11/0.11	2.05	0.14/0.14
Individual ERT MS	l_2-diff.	01.16	0.17/0.17	1.63	0.23/0.24	2.64	0.18/0.18	2.12	0.23/0.23
Joint MCMC	l_2-diff.	0.94	0.08/0.08	2.35	0.18/0.18	2.78	0.17/0.15	1.13	0.23/0.25
Joint MS	l_2-diff.	0.99	0.15/0.16	2.18	0.25/0.35	3.11	0.20/0.18	1.05	0.22/0.26
True values	-	1.00	N/A	3.00	N/A	3.0	N/A	1.00	N/A

edges that extend to the end of the forward mesh (1300 m in each direction). We used Jeffreys priors in the range of 100.5 to 103.5 of $\rho(\Omega\text{m})$. In addition, we estimated two hyperparameters: the regularization weight λ and a data error correction factor. The latter represents a scaling factor of the errors and error floor. We assume a Jeffreys prior for this scaling factor, with ranges between the logarithms of 0.5 and 4.

Convergence was reached after approximately 150 000 CTUs. Figures 3.11(b) and (c) show two realizations from the MCMC derived posterior pdf. The two models clearly indicate two shallow conductors at profile offsets of 40 m and between 170 and 220 m. A deep resistor is also found that is deeper on the left side of the profile than in the middle and that disappears on the right side. A mean posterior model was constructed by taking the mean value of the different realizations of the posterior pdf (Fig. 3.11d). This model is largely comparable to the model obtained by the deterministic inversion; the claysand/gravel transitions are located at similar depths nearly everywhere along the profile and the overall basement geometry of the two different models corresponds well (this was also noted with the ensemble mean of the synthetic example using least squares smoothness constraints compared to Fig. 3.11(b), not shown here). Some deviations are possibly due to difference in model discretization, but may more probably be due to differences in data fitting, as discussed below.

We present four vertical profiles of the posterior pdf in Figs 3.12(a-d), at offsets (a) y= 50 m, (b) y= 100 m, (c) y= 150 m and (d) y= 200 m. As expected, the profiles show an increase

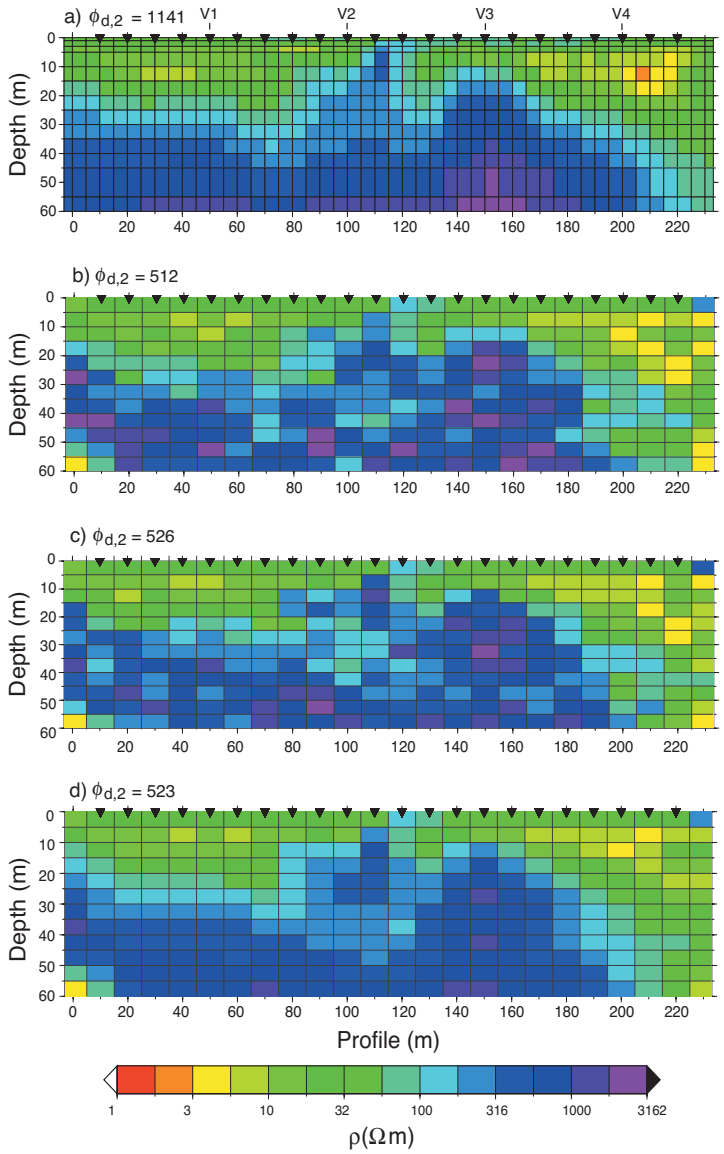

Figure 3.11: (a) Deterministic inversion model obtained from RMT data acquired at Skediga, Sweden (modified after Kalscheuer and Pedersen, 2007). Numbered letters V1, V2, V3 and V4 indicate the offsets at which the resistivity marginal posterior pdfs are presented in Fig. 3.12. (b)(c) Posterior MCMC realizations obtained by inversion of the same data with least-squares smoothness constrains. (d) Ensemble posterior mean model from MCMC inversion. The data misfits are calculated with errors inferred from the mean value of Fig. 3.12(e). Note the strong similarity between the models in (a) and (d).

in model variability below the conductive clay lenses. Furthermore, we see how the clay-sand/gravel transitions are much better determined at places where the aquifer stretches up to the surface (Figs. 3.12b and c). In these regions there is no overlapping between the two resistivity intervals, whereas in the other two profiles the transition happens more smoothly, probably due to the model constraints. Also the transition to a fixed basement resistivity is smooth because of the model regularization. Magnitudes are expected to be above $\rho =$

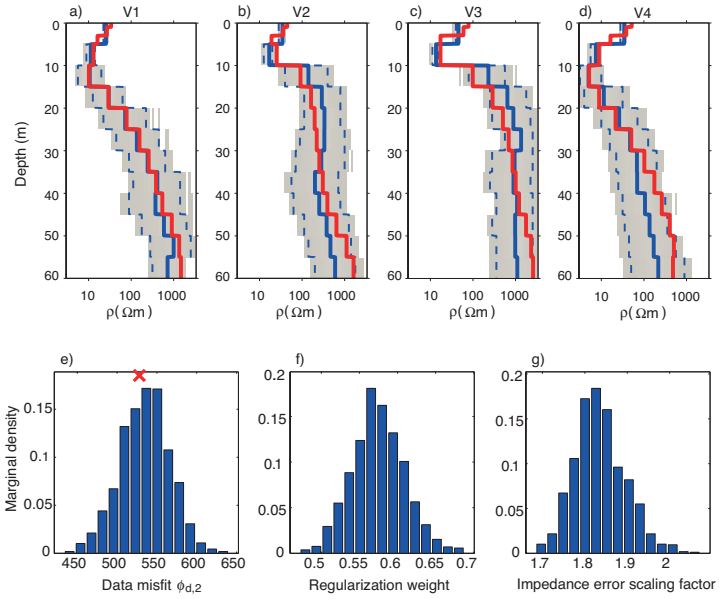

Figure 3.12: MCMC inversion of the Skediga data set with least-squares model constraints. (a-d) Resistivity marginal posterior pdf of the vertical profiles V1, V2, V3 and V4 corresponding to the offsets (a) 50 m, (b) 100 m, (c) 150 m and (d) 200 m of the model shown in Fig. **??**(d). The solid and dashed blue lines represent the mean and P2.5 and P97.5 percentiles, respectively. The red line represents the values obtained with the deterministic inversion (see Fig. **??**a). Grey colour-coding indicates the full posterior pdf range. (e-f) Histograms of the (e) data misfit and (f) impedance error scaling factor marginal posterior pdfs. The red cross at the top of (e) depicts the number of data.

1000Ωm for the crystalline basement (Pedersen *et al.*, 2005). These values are reached at all profiles except in Fig. 3.12(d), probably due to the important clay thickness in the shallow part of the model. Figs 3.12(e) and (f) show marginal distributions of the posterior data misfit and the data error correction factor. These two variables are related. The mean data misfit is 542 and the number of data is comprised within the estimated data misfit uncertainty range. The mean data error correction factor is 1.84, hence data errors are estimated to be almost twice those initially assumed for the impedances. The data misfits presented in Fig. 3.11 are calculated using data errors corrected with this value, and they show that the model given by the deterministic inversion appears to be overfitting the data. This, in turn, could explain the differences in magnitude observed between the two models. An inversion of the Skediga data set with the same priors for the error scaling factor and resistivity values but with no model constraints converged to a similar marginal posterior pdf of the impedance errors (not shown). In accordance with the synthetic example, the posterior pdf of the unconstrained inversion contains models with unrealistically high spatial variability.

3.6 Discussion

We have presented the first fully 2-D pixel-based MCMC inversion of plane-wave EM data. While the presented results indicate that the inversion can be successfully addressed within a probabilistic framework, notable features and issues arise that are discussed in more detail below.

A comparison between the most-squares and MCMC inversions showed that while the former tends to provide slightly larger uncertainty estimates, the results of the two approaches are comparable. A more substantial difference between the methods relates to the centre values from which the uncertainty estimates are derived. This difference is mainly caused by the fact that the most-squares inversion starts from a model that minimizes the combined data and model misfit function, while the MCMC analysis is based on an ensemble mean model obtained from a combination of the marginal estimates of individual variables. The minimization approach used in the most-squares inversion is not rigorously formal, as the best model should be the one that best represents the statistics of the posterior pdf rather than the minimization of the combined data and model misfit function. Calculating maximal and minimal perturbations of specific parameters from this "optimal" model could be the reason for the shifted and slightly larger uncertainty ranges compared to the MCMC estimates that describe the ensemble statistics of the posterior pdf.

The type of model parameterization and the number of parameters have an important impact on the posterior pdfs. Laloy and Vrugt (2012) and Linde and Vrugt (2013) used model parameterizations based on Legendre polynomials and the discrete cosine transform, respectively, to show how improper model truncations may lead to biased model estimates. To alleviate this problem, we considered a finely discretized model. However, the unconstrained inversions converge to models that exhibit much more structure than the true model (see Fig. 3.10a), which is in agreement with Linde and Vrugt (2013). When running inversions with coarser grids (i.e. 10×10 m cells, not shown herein), the proposed models and the true model are in much better agreement and the uncertainty ranges of the parameters were strongly reduced. This highlights the fundamental trade-off between model resolution and variability: allowing a higher spatial resolution by using smaller model cells implies larger resistivity ranges for each pixel.

To obtain meaningful results for fine model discretizations, it appears fundamental to add additional constraints regarding the model structure. As noted by Grandis *et al.* (1999) for the 1-D MT problem, the use of least-squares smoothness constraints reduced the presence of unrealistic oscillations in the models and led to smaller and more realistic estimates of parameter uncertainty. Unfortunately, the models provided by the constrained inversions did not contain all the features of the true model. In regions where the data are not sensitive enough, the

model constraints strongly affect the resulting parameter values and result in biased estimates.

The problem of biased estimates was partly mitigated through joint inversion of the plane-wave EM data with ERT. The inversion of the ERT data alone with l_2 smoothness constraints (not shown) did recover the deep resistor albeit with a smaller magnitude than the true value, but not the deep conductor that was resolved by the RMT data. As seen in Fig. 3.10, when inverting the ERT data and plane-wave EM data separately, constraining the model structure led to oversimplified models, whereas the joint inversion led to the correct amount of model structure for this specific application. The models obtained from the plane-wave EM data could clearly be improved by adding lower frequencies, while a larger electrode spread would improve the ERT models. However, our intention was not to determine an optimal experimental design, but to evaluate the implications of the different constraints applied to the inferred subsurface models. In this sense, we see how the combination of two complimentary methods helps to better estimate the resistivity models in terms of structure and magnitude, and effectively reduces the weight given to the model constraints.

Other strategies can also be applied to tackle the aforementioned issues. The incorporation of a pre-supposed geostatistical model or summary statistics derived from training images can easily be incorporated in the Bayesian framework (e.g. Cordua *et al.*, 2012). Clearly, the resulting models would be much closer to the true model if the true model structure was known and we penalized deviations from this value in Eqs. (3.9) and (3.11), rather than penalizing deviations from zero variability. Reliable information of this kind is often not available and strong assumptions about the model structure will to a certain degree promulgate biased model estimates. Nevertheless, it might be favourable to test the resulting models under such restrictive assumptions, rather than to obtain models that are too variable to be meaningful.

Alternatively, one may consider a set of possible model parameterizations, model discretizations and/or model constraints that may seem equally suitable for a specific problem. In the spirit of Oldenburg and Li (1999), one may test the different hypotheses of the model structure and compare the results. More quantitatively, a 2-D trans-dimensional inversion algorithm could be implemented. The trans-dimenional algorithm would, for a chosen parameterization, estimate the appropriate degree of discretization, while inherently favouring models with fewer parameters (see Bodin and Sambridge, 2009 for a 2-D application to seismic tomography). The implementation of such a method is beyond the scope of the present work. Possibly more interesting than determining appropriate model discretizations would be to determine preferred model parameterizations. In fact, a formal theory based on Bayes factors (e.g. Kass and Raftery, 1995) could be used to evaluate evidence in favour of a null hypothesis (see Khan and Mosegaard, 2002; Khan *et al.*, 2004) for applications of Bayes factors to study the physical properties of the Moon). Bayes factors could be used within a model selection strategy to evaluate the a posteriori probability of different model parameterizations and discretizations.

We leave such a study of Bayesian hypothesis testing for future work.

3.7 Conclusions

We presented the first pixel-based and fully 2-D MCMC inversion of plane-wave EM and ERT data. The results of the inversion include the posterior mean and uncertainty of the model parameter estimates. Numerical findings demonstrated a necessity to add explicit constraints on the model structure to obtain meaningful results. These constraints were designed such that they favour model parsimony, and consequently the posterior ensemble mean was shifted closer to that of its true value. However, model interpretation should be done with some care, acknowledging that models may be biased in regions with insufficient data sensitivity, and uncertainty estimates are determined by the imposed model constraints.

The MCMC inversion not only appropriately converged to the posterior mean model, the posterior realizations adequately estimated the actual data errors, including a regularization weight that favours the appropriate model structure. Joint inversion of the ERT and plane-wave EM data provided the best model estimates. The inversion methodology was applied to real RMT aquifer data from Sweden. The MCMC derived posterior mean model was very similar to that of the model geometry obtained from a deterministic inversion. On top of this, the MT-DREAM$_{(ZS)}$ algorithm also retrieved a correction of the impedance errors, which suggested that the deterministic inversion might have overfitted the experimental data. The differences among the resistivity magnitudes of the two different models may hence be explained by a difference in data fitting. Future work should involve diagnostic criteria and methodologies that help favour model selection. In this regard, Bayes factors may be of particular interest.

3.8 Acknowledgments

We thank Jinsong Chen, Amir Khan, one anonymous reviewer, and the editor Mark Everett for their very helpful comments that improved the quality of the paper. Laust B. Pedersen, from Uppsala University, kindly provided the RMT data from Skediga, Sweden. The source code of the MT-DREAM$_{(ZS)}$ algorithm can be obtained from the last author upon request. This research was supported by the Swiss National Science Foundation under grant 200021-130200.

3.9 Appendix A: 2-D Smoothness Constraints

To obtain smoothly varying model property variations in the 2-D models, we impose zero-mean normal prior distributions with respect to the vertical and horizontal log-resistivity gradients:

$$\begin{cases} c^{y}_{m,2}(\mathbf{m}) = \frac{1}{(2\pi\alpha_y)^{M_y}} \exp\left[-\frac{1}{2\alpha_y^2}\left(\mathbf{m}^{\mathrm{T}}\mathbf{D}_y^{\mathrm{T}}\mathbf{D}_y\mathbf{m}\right)\right], \\ c^{z}_{m,2}(\mathbf{m}) = \frac{1}{(2\pi\alpha_z)^{M_z}} \exp\left[-\frac{1}{2\alpha_z^2}\left(\mathbf{m}^{\mathrm{T}}\mathbf{D}_z^{\mathrm{T}}\mathbf{D}_z\mathbf{m}\right)\right], \end{cases} \tag{3.13}$$

where $\mathbf{D}_y$ and $\mathbf{D}_z$ are the difference operators in the horizontal and vertical directions with rank M_y and M_z, respectively, and α_y and α_z are the standard deviations of the log-resistivity gradients in each direction. Assuming that the two pdfs are uncorrelated, the joint pdf of the horizontal and vertical resistivity gradients is given by multiplication of each pdf (eq. 3.8). When the standard deviations are the same, eq. (3.8) can be expressed as

$$c_{m,2}(\mathbf{m}) = \frac{1}{(2\pi\lambda)^{M_y}} \frac{1}{(2\pi\lambda)^{M_z}} \exp\left[-\frac{1}{2\lambda^2}\left(\mathbf{m}^{\mathrm{T}}\mathbf{D}_y^{\mathrm{T}}\mathbf{D}_y\mathbf{m} + \mathbf{m}^{\mathrm{T}}\mathbf{D}_z^{\mathrm{T}}\mathbf{D}_z\mathbf{m}\right)\right], \tag{3.14}$$

where $\lambda = \alpha_z = \alpha_y$. Taking the logarithm of eq. 3.14 results in

$$\log(c_{m,2}(\mathbf{m})) = -M_y \log(2\pi\lambda^2) - M_z \log(2\pi\lambda^2) - \frac{1}{2\lambda^2}\left(\mathbf{m}^{\mathrm{T}}\mathbf{D}_y^{\mathrm{T}}\mathbf{D}_y\mathbf{m} + \mathbf{m}^{\mathrm{T}}\mathbf{D}_z^{\mathrm{T}}\mathbf{D}_z\mathbf{m}\right), \tag{3.15}$$

or, equivalently

$$\log(c_{m,2}(\mathbf{m})) = -(M_y + M_z) \log(2\pi\lambda^2) - \frac{1}{2\lambda^2}\left(\mathbf{m}^{\mathrm{T}}\mathbf{D}_y^{\mathrm{T}}\mathbf{D}_y\mathbf{m} + \mathbf{m}^{\mathrm{T}}\mathbf{D}_z^{\mathrm{T}}\mathbf{D}_z\mathbf{m}\right). \tag{3.16}$$

3.10 Appendix B: Log-likelihood functions for plane-wave EM data

Equation (3.5) represents the log-likelihood function of a set of normally distributed errors that have zero mean and are uncorrelated. These errors may, however, have different standard deviations. Indeed, RMT data often comprise apparent resistivities and phases. Let the first $N/2$ data points be the apparent resistivities $d_i = \rho_i^{app}, i = 1, ..., N/2$, and the last $N/2$ data points the phases $d_i = \varphi_i, i = N/2 + 1, ..., N$. The data standard deviations can then be expressed as (Fisher and LeQuang, 1981)

$$\sigma_i = \begin{cases} r d_i, & \text{if } i = 1, ..., N/2 \\ r/2, & \text{if } i = N/2 + 1, ..., N \end{cases} \tag{3.17}$$

where r is the standard deviation of the relative error of the apparent resistivities, which is assumed to be the same for all measurements. Using eq. 3.17, the middle term in eq. (3.5) can be expressed as

$$\frac{1}{2}\log\left(\prod_{1\le i\le N}\sigma_i^2\right) = \frac{1}{2}\log\left(\prod_{1\le i\le N/2}(r\rho_i^{app})^2 \prod_{N/2+1\le i\le N}(r/2))^2\right) \tag{3.18}$$

which leads to

$$\frac{1}{2}\log\left(\prod_{1\leq i\leq N}\sigma_i^2\right)=\log\left(\frac{r^N}{2^{N/2}}\prod_{1\leq i\leq N/2}\rho_i^{app}\right). \tag{3.19}$$

Expanding the logarithm and replacing this expression in eq. (3.5) gives

$$l(\mathbf{m}|\mathbf{d})=-\frac{N}{2}\log(2\pi)+\frac{N}{2}\log(2)-N\log(r)-\sum_{1\leq i\leq N/2}\log(\rho_i^{app})-\frac{1}{2}\sum_{1\leq i\leq N}\left(\frac{g_i(\mathbf{m})-d_i}{\sigma_i}\right)^2, \tag{3.20}$$

which is equivalent to

$$l(\mathbf{m}|\mathbf{d})=-\frac{N}{2}\log(\pi)-N\log(r)-\sum_{1\leq i\leq N/2}\log(\rho_i^{app})-\frac{1}{2}\sum_{1\leq i\leq N}\left(\frac{g_i(\mathbf{m})-d_i}{\sigma_i}\right)^2. \tag{3.21}$$

3.11 Appendix C: Log-likelihood functions for ERT data

In the case of ERT, we consider a single type of data. The apparent resistivities are assumed to comprise relative errors. Therefore, we follow the same derivation as in Appendix B, but with standard deviations given by $\sigma_i = rd_i, i = 1, ..., N$. Then, the middle term of eq. (3.5) can be expressed as

$$\frac{1}{2}\log\left(\prod_{1\leq i\leq N}\sigma_i^2\right)=\log\left(r^N\prod_{1\leq i\leq N}\rho_i^{app}\right), \tag{3.22}$$

which leads to a log-likelihood of the form

$$l(\mathbf{m}|\mathbf{d})=-\frac{N}{2}\log(\pi)-N\log(r)-\sum_{1\leq i\leq N}\log(\rho_i^{app})-\frac{1}{2}\sum_{1\leq i\leq N}\left(\frac{g_i(\mathbf{m})-d_i}{\sigma_i}\right)^2. \tag{3.23}$$

Chapter 4

Probabilistic three-dimensional time-lapse inversion of magnetotelluric data: Application to an enhanced geothermal system

Marina Rosas-Carbajal, Niklas Linde, Jared Peacock, Fabio I. Zyserman, Thomas Kalscheuer, and Stephan Thiel

in preparation for *Geophysical Journal International*[1]

[1]M. Rosas-Carbajal, N. Linde, J. Peacock, F. I. Zyserman, T. Kalscheuer, and S. Thiel (2014). Probabilistic three-dimensional time-lapse inversion of magnetotelluric data: Application to an enhanced geothermal system. Submitted to *Geophysical Journal International*.

4.1 Abstract

Surface-based monitoring of mass transfer caused by injections and extractions in deep boreholes is crucial to maximize oil, gas, and geothermal production. Inductive electromagnetic methods, such as magnetotellurics, are appealing for these applications due to their large penetration depths and sensitivity to changes in fluid conductivity and fracture connectivity. In this work, we propose a three-dimensional Markov chain Monte Carlo (MCMC) inversion of time-lapse magnetotelluric data to image mass transfer following a saline fluid injection. The inversion retrieves the posterior probability density function of the resulting plume, and thus directly quantifies uncertainty. To decrease computation times, we base the parameterization on a reduced Legendre moment decomposition of the plume. A synthetic test shows that our methodology is effective when the electrical resistivity structure prior to the injection is well characterized. The center of mass and spread of the plume are well retrieved. We then apply our inversion strategy to an injection experiment in an enhanced geothermal system at Paralana, South Australia, and compare it to a three-dimensional deterministic time-lapse inversion. The latter retrieves conductivity changes that are more shallow than the actual injection interval, whereas the probabilistic inversion retrieves plumes that are located at the correct depths and oriented in a preferential north-south direction. The inversion requires a correction factor in the petrophysical relation to explain the time-lapse data. We suggest that this discrepancy may be partly explained by unaccounted subsurface heterogeneities in the base model from which time-lapse changes are inferred.

4.2 Introduction

Monitoring of subsurface mass transfer is critical to maximize oil, gas, and geothermal production, to improve groundwater remediation and to manage environmental risk. In particular, enhanced geothermal systems, which constitute an attractive and increasingly studied renewable energy source (Muñoz, 2014), require information on the flow paths taken by the injected water in order to subsequently recover it and use it for energy production.

Geophysical methods are suitable to characterize subsurface processes, both because of their non-invasive nature and their capacity to provide spatially extensive data coverage (e.g., Hubbard and Rubin, 2005). Various geophysical techniques have been applied in time-lapse studies that aim at inferring temporal changes in the near subsurface (e.g., LaBrecque and Yang, 2001; Day-Lewis *et al.*, 2002; Ajo-Franklin *et al.*, 2007; Miller *et al.*, 2008; Doetsch *et al.*, 2010; Rosas Carbajal *et al.*, 2012). Tailored inverse formulations that reduce noise and model parameterizations that focus on temporal changes make time-lapse inversions more suitable than simple differencing of models obtained from separate inversions. LaBrecque and Yang (2001) proposed a time-lapse difference inversion, and applied it to three-dimensional electrical resistivity tomography (ERT) data. A similar strategy was applied by Ajo-Franklin *et al.* (2007)

to better resolve subsurface variations related to CO_2 injection with crosshole seismics, and by Doetsch *et al.* (2010) combined with joint inversion of crosshole ERT and ground-penetrating radar (GPR). More recently, Rosas Carbajal *et al.* (2012) applied this type of inversion approach to time-lapse electromagnetic (EM) data, specifically radio (RMT) and audio (AMT) magnetotellurics. Inspired by the work of Falgàs *et al.* (2009), who monitored saltwater intrusion in a coastal aquifer, Rosas Carbajal *et al.* (2012) demonstrated significant improvements in the resulting models by incorporating information about the expected temporal changes and removing systematic errors.

For deeper targets, for example in volcanic and geothermal studies, microseismic and inductive EM methods represent prominent monitoring tools. The former consists in locating natural (e.g., Brenguier *et al.*, 2007, 2008) or induced (e.g., House, 1987) seismic sources associated with fracture openings caused by hydraulic pressure variation. The latter are sensitive to changes in electrical resistivity, which can be related to fluid redistributions and changes in fracture connectivity. Feasibility studies (e.g., Lien and Mannseth, 2008; Orange *et al.*, 2009; Wirianto *et al.*, 2010) that focused on controlled source electromagnetics (CSEM) showed that monitoring is feasible, but complicated by the diffusive character of the EM fields and the depths of investigation. Bedrosian *et al.* (2004) performed one of the first magnetotellurics (MT) studies aimed at monitoring a fluid injection. They conducted two-dimensional inversions to map the subsurface resistivity changes following the injection, but no changes could be detected due to the low signal-to-noise-ratio. Kappler *et al.* (2010) studied MT data variations over a period of 4 years at the San Andreas Fault and showed that no significant EM signal precursors occurred prior to the most significant earthquake event during this period. Aizawa *et al.* (2011) conducted a one-year monitoring study at a volcano in Japan using two MT stations. The data indicate large temporal changes, and the two-dimensional inversion models suggested that the resistivity changes occurred at the sea level. Peacock *et al.* (2012, 2013) presented MT monitoring results of an injection experiment in an enhanced geothermal system at Paralana, Australia. In this experiment, 3100 m^3 of saline water, together with acids, were injected at 3.7 km depth to stimulate the opening of new fractures and enable remote monitoring of the plume. The authors observed changes above the ambient noise in both apparent resistivity and phase at ~50 MT stations, with maximum changes occurring in the north-northeast direction. No attempts were made to invert these data.

The works cited above present deterministic approaches to the inverse problem, where one single subsurface model that explains the data is sought by iterative linearization and regularization, and no formal estimates of model parameter uncertainty are made. An alternative approach is offered by probabilistic inversion (e.g., Mosegaard and Tarantola, 1995; Tarantola, 2005). This approach aims at estimating the posterior probability density function (pdf) of the model parameters, which carries detailed information about parameter uncertainty. To numerically estimate the posterior distributions, Markov chain Monte Carlo (MCMC) simu-

lation methods are often used. These methods are able to (e.g., Sambridge and Mosegaard, 2002, and references therein) (1) correctly treat the non-linear relationships between model and data, (2) successfully converge to the posterior pdf of the model parameters, and thus, (3) adequately characterize parameter uncertainty. Pioneering EM applications of probabilistic inversions were performed by Tarits *et al.* (1994), Grandis *et al.* (1999, 2002), Hou *et al.* (2006), Khan *et al.* (2006), and Chen *et al.* (2007). The computational costs of the algorithms, which require many evaluations of the forward response, have only recently been overcome to explore high dimensional problems: Chen *et al.* (2012) presented a MCMC algorithm to invert two-dimensional MT data based on a fixed number of layers, and Rosas-Carbajal *et al.* (2014) presented the first two-dimensional pixel-based MCMC inversion of plane-wave EM data. Probabilistic inversions have been applied to time-lapse geophysical data (e.g., Ramirez *et al.*, 2005; Laloy *et al.*, 2012; Lochbühler *et al.*, 2014). Of particular interest in this study is the work by Laloy *et al.* (2012), who inverted synthetic crosshole GPR travel time data to characterize a injected water plume in partially-saturated media. The authors proposed a model parameterization based on the Legendre moments of the injected plume. This reduces the number of parameters to estimate, and thus the computation time, and constrains the solutions to those that honor the total volume of water injected.

In this paper, we address the problem of estimating the mass transfer following a deep injection with time-lapse MT data. To do so, we present the first three-dimensional time-lapse deterministic and probabilistic inversions of MT data. We parameterize the probabilistic inversion using a Legendre moment decomposition similar to Laloy *et al.* (2012), but under saturated conditions and for a saline fluid, and provide estimates of the plume's center of mass and spread and their uncertainty. After a numerical test, we focus on the plume resulting from the Paralana injection experiment (Peacock *et al.*, 2012), and compare the MCMC inversion results to those obtained by time-lapse deterministic inversion.

4.3 Methodology

4.3.1 Probabilistic inversion

We use a probabilistic framework to estimate the posterior pdf of a set of model parameters that describe a tracer plume at a given time-lapse t. Let this system be described by a vector of B model parameters, $\mathbf{b}_t = (b_{1,t}, b_{2,t}, ..., b_{B,t})$ and a set of N observations, $\mathbf{d}_t = (d_{1,t}, d_{2,t}, ..., d_{N,t})$, which are related to $\mathbf{b}_t$ via a set of equations,

$$\mathbf{d}_t = g(\mathbf{b}_t) + \mathbf{e}_{\mathrm{r},t} + \mathbf{e}_{\mathrm{sys}}, \tag{4.1}$$

where $g(\mathbf{b}_t)$ is the MT forward response, $\mathbf{e}_{\mathrm{r},t}$ is a random observational error that is varying in time, and $\mathbf{e}_{\mathrm{sys}}$ is a systematic contribution that is present at all times. The latter may include modeling errors, static shifts, errors in sensor calibrations, and/or geometrical errors

(e.g., station positioning). The posterior pdf $p(\mathbf{b}_t|\mathbf{d}_t)$ of the model parameters conditional on the data is found by applying Bayes theorem (e.g., Tarantola and Valette, 1982). In the case of a fixed model parameterization, this results in the following proportionality equality

$$p(\mathbf{b}_t|\mathbf{d}_t) \propto p(\mathbf{b}_t)L(\mathbf{b}_t). \tag{4.2}$$

The prior probability, $p(\mathbf{b}_t)$, represents the information known about the subsurface before collecting the actual data, whereas the likelihood function, $L(\mathbf{b}_t)$, describes the likelihood that a given model is responsible for the observed data. The larger the likelihood, the closer the model response is to the experimental data. Typically, the assumption is made that the errors are uncorrelated and follow a normal distribution with zero mean. Then the log-likelihood function, that is, the logarithm of the likelihood function, is $l(\mathbf{b}_t) \propto -\frac{1}{2}\varphi_{l_2}$, where

$$\varphi_{l_2} = \sum_{i=1}^{N} \left(\frac{g_i(\mathbf{b}_t) - d_{i,t}}{\sigma_{i,t}} \right)^2, \tag{4.3}$$

represents the data misfit, $\sigma_{i,t}$ denotes the standard deviation of the i-th error at time t, and the subscript l_2 indicates the l_2-norm. Under these assumptions, φ_{l_2} is expected to follow a chi-squared distribution with expected value N. A common representation of the data misfit is the root mean square (RMS) misfit:

$$\mathrm{RMS} = \sqrt{\frac{1}{N} \sum_{i=1}^{N} \left(\frac{g_i(\mathbf{b}_t) - d_{i,t}}{\sigma_{i,t}} \right)^2}, \tag{4.4}$$

which takes a value of RMS = 1 when $\varphi_{l_2} = N$.

When the data errors contain significant outliers, it is often better to use an exponential distribution, which is equivalent to using an l_1-norm instead of an l_2-norm in the data misfit (Menke, 1989). The l_1-norm is more robust and often represents a more realistic description of data errors (e.g., Claerbout and Muir, 1973; Egbert and Booker, 1986; Chave and Thomson, 1989; Farquharson and Oldenburg, 1998; Tarantola, 2005). For uncorrelated errors, the corresponding log-likelihood function is proportional to $l(\mathbf{b}_t) \propto -\varphi_{l_1}$, where the data misfit is now defined as

$$\varphi_{l_1} = \sum_{i=1}^{N} \left| \frac{g_i(\mathbf{b}_t) - d_{i,t}}{\sigma_{i,t}} \right|, \tag{4.5}$$

and $\sigma_{i,t}$ represents the mean deviation of the i-th error at time t (e.g., Tarantola, 2005).

To numerically implement the probabilistic inversion, we use the DREAM$_{(\mathrm{ZS})}$ algorithm (Laloy and Vrugt, 2012). This is an adaptive MCMC algorithm (e.g., Roberts and Rosenthal, 2007) which, in order to render the sampling more efficient, runs multiple chains in parallel and implements sampling from an archive of past states. Jumps in each chain are calculated by

computing the difference between one or multiple pairs of chain states, drawn from an external sample of points that summarizes the search history of all the individual chains. A proposed model $\mathbf{b}_{t,new}$ is accepted, in the case of a uniform prior, with probability (e.g., Mosegaard and Tarantola, 1995):

$$P_{\text{accept}} = \min\left\{1, \exp[l(\mathbf{b}_{t,new}) - l(\mathbf{b}_{t,old})]\right\}, \tag{4.6}$$

where $\mathbf{b}_{t,old}$ is the chain's last accepted model. If the proposal is accepted then the chain moves to $\mathbf{b}_{t,new}$, otherwise the chain remains at its old location. After a burn-in period, the sampled model realizations are distributed according to the underlying posterior distribution. To assess convergence, the Gelman-Rubin statistic (Gelman and Rubin, 1992) is periodically computed using the last 50% of the chains' samples. Convergence to a limiting distribution is declared if the Gelman-Rubin statistic is less than 1.2 for all model parameters.

A variation of the DREAM$_{(ZS)}$ algorithm is the so-called MT-DREAM$_{(ZS)}$ algorithm (Laloy and Vrugt, 2012), which has recently been applied to several types of geophysical data such as GPR, RMT and ERT (Laloy *et al.*, 2012; Linde and Vrugt, 2013; Rosas-Carbajal *et al.*, 2014; Lochbühler *et al.*, 2014). This multiple-try sampling procedure, designed for high parameter dimensions (i.e., more than ~30 model parameters), proposes several models per chain and per realization, and thus requires many forward computations running in parallel to be efficient. In the present contribution we use DREAM$_{(ZS)}$ as we estimate at maximum 14 parameters. We run the different chains in parallel, and use parallelized forward solvers.

4.3.2 Time-lapse strategy

Rosas Carbajal *et al.* (2012) used a time-lapse inversion strategy to obtain temporal updates from an initial two-dimensional resistivity model using time-lapse RMT and AMT data. The strategy is based on data differencing (LaBrecque and Yang, 2001) to remove systematic errors (see Eq. 4.1). Although the examples were limited to the audio and radio frequency range, this strategy is directly applicable to other types of geophysical data, in particular MT data.

First, a base resistivity model is obtained by means of a deterministic inversion using the data acquired at a reference time ($t = 0$) before any perturbation is made to the system. The resulting data residuals, $\boldsymbol{\delta}_0 = \mathbf{d}_t - g(\mathbf{b}_0) = \mathbf{e}_{\text{sys}} + \mathbf{e}_{\text{r},0}$, are removed from the data acquired at all subsequent times:

$$\tilde{\mathbf{d}}_t = \mathbf{d}_t - \boldsymbol{\delta}_0 = g(\mathbf{b}_t) + \mathbf{e}_{\text{r,t}} - \mathbf{e}_{\text{r},0}. \tag{4.7}$$

The new data sets $\tilde{\mathbf{d}}_t$ used in the inversion at time-lapse t will be contaminated with less error provided that $\sigma_{sys} > \sqrt{\sigma_{r,0}^2 + \sigma_{r,t}^2}$, where σ_{sys} and σ_r are the standard deviations of the systematic and random errors, respectively.

4.3.3 Tracer plume parameterization

Markov chain Monte Carlo inversion is computationally demanding in high parameter dimensions. To reduce the number of parameters, and to include the total mass of water injected as a fixed constraint on the proposed plume geometries, we use a parsimonious model parameterization proposed by Laloy *et al.* (2012). This parameterization is based on a reduced Legendre moment decomposition of the tracer plume. The Legendre polynomials are orthogonal if defined in a unit square domain, and thus the Legendre moments are uncorrelated with each other (Teague, 1980).

Consider a uniformly discretized three-dimensional distribution of the injected fluid θ_i [m^3/m^3], $i = 1, ..., (nx \times ny \times nz)$, for which x_i, y_i and z_i, are the spatial coordinates and nx, ny, and nz the number of voxels in the x-, y- and z-directions, respectively. The three-dimensional space described by $\boldsymbol{\theta}$ is a sub-region of the three-dimensional resistivity forward model domain and is typically more finely discretized (see Fig. 4.1). A set of coordinates $\boldsymbol{\beta} = (x_{\text{start}}, x_{\text{end}}, y_{\text{start}}, y_{\text{end}}, z_{\text{start}}, z_{\text{end}})$ describes the limits within this sub-region where $\theta_i \neq 0$.

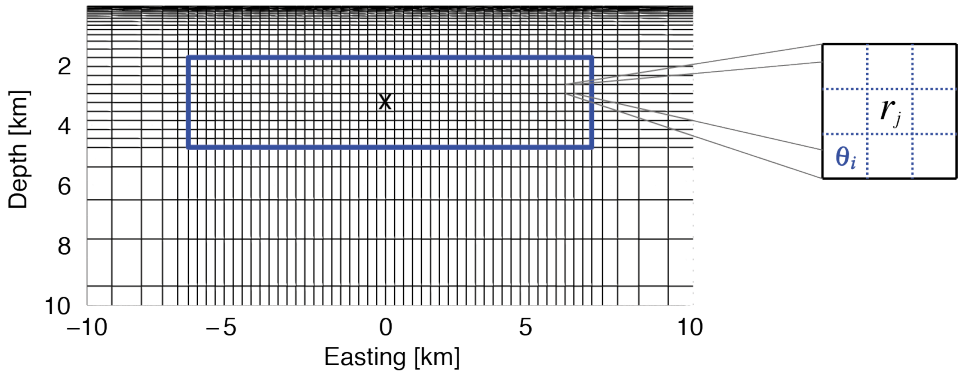

Figure 4.1: Three-dimensional parameter discretization used in the inversions of the Paralana data set. The discretization along the north axis, not shown in the figure, is identical to the discretization along the east axis. The black lines represent the resistivity mesh (the complete extension to the sides and in depth is not shown), which is used as the forward mesh in the MCMC inversions and also as the inversion mesh in the deterministic inversions. The solid blue lines represent the limits of the sub-region where the tracer plumes can be placed in the MCMC inversions. The dashed blue lines represent the discretization of the tracer plume as mapped from the Legendre parameterization. The black cross indicates the injection point.

The Legendre moments $\boldsymbol{\lambda}$ of $\boldsymbol{\theta}$ are given by

$$\lambda_{pqu} = \frac{(2p+1)(2q+1)(2u+1)}{8} \times \sum_{i=1}^{nx \times ny \times nz} P_p(x_i') P_q(y_i') P_u(z_i') \theta_i \Delta x' \Delta y' \Delta z', \tag{4.8}$$

where x', y', and z' are the transformed model coordinates on a unit square grid $[-1 \leq x', y', z' \leq 1]$, $\Delta x'$, $\Delta y'$ and $\Delta z'$ represent the voxel dimensions of the unit square, and $P_p(x_i')$

is the Legendre polynomial of order p evaluated by numerical integration over cell i in the x-direction. In matrix notation, equation (4.8) is described by

$$\boldsymbol{\lambda} = \mathbf{P}\boldsymbol{\theta}, \tag{4.9}$$

where $\mathbf{P}$ contains the Legendre polynomial products on the three-dimensional unit grid. Then, $\boldsymbol{\theta}$ can be reconstructed from its Legendre moments up to a given resolution defined by a truncated series expansion (Teague, 1980),

$$\theta_i^{\text{rec}} = \sum_{p=0}^{O_{max}} \sum_{q=0}^{O_{max}} \sum_{u=0}^{O_{max}} \lambda_{pqu} P_p(x_i') P_q(y_i') P_u(z_i'), \tag{4.10}$$

where the superscript rec stands for reconstructed and O_{max} is the maximum order of moments used for the reconstruction. Writing Eq. 4.10 in matrix notation gives

$$\boldsymbol{\theta}^{\text{rec}} = \boldsymbol{\Gamma}\boldsymbol{\lambda}, \tag{4.11}$$

where $\boldsymbol{\Gamma}$ contains the polynomial product coefficients of the orthogonal moments and has dimension $(nx \times ny \times nz) \times n_{pqu}$, with $n_{pqu} = [(\max(p)+1) \times (\max(q)+1) \times (\max(u)+1)]$. The resulting plumes should not only lead to resistivity models whose forward responses explain the measured data, but they should also honor prior constraints. Here, the first imposed constraint concerns the total mass of injected water, which is directly related to the first Legendre moment:

$$\lambda_{000} = \frac{W^{\text{tot}}}{8} \frac{\Delta x' \Delta y' \Delta z'}{\Delta x \Delta y \Delta z}, \tag{4.12}$$

where Δx, Δy, and Δz represent the true voxel dimensions and W^{tot} is the injected volume of water. The remaining constraints force $\boldsymbol{\theta}$ to be zero at the boundaries of the region defined by $\boldsymbol{\beta}$. Following Laloy *et al.* (2012), we construct a system of equations $\mathbf{A}\boldsymbol{\lambda} = \mathbf{h}$, which contains all the constraints on $\boldsymbol{\lambda}$, and calculate the singular value decomposition (SVD) of $\mathbf{A}$

$$\mathbf{A} = \mathbf{U}\mathbf{S}\mathbf{V}^{\text{T}}, \tag{4.13}$$

where $\mathbf{U}$ and $\mathbf{V}$ are orthogonal matrices that contain basis vectors spanning the space of constraints imposed in $\mathbf{h}$, and basis vectors spanning the model space for $\boldsymbol{\lambda}$, respectively, and $\mathbf{S}$ is a diagonal matrix with the singular values sorted in decreasing order. According to Laloy *et al.* (2012), $\mathbf{S}$ will typically have k significant singular values related to the constraints in $\mathbf{h}$. Then, the solutions to the inverse problem will have the general form

$$\boldsymbol{\lambda} = \mathbf{V}_k \mathbf{S}_k^{-1} \mathbf{U}_k^{\text{T}} \mathbf{h} + \mathbf{V}_0 \boldsymbol{\alpha}, \tag{4.14}$$

where $\mathbf{V}_k$, $\mathbf{S}_k$ and $\mathbf{U}_k$ have dimensions $n_{pqu} \times k, k \times k$ and $N_{prior} \times k$, respectively. The first term on the right side of Eq. 4.14 ensures that $\boldsymbol{\lambda}$ satisfies the desired constraints while the

second term, specifically the vector $\boldsymbol{\alpha}$, is to be determined by the MCMC inversion such that the inferred models honor the data.

The constraints described above do not prevent the generation of models containing negative values (i.e., $\theta_i < 0$). To avoid such models, we only consider the region of the plume with $\theta_i \geq 0$, that is, we set to zero the negative values, and re-scale the plume to conserve the injected water mass.

We evaluate the basic geometrical properties of the resulting plumes in terms of their center of mass:

$$\begin{cases} \mu_{xc} = \frac{1}{W^{\text{tot}}} \sum_{i=1}^{nx \times ny \times nz} \theta_i x_i \Delta x' \Delta y' \Delta z', \\ \mu_{yc} = \frac{1}{W^{\text{tot}}} \sum_{i=1}^{nx \times ny \times nz} \theta_i y_i \Delta x' \Delta y' \Delta z', \\ \mu_{zc} = \frac{1}{W^{\text{tot}}} \sum_{i=1}^{nx \times ny \times nz} \theta_i z_i \Delta x' \Delta y' \Delta z', \end{cases} \tag{4.15}$$

and spread:

$$\begin{cases} S_{xx} = \sqrt{\frac{1}{W^{\text{tot}}} \left(\sum_{i=1}^{nx \times ny \times nz} \theta_i x_i^2 \Delta x' \Delta y' \Delta z' \right) - \mu_{xc}^2}, \\ S_{yy} = \sqrt{\frac{1}{W^{\text{tot}}} \left(\sum_{i=1}^{nx \times ny \times nz} \theta_i y_i^2 \Delta x' \Delta y' \Delta z' \right) - \mu_{yc}^2}, \\ S_{zz} = \sqrt{\frac{1}{W^{\text{tot}}} \left(\sum_{i=1}^{nx \times ny \times nz} \theta_i z_i^2 \Delta x' \Delta y' \Delta z' \right) - \mu_{zc}^2}. \end{cases} \tag{4.16}$$

4.3.4 Petrophysics and upscaling procedure

In this subsection, we explain how $\boldsymbol{\theta}$ can be translated into a salinity distribution and corresponding bulk resistivity values, from which the MT response can be evaluated. Let the three-dimensional subsurface resistivity prior to the injection be described by a vector $r_{j,0}$, $j = 1, ..., (NX \times NY \times NZ)$, with NX, NY and NZ the number of resistivity blocks in the x-, y- and z-direction, respectively. The subscript 0 refers to the base model, that is, prior to the injection. The black mesh in Fig. 4.1 represents this discretization. It is assumed that the region where fluid is injected is saturated with water of constant resistivity. Taking $\Phi_{j,t}$ to be the porosity at the scale of the resistivity discretization, and using Archie's law (Archie, 1942) gives

$$r_{j,0} = \rho_{\text{w}}^{\text{pre}} \Phi_{j,0}^{-m_0}, \tag{4.17}$$

where m_0 is the cementation factor prior to the injection, which is assumed to be known, and $\rho_{\text{w}}^{\text{pre}}$ is the resistivity of the pre-existing fluid at the confined rock temperature. It is assumed that the conductive fluid dominates the conduction in the fracture network (e.g., Brace *et al.*, 1965), and surface conductivity is thus neglected.

The fluid resistivity is a function of temperature and salt concentration. We use the relationship by Sen and Goode (1992) to model this dependence:

$$\rho_{\text{w}}(T, c) = \left[(5.6 + 0.27T - 1.5 \times 10^{-4} T^2) c - \frac{2.36 + 0.099T}{1 + 0.214c} c^{3/2} \right]^{-1} \Omega\text{m}, \tag{4.18}$$

where c is the salt concentration in mol/l and T the temperature in °C. Given a proposed spatial distribution of the tracer plume at time t, $\theta_{i,t}$ [m^3/m^3], which is prescribed at a finer scale than that of the base resistivity model, we consider the possibility of an increase in porosity due to the opening of fractures, $\Delta\phi_{i,t}$, where $\phi_{i,t}$ represents the porosity at the scale of the fine discretization. The bounds for the porosity change are given by $0 \leq \Delta\phi_{i,t} \leq \theta_{i,t}$. To obtain the salt concentration of the fluid at time t in each model block, we sum the contributions from the salt concentration prior to the injection and the salt concentration of the injected water, weighted by the volume they occupy in the available space:

$$c_{i,t} = \frac{\theta_{i,t}}{\phi_{i,t}} c^{\text{inj}} + \frac{\phi_{i,t} - \theta_{i,t}}{\phi_{i,t}} c^{\text{pre}}, \tag{4.19}$$

where $\phi_{i,t} = \phi_{i,0} + \Delta\phi_{i,t}$.

If new fractures are opened it is likely that the cementation factor decreases (e.g., Jougnot and Revil, 2010). As a first approximation, we model the changes of the cementation factor $\Delta m_{i,t}$ as a linear mapping of the injected water content to the interval $[0 : \Delta m^{\max}]$, that is,

$$\Delta m_{i,t} = \frac{\theta_{i,t}}{\theta_{t,\max}} \Delta m^{\max}, \tag{4.20}$$

where the maximum change in the cementation factor $\Delta m^{\max}$ is one of the parameters to be estimated within the inversion. The cementation factor at time t will then be given by $m_{i,t} = m_0 + \Delta m_{i,t}$.

To reduce the time needed to calculate the MT forward responses, it is important to make the resistivity model discretization as coarse as possible. To upscale the finely discretized salt concentration model described by our inverse parameterization to the coarse bulk resistivity model used for forward modeling (see Fig. 4.1), we volume-average the porosity and the cementation factor in each coarse block:

$$\begin{cases} \Phi_{j,t} & = \sum_{i \in V_j} \frac{\phi_{i,t} V_i}{V_j}, \\ M_{j,t} & = \sum_{i \in V_j} \frac{m_{i,t} V_i}{V_j}, \end{cases} \tag{4.21}$$

where V_j and V_i are the volumes of the coarse-mesh and fine-mesh blocks, respectively. Correspondingly, the total salt content in each of the coarse blocks is given by:

$$S_{j,t} = \sum_{i \in V_j} c_{i,t} \phi_{i,t} V_i. \tag{4.22}$$

We use this salt content to calculate the upscaled fluid salt concentration $C_{j,t} = \frac{S_{j,t}}{\Phi_{j,t} V_j}$, which in turn is used in Eq. 4.18 to calculate an upscaled fluid resistivity. Finally, the coarse-mesh bulk resistivity at time t, $r_{j,t}$, is calculated using Eq. 4.17 with the upscaled porosity, cementation

factor and fluid resistivity.

The posterior pdf that we seek to sample with MCMC simulations is given by

$$p(\mathbf{b}_t|\tilde{\mathbf{d}}_t) \propto p(\mathbf{b}_t)L(\mathbf{b}_t), \tag{4.23}$$

where $\mathbf{b}_t = [\boldsymbol{\alpha}, \boldsymbol{\beta}, \Delta m^{\max}]$. Figure 4.2 summarizes our probabilistic inversion methodology and the upscaling procedure.

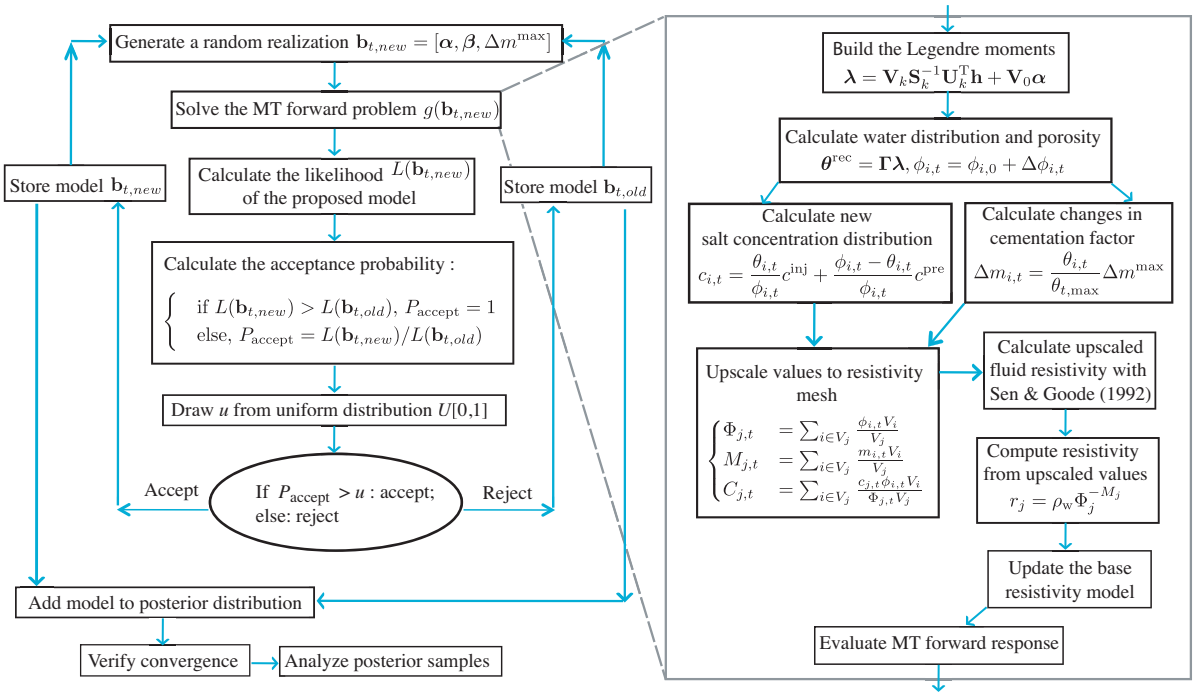

Figure 4.2: Schematic overview of the MCMC inversion framework used to invert the time-lapse MT data. The left side describes the MCMC algorithm applied to one of the parallel chains used in DREAM$_{(ZS)}$. The right side highlights the upscaling procedure used to transform the proposed tracer plume model to a resistivity model that can be used to evaluate the corresponding MT response.

4.3.5 Three-dimensional deterministic inversion

To obtain the base resistivity model needed for the time-lapse inversions, we resort to classical deterministic inversion. To the best of our knowledge, no attempts have been made so far to use MT data to obtain the posterior pdf of a three-dimensional resistivity model discretized in voxels. This is because the large number of unknowns would imply a large number of iterations to converge to the posterior distribution (c.f., Rosas-Carbajal *et al.*, 2014), and the forward solvers still require significant CPU time to calculate the three-dimensional forward model response. We use the ModEM program (Egbert and Kelbert, 2012) with non-linear conjugate gradients as the inversion algorithm (e.g., Nocedal and Wright, 2006) to perform

the deterministic inversions.

4.4 The Paralana test site

The Paralana geothermal system is located in Paralana, South Australia. Its anomalously high heat flow, estimated at 113 mW/m^2 (Neumann *et al.*, 2000), is associated with an unusual concentration of radiogenic elements within the Mount Painter Domain (Brugger *et al.*, 2005). This domain is composed of fractured Paleoproterozoic to Mesoproterozoic gneiss, granites, and metasediments. Well testing and fracture stimulation were carried out in view of developing a power supply from the geothermal sources. In 2009, an injection well was drilled to 4000 m depth and cased to 3725 m. Several zones of over-pressured fluid were encountered between 3670 and 3864 m (Reid *et al.*, 2011) and the measured temperature at the bottom of the borehole was 190 °C. Saline fluids with a resistivity of 1.5 Ωm (at ambient temperature) were encountered at 3860 m, indicating a preexisting fluid-filled fracture network (Peacock *et al.*, 2013).

In July 2011, 3100 m^3 of saline water of resistivity 0.3 Ωm, along with acids, were injected into the metasediments to stimulate the opening of new fractures. The injection was carried out at a depth of 3680 m over the course of four days. During the injection, a microseismic array measured over 11,000 events with the majority located in the northeast quadrant from the injection well (Hasting *et al.*, 2011). The data suggest that fractures opened in a preferred northeast direction and that the total zone stimulated by the injection was approximately 900 m in the northeast-southwest direction, over a depth extent of 600 m. After the injection, the wellhead pressure remained at approximately 27.6 MPa, suggesting that the stimulated volume is connected to a naturally over-pressured zone (Reid *et al.*, 2011) .

Peacock *et al.* (2012) presented the results of the continuous monitoring of the 4-day injection with 11 MT stations placed around the borehole. Peacock *et al.* (2013) reported on time-lapse measurements of about 50 MT stations acquired just before and 1 week after the injection experiment. They observed coherent changes in the MT signals above measurement errors, indicating predominant resistivity changes in the north-northeast direction. In the following section, we use these data in an attempt to infer the spatial distribution of the injected tracer 1 week after the injection was finalized. We refer to Peacock *et al.* (2012) and Peacock *et al.* (2013) for details about the MT transfer function estimation.

4.5 Results

4.5.1 Base resistivity model from three-dimensional deterministic inversion

To evaluate the changes in resistivity produced by the injected water, a base model representing the subsurface resistivity prior to the injection is needed (Rosas Carbajal *et al.*, 2012).

Figure 4.3 depicts the location of the 60 MT stations used to obtain this model. Besides the time-lapse stations (i.e., those repeated post-injection), additional stations were used to obtain the base model.

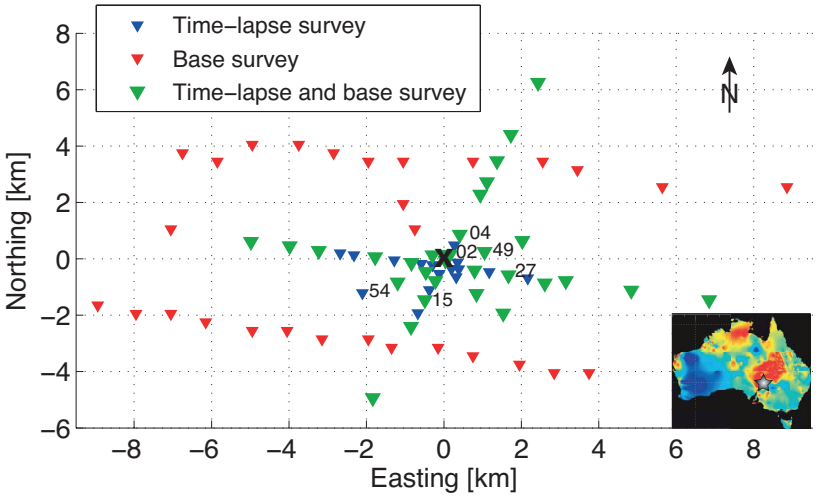

Figure 4.3: Magnetotelluric stations used for the base and time-lapse inversions in Paralana, represented in a local grid with the injection point in the center (×). At the bottom right corner, a map of Australia shows the temperature at 5 km depth where red represents 285 °C and the star locates Paralana.

We first perform one-dimensional MCMC inversions to obtain layered models that are parameterized in terms of the logarithms of resistivity and layer thickness, for 2, 3, 4, and 5 layers. The one-dimensional forward solver is described by Linde and Pedersen (2004b). We use the off-diagonal components of the impedance tensor of 60 stations with 12 periods ranging from 0.016 to 161 seconds and assume an error floor of 5% on the impedance elements. The prior pdf consists of uniform distributions in the range of -2 to 4 for log-resistivity, and 1 to 4 for log-thickness. Figure 4.4(a) shows some posterior realizations of these inversions, and 4.4(b) and (c) display the forward response of the posterior mean models compared to the measured apparent resistivity and phase, respectively. As the number of layers and, thus, the degrees of freedom increase, so does the uncertainty in the posterior pdf. The improvement in data fit from the mean model with 4 layers to the mean model with 5 layers is very subtle (RMS of 6.77 and 6.6, respectively). Furthermore, the inversion considering 5 layers proposes a very thin and conductive layer (located at about 10 km depth), which appears unphysical. The data presented in Figs. 4.4(b) and (c) shows evidence of heterogeneity that cannot be explained with one-dimensional models. Therefore, we use the mean model from the posterior pdf with 4 layers as the starting model of the three-dimensional deterministic inversion. The layers'

thicknesses and resistivities in this model from surface to depth are given by

$$\begin{cases} h_1 & = 33 \text{ m}, r_1 = 70 \ \Omega\text{m}, \\ h_2 & = 700 \text{ m}, r_2 = 4 \ \Omega\text{m}, \\ h_3 & = 7780 \text{ m}, r_3 = 550 \ \Omega\text{m}, \\ h_4 & = \text{half-space}, r_4 = 20 \ \Omega\text{m}. \end{cases} \tag{4.24}$$

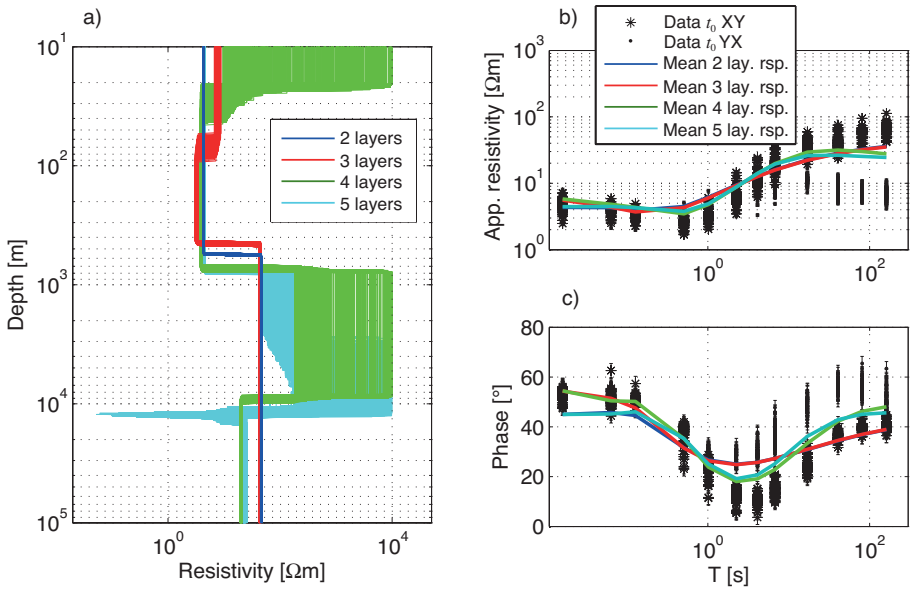

Figure 4.4: (a) Posterior realizations of the one-dimensional MCMC inversions of the base data using different (fixed a-priori) number of layers. Corresponding data in terms of (b) apparent resistivities and (c) phases are shown together with the simulated responses of the posterior mean models, where the X direction corresponds to the north and the Y direction to the east. The model with 4 layers represents a compromise between low data misfit and few model parameters. The forward responses of the one-dimensional models explain the general tendency of the data at low periods but cannot describe the separation between the XY and YX data at higher periods.

We use the ModEM program (Egbert and Kelbert, 2012) to perform the three-dimensional inversion. ModEM implements l_2 measures of model structure and data misfit. This makes it necessary to use Gaussian error assumptions for all the deterministic inversions. Since the diagonal components of the impedance tensor are strongly noise contaminated, we do not use them in any of the inversions. Thus, we invert the same data as in the one-dimensional MCMC inversion, and we obtain a final RMS of 1.35.

Figure 4.5(a) shows vertical slices of the inverted three-dimensional model at the center of the x- and y- axes and for horizontal slices at 700 m and 3700 m (injection) depth. Most of the

new structure with respect to the starting model is present at shallow depths whereas only minor changes are introduced at the injection depth. According to this model, the injection takes place in a thick resistive layer. We present the comparison between the model response and the data for some stations in Fig. 4.5(b). Both apparent resistivity and phase curves are clearly better explained by the three-dimensional model than by the one-dimensional model (see 4.4 Figs. b and c).

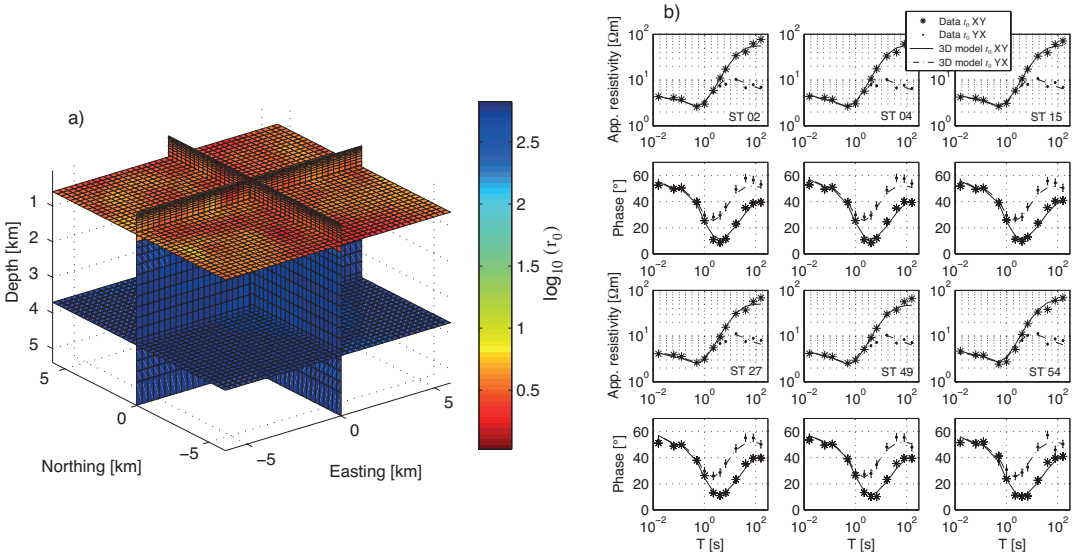

Figure 4.5: (a) Three-dimensional base model at Paralana obtained from the deterministic inversion of the base data using ModEM (Egbert and Kelbert, 2012) and the mean one-dimensional model with 4 layers from Fig. 4.4 as the starting model. Horizontal depth slices correspond to 700 m and 3700 m (injection) depth. (b) Base data and forward response of the model shown in (a) for some of the MT stations.

4.5.2 Time-lapse three-dimensional deterministic inversion

Figure 4.6 illustrates some of the changes observed with respect to the base data one week after the injection (defective stations were removed). Changes in apparent resistivity between stations are more erratic in terms of orientation and magnitude than changes in phase. Hence, we decided to only use the phase data for the deterministic and probabilistic time-lapse inversions.

Following the strategy presented in Section 4.3.2, we compute the data residuals from the base model and remove them from the post-injection data. Not all the stations could be repeated using the same holes for installing the MT stations, however, we applied the time-lapse strategy to all the stations assuming that in cases where the station locations were not exactly the same this would still remove most of the systematic modeling errors. We use the combination ($\sigma_{r,\text{tot}} = \sqrt{\sigma_{r,0}^2 + \sigma_{r,t}^2}$) of the errors pre- and post-injection provided by the impedance transfer function estimations. In addition, we use an error floor of 1° to ensure that data are not

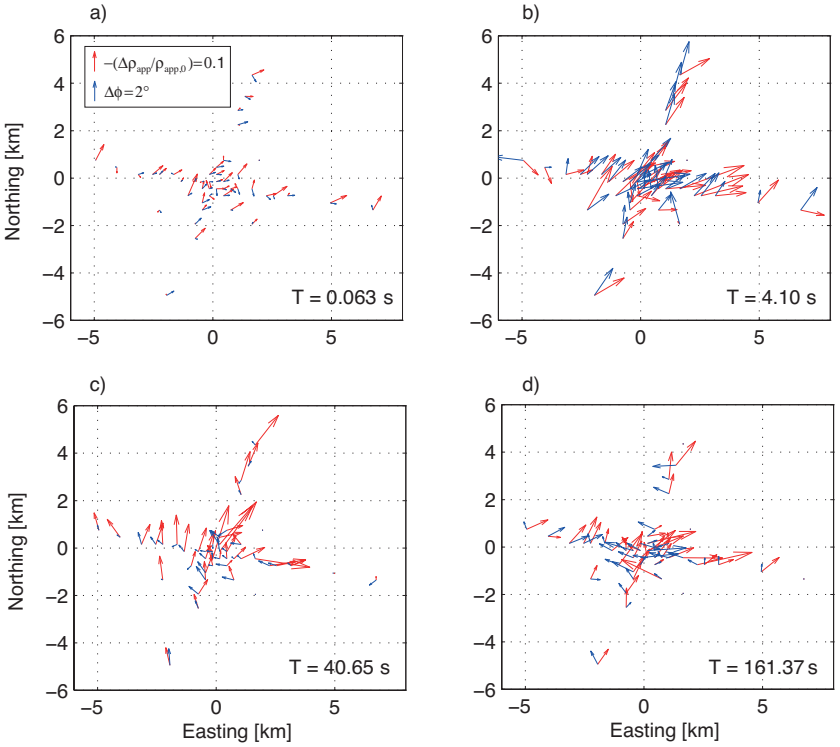

Figure 4.6: Relative apparent resistivity and absolute phase changes observed in the data one week after the injection as a function of station position, for some of the periods considered. Changes are represented by arrows, where the length is proportional to the l_2-norm of the off-diagonal impedance changes and the orientation depicts the relative weight between changes in the XY and YX components. A vertical arrow indicates changes in the XY component only. Phase changes appear to be more consistent among different stations than resistivity changes, and are largest at T = 4.10 s (panel b). This figure is shown as a station-to-station comparison only. For phase tensor representation, see Peacock *et al.* (2013).

over-fitted. Finally, we remove 6 data points corresponding to the longer periods at 3 different stations because they present extremely large errors. This results in a total of 676 data points.

Using the three-dimensional base model (Fig. 4.5a) as the starting model, we perform a deterministic time-lapse inversion of the data. The RMS of the starting model is 2.8 and the final RMS after the inversion converged is 1.01, which corresponds to a misfit of $\varphi_{l_2} = 690$. Depth slices of resistivity changes at 700 and 3700 m depth are presented in Figs. 4.7(a) and (b). Most changes indicate a decrease in the electrical resistivity. In Fig. 4.7(a), large regions with predominant resistivity decrease are found close to the injection point and towards the south and west. Resistivity changes of more than 1 order of magnitude, but with small spatial supports, are obtained below the stations. The resistivity decrease at the injection depth (Fig. 4.7b), is elongated in the north-south direction and is of much smaller magnitude than at 700 m depth (log-resistivity contrasts with respect to the base model are approximately 2 orders of magnitude smaller). The adequate data misfit and the agreement between the data and the

forward responses in Fig. 4.7 (c) suggest that this model explains most of the time-lapse data.

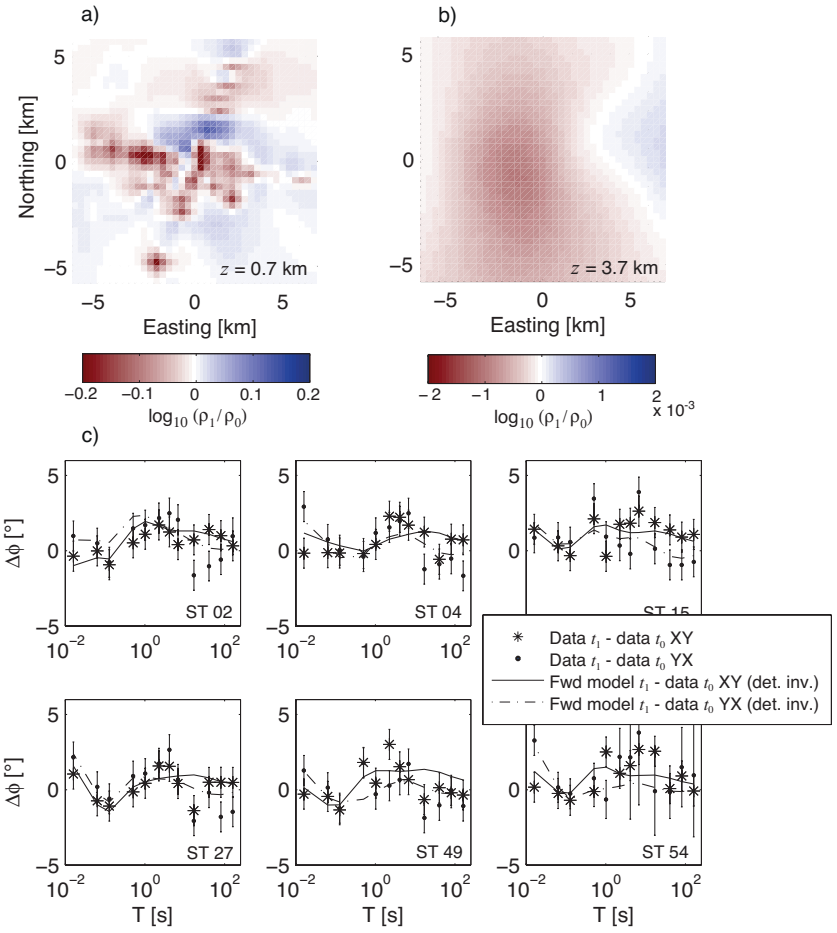

Figure 4.7: (a-b) Estimated differences in log-resistivity after the injection with respect to the base model (Fig. 4.5a), obtained with a three-dimensional deterministic time-lapse inversion of the data acquired post-injection. The depth slices correspond to (a) 700 m and (b) 3700 m (injection depth). (c) Post-injection differences of data and forward response of the model shown in (a) and (b) for some of the stations measured, with respect to the data shown in Fig. 4.5 (b). The resistivity changes are concentrated at shallower depths than the injection point, but the model explains the time-lapse data (RMS = 1.01). Note the low signal-to-noise-ratios in the field example

4.5.3 Synthetic time-lapse MCMC inversion

To evaluate our probabilistic three-dimensional time-lapse inversion strategy, we first consider a synthetic test case. The example is similar to the real experiment in that we assume being in possession of the same amount and type of information in terms of the station distribution, periods and data errors. In addition, we assume that the base model previously obtained (Fig. 4.6 a) is the real one, and insert in this model a three-dimensional plume calculated with a Legendre moment decomposition of order 3. For this, we use the same temperature and salinity constraints as the ones from the real experiment, but we assume that the mass injected is

6 orders of magnitude larger than in the real case, and that the injection is done at a depth of 2700 m, that is, 1 km more shallow than the real experiment. These drastic changes compared to the field experiment were needed to reproduce the observed time-lapse data. Finally, we assign a maximum change in the cementation factor of $\Delta m^{\max} = -0.5$.

To generate the synthetic plume we use the scheme shown on the right side of Fig. 4.2. We consider the porosity presented in Eq. 4.17 to be the crack porosity, that is, the ratio between the volume of open fractures in the rock and the total rock volume. This value is calculated using Eq. 4.17 with the base resistivity model and assuming $m = 2$ over the complete domain. The fluid resistivity at the borehole temperature is calculated using Eq. 4.18 with the values obtained from fluid samples and temperature measured at the injection borehole. Equation 4.17 gives, for an average resistivity value of 550 Ωm at the injection depth, an average crack porosity of 2.5%. We assume that the space created by the rock dissolution and opening of fractures in each voxel is equal to the volume of fluid that originates from the injection in that voxel, that is, $\Delta\phi_{i,t} = \theta_{i,t}$. This assumption implies that the volume of pre-existing fluids does not change since the extra volume needed for the injected fluids is given by the porosity increase. This simplification maximizes the predicted resistivity changes because the pre-existing fluids are not replaced by the injected ones. We adopt the same assumption in the inversion of the field data. Figure 4.8 (a) shows the selected geometry of the synthetic plume represented as the volume of subsurface where salinity has changed. The plume is predominantly oriented in the north-south direction and presents a bend towards the east in the northern extreme. In depth, it extends from ~1.5 km to ~3.3 km. The northeast extreme of the plume has smaller tracer water content than the north-south portion. The center of mass and spread are given in Table 4.1. The spread in the north-south direction is ~900 m larger than in the east-west direction.

Figure 4.8 (b) shows the corresponding resistivity changes with respect to the base model calculated as described in Section 4.3.4 and Fig. 4.2. Maximum resistivity changes of 2 orders of magnitude are found close to the injection point (x= y= 0 in Fig. 4.8b). In the northeastern part, the resistivity changes are ~1 order of magnitude. To simulate the synthetic data, we contaminate the forward response of this new resistivity model with errors following an exponential distribution with a mean deviation (see Eq. 4.5) equal to the standard deviation used for the deterministic inversion. The resulting synthetic data, shown for some stations in Fig. 4.8 (c), have deviations from the base model response that are similar to the field data.

The model parameterization used for the synthetic and field-based inversions is based on a Legendre decomposition up to order 3 (see Section 4.3.3). This means that, besides the 6 coordinate parameters in $\boldsymbol{\beta}$ and the maximum change in the cementation factor $\Delta m^{\max}$, 7 coefficients $\alpha_i, i = 1, .., 7$ need to be determined by the inversion. Following Laloy *et al.* (2012), we assign uniform prior distributions for these coefficients in the range [-0.1 0.1], which contain

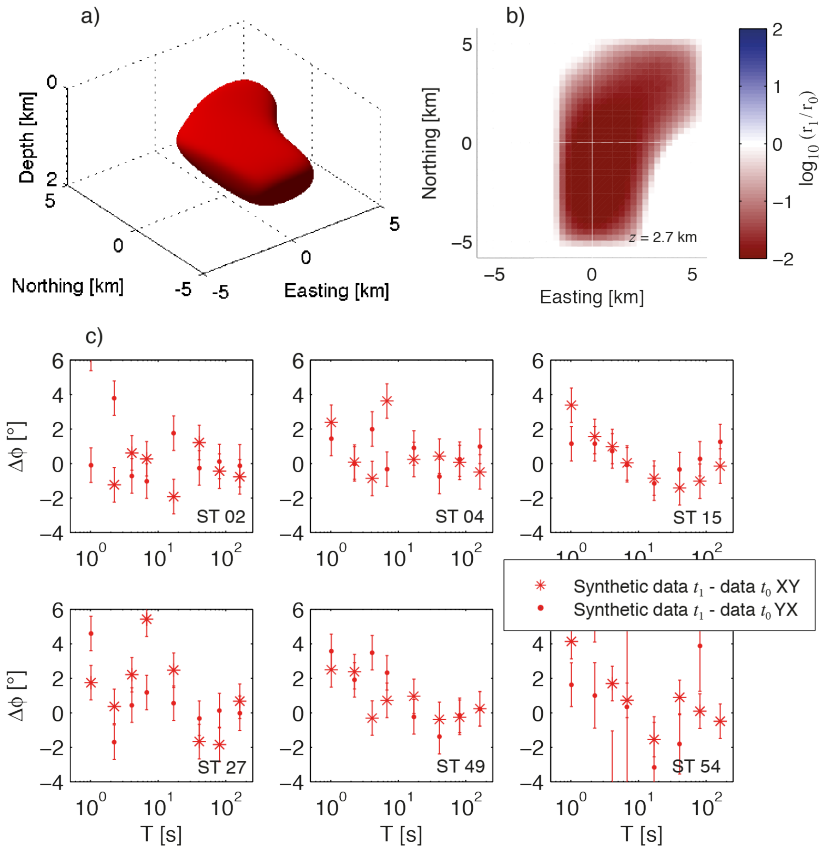

Figure 4.8: Synthetic plume used to test the MCMC inversions based on the Legendre moment decomposition. (a) Plume geometry at the fine discretization used for the Legendre decomposition. (b) Differences in log-resistivity with respect to the base model (Fig. 4 a) at the injection depth of 2700 m. (c) Time-lapse data simulated from the synthetic model and contaminated with noise corresponding to the same errors as assumed for the field data. The plume has a predominant north-south direction with a bend towards the northeast at its northern side.

the values used to create the synthetic plume. For the coordinates of the plume boundaries, we determine a maximum extension of 13.8 km in the east-west and north-south directions and of 3.3 km in depth. Then, we discretize this volume in cubes of $75 \times 75 \times 75$ m^3 to obtain the injected water distribution $\boldsymbol{\theta}$ from the Legendre moments. Thus, x_{start} and y_{start} can take discrete (every 75 m) values between -6.9 km and 0 km; x_{end} and y_{end} can take values between 0 and 6.9 km; and z_{start} and z_{end} can vary between 0.5 and 2.15 km, and 2.15 km and 3.8 km, respectively. To translate the plume to a resistivity model, we discretize the same volume in cubes of $300 \times 300 \times 300$ m^3. This discretization was chosen based on a convergence test of the mesh, in which we evaluated the forward response (also calculated with ModEM) of the base model containing a conductor of the size of the maximum plume allowed for different lengths of the domain and resistivity block sizes. The chosen resistivity discretization represents a compromise between accurate forward responses, that is, changes in impedance of less than 0.1% with respect to a highly discretized and largely extended mesh, and computation time.

Table 4.1: Mean values and standard deviations of the center of mass and spread of the synthetic plume, as estimated with the probabilistic mass-constrained time-lapse approach.

Model	Estimate	Center of mass			Spread			$\Delta m^{\max}$	Misfit
		μ_{xc} [m]	μ_{yc} [m]	μ_{zc} [m]	S_{xx} [m]	S_{yy} [m]	S_{zz} [m]	[-]	[-]
True	N/A	-620	840	2550	2420	1530	440	-0.5	676
Order 3	Mean	-1160	670	2490	2370	1480	370	-0.48	682
	Standard deviation	490	440	310	370	190	110	0.24	3

We allow $\Delta m^{\max}$ to vary between 0, that is, no change in the cementation factor, and -0.99, which implies $m^{\min} \approx 1$ and thus a perfectly connected medium. We use uniform prior distributions for all the model parameters mentioned.

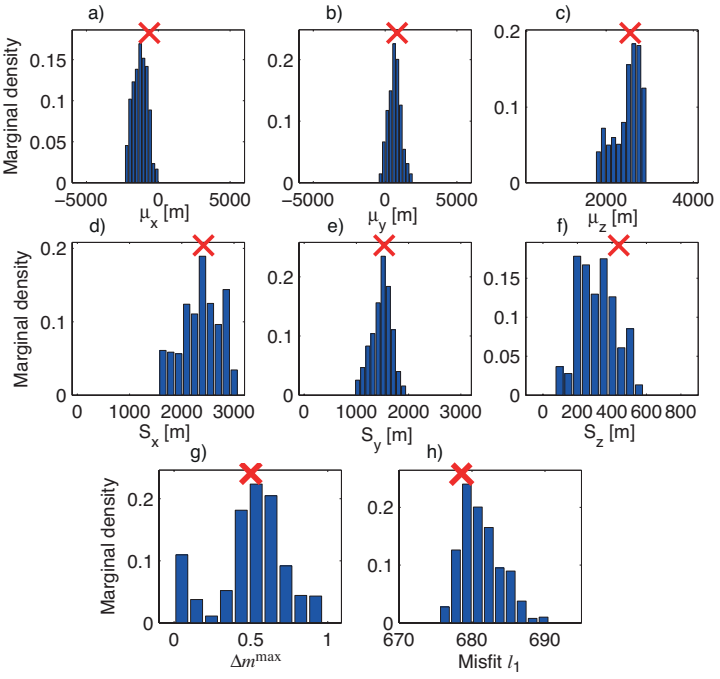

Figure 4.9: (a-f) Marginal posterior distributions of the center of mass (a-c) and spread (d-f) of the plume for the synthetic test. The ranges of values shown correspond prior pdfs' bounds. (g) Maximum change of the cementation factor. (h) Misfit distribution of the posterior models' responses, to compare with the 676 data points used. The red crosses indicate the true values. The histograms' mean and standard deviation are indicated in Table 4.1.

We use the DREAM$_{(ZS)}$ algorithm with 3 chains that evaluate the forward responses in parallel. We also employ the parallelized forward solver in ModEM, which distributes the forward computations for each period and electric and magnetic field configuration to a different processor. To decrease the number of processors needed, we only use the 8 largest periods in the

MCMC inversions, which is where the main time-lapse changes are given. Since we evaluate 8 periods for each configuration, we use 16 processors per chain, and thus 48 processors in total for the forward computations. The computing time of a single forward response depends on the complexity of the model evaluated, but on average takes 11 minutes. Convergence of the chains was reached after ~7500 realizations, which, multiplying by the number of chains implies ~22500 forward computations. The mean acceptance rate was 40% and the total computing time needed to reach convergence was approximately 2 months.

Figure 4.9 (a-f) shows the marginal posterior distributions of the plume's center of mass and spread, and $\Delta m^{\max}$. All the parameter values used to construct the synthetic plume are contained in the posterior pdf. Figure 4.9 (h) shows the data misfit distribution of the models that belong to the posterior pdf. The corresponding model responses have misfits that are close to the true value (676). Table 4.1 shows the mean and standard deviation of the histograms shown in Fig. 4.9. The center of mass estimate in depth is very well determined, being only 60 m more shallow than the true value, while in the x-direction, it is approximately 450 m to the south from the exact value. The standard deviations of the center of mass estimates are in the order of 400 m. The spreads of the plume are well determined, with a larger uncertainty in the x-direction. The cementation factor change is well estimated with a mean value of -0.48 and a standard deviation of 0.24. The posterior misfit distribution is short-tailed and close to the number of data. In Fig. 4.10(a-f) we present some of the plumes that belong to the posterior distribution. Like the true model, the plumes are mostly located in the eastern part of the region and are elongated in the north-south direction. Only two plumes (Fig. 4.10 b and e) present a larger extension to the northeast similar to the true plume.

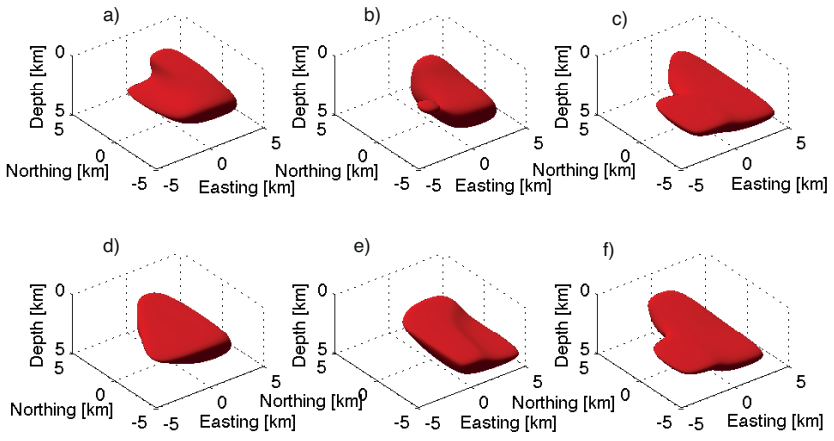

Figure 4.10: (a-f) Random posterior realizations from the MCMC inversion of the synthetic time-lapse data. Models have a predominant north-south direction and similar extension to the true plume (Fig. 4.8a).

4.5.4 Application to the Paralana injection experiment

We now return to the field data acquired during the injection experiment in Paralana. We first perform a MCMC inversion with the same model parameters as for the synthetic case and the same prior distributions, but with the correct water volume. Also, the discretization in cubes of $300 \times 300 \times 300$ m^3 is shifted downwards 1.1 km in z to allow for deeper plumes. Thus, z_{start} and z_{end} can vary between 1.6 km and 3.25 km, and 3.25 km and 4.9 km, respectively.

The base model l_1-norm data misfit of the time-lapse data is $\varphi_{l_1} \approx 1980$ and the MCMC inversion reaches a data misfit that oscillates around $\varphi_{l_1} \approx 750$ for our 676 data (i.e., the data are not fitted). The spread estimates shown in Table 4.2, S_{xx} = 2820 m, S_{yy} = 2900 m, S_{zz} = 710 m, have a tendency to maximize the size of the plume (the prior ranges of $\boldsymbol{\beta}$ result in allowed maximum spreads of 3100 m in the horizontal directions and 740 m in depth). Moreover, $\Delta m^{\max}$, which largely controls the changes in the resistivity with respect to the base model, is very close to the maximum value allowed, that is, -0.99. This behavior of the spread and $\Delta m^{\max}$ indicates that a larger conductance is needed to explain the time-lapse changes.

To investigate if more compact models that fit the data can be obtained, we make a correction in our physical model to account for the additional conductance needed. We add a correction factor in Archies law: $r_{j,t=1} = \frac{1}{10^f} \rho_{\text{inj}} \Phi_{j,t=1}^{-m}$, with f being a free and non-physical parameter to be determined by the MCMC inversion. We use a uniform prior pdf between 0 and 10 for f, and we do not invert for a change in the cementation factor anymore.

Table 4.2: Mean and standard deviation of the estimated center of mass and spread of the injected plume at Paralana, as estimated with the probabilistic mass-constrained time-lapse inversion approach, with and without a correction factor in the petrophysical relationship.

Model	Estimate	Center of mass			Spread					
		μ_{xc} [m]	μ_{yc} [m]	μ_{zc} [m]	S_{xx} [m]	S_{yy} [m]	S_{zz} [m]	$\Delta m^{\max}$	f	Misfit
Order 3 with $\Delta m^{\max}$	Mean	-460	1010	2830	2820	2900	710	-0.95	N/A	750
	Standard deviation	390	1070	110	210	100	60	0.04	N/A	7
Order 3 with f	Mean	-2540	10	3830	2260	1630	530	N/A	5.7	574
	Standard deviation	440	550	130	180	160	60	N/A	0.3	9

The MCMC inversion converged after ~13,500 iterations, with a mean acceptance rate of 25% and 3 months and 1 week of total computation time. Figure 4.11 shows the posterior estimates of mean and standard deviation of the center of mass, spread, correction factor and misfit. The posterior uncertainty ranges of the spreads are no longer affected by the prior boundaries (see Table 4.2). The center of mass of the plume is located towards the south of

the injection point and it is well centered in the east-west direction. In depth, the center of mass is estimated at a depth ~150 m deeper than the actual injection point, with a standard deviation of 130 m. In accordance with the microseismics (Reid *et al.*, 2011), the spread is larger in the north-south direction than in the east-west direction. The posterior pdf of f has a mean value of 5.7 with a standard deviation of 0.7. This results in bulk resistivity changes of approximately 5 orders of magnitude. The posterior models have data misfit values that are smaller than the number of data with the posterior misfit distribution centered on 575.

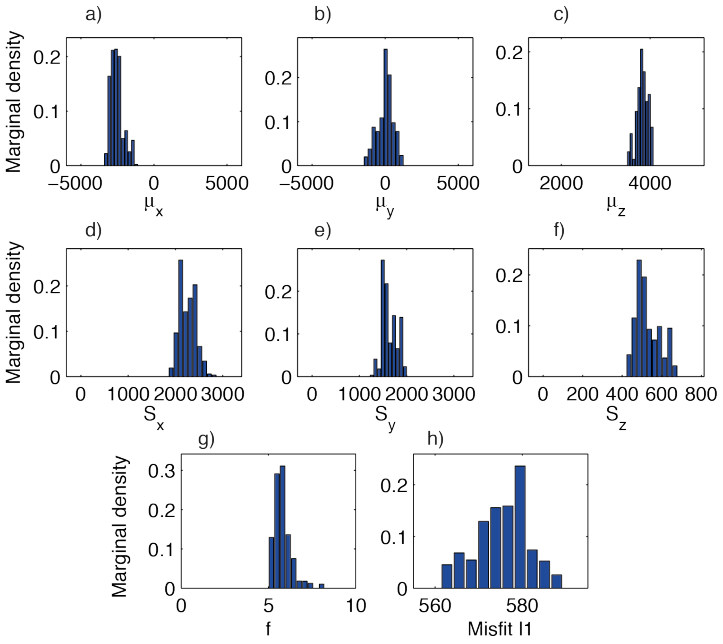

Figure 4.11: (a-f) Marginal posterior distributions of the center of mass (a-c) and spread (d-f) of the plume from the Paralana time-lapse inversion. The range of values shown corresponds to the prior pdfs' bounds. (g) Maximum change of the cementation factor. (h) Misfit distribution of the posterior models, to compare with the 676 data points used. The histograms mean and standard deviation are indicated in Table 4.2.

The posterior models shown in Fig. 4.11(a-f) indicate that the plume is most likely oriented in a north-south direction, and rather to the east. In depth, most models extend between 3400 m and 4500 m but with depth variations along the plume. Some models (Figs. 4.11b, c, d and f) show a plume dipping towards the north, as suggested by the microseismic data by Reid *et al.* (2011). An isolated component of the plume can be observed in Figs. 4.11(b), (d), and (f) in the northeast region at more shallow depths (~3400 m) than the rest of the plume.

4.6 Discussion

Our results indicate that it is possible to infer information about tracer plumes in deep injections experiments using MT data, but also that many important challenges remain.

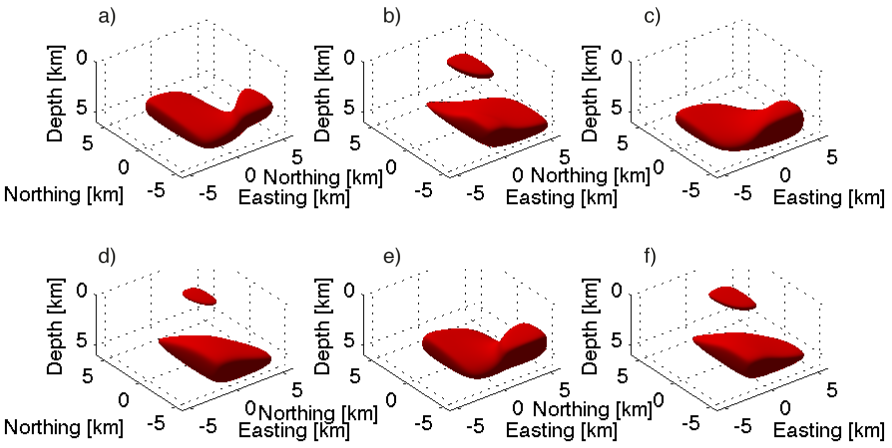

Figure 4.12: (a-f) Random posterior realizations from the MCMC inversion of the Paralana time-lapse data using a correction factor in the petrophysical relationship.

Our probabilistic time-lapse inversion methodology has several advantages over the deterministic approach. The non-linearity of the inverse problem is correctly treated and the uncertainty of the model parameters is formally characterized. Furthermore, valuable prior information such as the injection depth, the fact that electrical resistivity is expected only to decrease or stay unchanged after the injection, and bounds on the region where resistivity can decrease, can be flexibly implemented in the MCMC inversion. The results of the synthetic example shown in Figs. 4.8-4.10 suggest that our approach works properly when the base resistivity model is correct, and the plume is in accordance with the proposed physical model. The MCMC inversion correctly retrieves the change in the cementation factor and the center of mass and spread of the plume. Higher orders of the Legendre moment decomposition could be used, which would allow for more complicated three-dimensional structures (c.f., Laloy *et al.*, 2012). The computational costs would then also be larger (3 months were needed for the inversion of the Paralana data to converge), but it is unlikely that smaller details would be resolved. Given that the first two-dimensional probabilistic inversions of MT data have only recently been presented (Chen *et al.*, 2012; Rosas-Carbajal *et al.*, 2014), this work presents the first advances towards an all-inclusive monitoring strategy with EM methods.

The large time-lapse changes observed in the MT data following the injection experiment in Paralana were used by Peacock *et al.* (2013) to provide qualitative information about the direction of flow of the injected fluids. Our deterministic three-dimensional time-lapse inversion, which was performed without including the corresponding prior information used in the MCMC inversion, was useful to determine the geographical regions of maximum resistivity changes, even if the changes in depth were too shallow. These changes were located close to

the injection point and towards the south and the west of this point. The large number of degrees of freedom allowed the deterministic inversion to place the resistivity changes where sensitivity is largest, that is, at shallower depths. Unphysical resistors also appear (see Fig. 4.7) as no constraints regarding the sign of the resistivity changes were included in the inversion. These results could be improved by including these types of constraints, for example by penalizing positive changes in the resistivity model and using an l_1-norm to penalize the model structure (see examples for two-dimensional inversions in Rosas Carbajal *et al.*, 2012).

A first indication that very large resistivity changes were needed to explain the Paralana time-lapse data was given by the fact that the amount of injected water had to be increased and the depth of injection moved to shallower depths to obtain similar time-lapse changes for the synthetic example. An inversion of the Paralana data that accounted for the amount of water and salinity injected, temperature, and maximum cementation factor changes could not explain the data changes. This suggests limitations of the upscaling model used, and raises the question of whether changes in reservoir properties can be inferred from the time-lapse MT data. In this regard, Vasco *et al.* (2014) argue that instead of aiming at relating changes in geophysical properties to changes in reservoir properties, it may be more viable to relate the initiation of a change in a geophysical property to key reservoir changes such as fluid saturation or pressures. While Vasco *et al.* (2014) consider reservoir monitoring with seismic data, the application to MT data where relatively long time series have to be used to obtain good signal-to-noise ratios of the transfer functions is not straightforward.

When adding a non-physical correction factor in the petrophysical model, the probabilistic inversion could fit the data and retrieved water plumes that are more elongated in the north-south direction. Compared to the microseismics, the center of mass of the plume is located to the south of the injection point, and the plumes predicted from the MT data are much larger in extent (see Fig. 4.12). The latter is expected, as the microseismic data sense the opening of fractures whereas the MT time-lapse data sense changes in electrical resistivity, which happen where the injected fluid is present and not only where fractures open. Also, the microseismic data were measured during the injection, while the time-lapse MT data were acquired one week after the injection was completed.

The extremely large resistivity changes needed to explain the time-lapse data raise important questions about the origin of such a large conductance anomaly caused by the injection. Surface conductivity effects could not explain the changes even if clay minerals were present, since the injection of more conductive water would only decrease its influence. One possibility is that, as the rock dissolves due to the injected acids, more minerals are incorporated into the fluids and thus the salinity of the fluid increases, therefore decreasing the bulk resistivity. An alternative is that the large changes observed originated from a complex arrangement of fractures, which in some directions were effectively connected by the fracture stimulation whereas

in other directions stay in the vicinity of the percolation threshold. Such a hypothesis was suggested by Bahr (2000) to explain the distortion in MT data and by Hautot *et al.* (2002) to associate observed temporal variations in resistivity to pore pressure changes controlled by lake level variations. Reid *et al.* (2011) reported on high fluid pressures encountered when drilling the Paralana borehole and after the injection experiment was finished. This supports the hypothesis that fractures may be well connected in some directions while staying close to the percolation threshold in others, thus creating large variations of the measured electric fields.

Simulating the MT responses of complex fracture networks would be highly computationally demanding. To test the influence of an unaccounted conduction mechanism operating in a preferential direction, we considered the simple case of a base model that contains two large unconnected conductors. To obtain this model, we performed a new deterministic inversion of the base data. The starting model was the same one-dimensional model as the one used in Section 4.5.1, but with two unconnected conductors oriented in the north-south direction that are separated by ~2 km and are located on opposite sides of the injection point. They have a vertical extension of ~5 km, and are completely embedded in the layer of 550 Ωm. The deterministic inversion based on this new starting model provided a new base model very similar to the original one (Fig. 4.5a), except for the two conductors. The RMS is 1.21, that is, slightly lower than the original one (RMS = 1.35). We then took one of the posterior plume realizations (Fig. 4.13a) from the MCMC inversion performed with the original base model. The plume, which fits the time-lapse data when evaluated with the original base model, has $f = 5.9$. When evaluated with the new base model, the plume effectively connects the two conductors and predicts larger data changes than the ones observed, which results in a large misfit of $\varphi_{l_1} = 1336$. This indicates that the base model has a significant influence on the inferred plume statistics. We then used the new base model to initiate a new MCMC time-lapse inversion until acceptable data misfits were reached. Figure 4.13(b) shows one of the plumes that fit the data ($\varphi_{l_1} = 636$). This plume is much smaller than the one shown in Fig. 4.13(a) and has $f = 4.4$, that is, smaller than any f contained in the posterior pdf displayed in Fig. 4.11(g).

This simple analysis suggests that, to a certain extent, the large resistivity changes needed to explain the time-lapse data could be an effect of our chosen base model. Indeed, the synthetic example, which was performed using the correct base model, yielded good estimates of the plume. This effect could be studied by performing a time-lapse MCMC inversion where not only the plume geometry would be inverted for, but also the heterogeneous base model. Such methods have been proposed for deterministic time-lapse studies involving ERT data (Kim *et al.*, 2009; Karaoulis *et al.*, 2011). This type of study would be highly computationally demanding, and we leave it for future investigations.

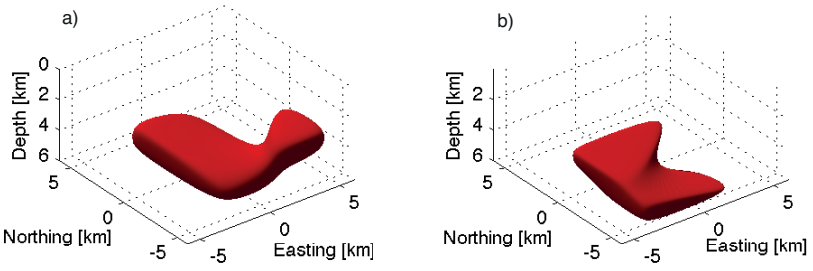

Figure 4.13: Influence of the base model on the plume estimation. (a) Plume belonging to the posterior distribution of the MCMC inversion with the base model represented in Fig. 4.5(a) including a correction factor (f = 5.9). (b) New proposed plume, more compact and with a smaller correction factor (f = 4.4) which fits the time-lapse data when using a different base model.

4.7 Conclusions

We presented the first time-lapse three-dimensional deterministic and probabilistic inversions of EM data, with focus on imaging a tracer plume created by injecting a saline tracer in a geothermal system. The time-lapse deterministic inversion resulted in resistivity changes that are much more shallow compared to the depth of the injection, which demonstrates the importance of including prior information such as the injection point and the fact that the electrical resistivity is expected to decrease following the injection. The probabilistic approach used was based on petrophysical relations and a reduced Legendre moment decomposition of the injected plume that was chosen to decrease the parameter dimensionality and thus the computation times. This approach was shown to be effective when applied to a synthetic test case based on similar informations as those available for the real experiment. For the inversion of the Paralana data, a large correction factor had to be included in the petrophysical relation to account for the extra conductance needed to explain the time-lapse changes. The plumes belonging to the posterior pdf are elongated in the north-south direction, which is in agreement with microseismic data. However, their center of mass is estimated to be located south from the injection point, which is in contrast to the microseismic events. The large correction factor values found suggested important limitations in our physical model. Since the studied media is highly fractured, a possible explanation is the existence of a connected fracture network that is close to the percolation threshold in one direction. Another related possibility is a heterogeneous base resistivity distribution that is poorly represented by our base model. A simple modeling example indicated that this is indeed a potential explanation. Thus, more efforts have to be put in the accurate characterization of the base model when performing monitoring studies with EM methods.

4.8 Acknowledgments

We thank Eric Laloy for his advice on the use of the Legendre moment parameterization, Philippe Logean for his help with the cluster implementations, Damien Jougnot for useful discussions about petrophysics, Anna Kelbert and Gary Egbert for providing the ModEM program for the deterministic inversions and forward computations, and Jasper Vrugt for providing the DREAM$_{(ZS)}$ program. This work was supported by the Swiss National Science Foundation under grants 200021-130200 and 200020-149117.

Chapter 5

Conclusions and Outlook

The general objective of this thesis was to improve the inversion results of plane-wave electromagnetic (EM) data related to static and dynamic subsurface studies. The research performed builds on an extensive number of synthetic feasibility studies and a few field experiments that show the potential of plane-wave EM methods to image and monitor the Earth's subsurface. The main contributions are related to a set of increasingly refined inversion strategies that provide new insights into the capability of plane-wave EM methods to resolve target features and temporal changes in the subsurface. Key advancements are related to the MCMC probabilistic framework used to perform the inversions, the incorporation of relevant prior information in the inversion algorithms, and the time-lapse strategies applied for dynamic characterizations. The main conclusions of the thesis are presented in this chapter, followed by an overview of persisting challenges related to my work that could help to further advance the inversion results of plane-wave EM methods if solved.

5.0.1 Conclusions

To decrease the non-unicity of the inverse problem and obtain models in accordance with expected subsurface temporal changes, I first implemented a time-lapse differencing strategy and enforced specific information in a deterministic two-dimensional inversion algorithm, as presented in Chapter 2. The time-lapse strategy had previously been proven useful for other geophysical methods and this was found to be the case for plane-wave EM methods as well. The numerical studies showed that the larger data errors present when this technique is not used lead to overly-smoothed models and thus poorly resolved temporal changes. Conversely, removing the systematic errors provides better defined structures and less weight is given to the model regularization term. The prior information considered in Chapter 2 includes the use of a stochastic regularization operator to specify the statistical properties of the expected changes, the use of non-l_2 norms to penalize structure and thus obtain sharper spatial transitions between regions where changes occur and where they do not, and the incorporation of expected ranges of conductivity changes through Lagrange multipliers. The stochastic regularization adds flexibility to the regularization since it allows to specify the expected correlation

lengths in the vertical and horizontal directions. The examination of different model norms led to the conclusion that the perturbed l_1-norm is probably the best option for monitoring applications since it produces sharp delimitations of the temporal changes but also respects smooth variations when this is motivated by the data. The time-lapse models were shown to further improve when incorporating constraints regarding the expected ranges of resistivity changes (resistivity could only decrease or remain unchanged in the example presented in Chapter 2).

Despite this positive results, much room for improvement was left considering that the deterministic framework only retrieves one possible model among the many that could equally explain the data and satisfy the imposed constraints. This is why I then decided to adopt a Bayesian framework and perform probabilistic inversion of plane-wave EM data using a Markov chain Monte Carlo (MCMC) algorithm. In Chapter 3, I presented the results of a pixel-based two-dimensional MCMC inversion of plane-wave EM data and electrical resistivity tomography (ERT) data. This algorithm provides formal estimates of the model parameters' uncertainty, and thus allows to completely evaluate the non-unicity of the inverse problem given the prior information. The random exploration of the posterior pdf with MCMC simulations becomes increasingly inefficient for large model parameter dimensions. When no information regarding the model structure is included, the posterior models tend to present unrealistically large spatial variations. In Chapter 3, I dealt with this problem by applying model regularizations as it is usually done in deterministic inversions. The model structure penalization is more straightforward to implement in a MCMC inversion algorithm than in a deterministic one. For example, applying an l_1-norm to penalize the model structure requires no approximation (see the Ekblom norm or perturbed l_1-norm in Chapter 2) because no linearization is needed in MCMC inversion. The regularization applied led to more realistic models and a significant decrease in the number of realizations needed to reach convergence. However, in regions were the data was not sensitive enough to constrain the model, the regularization led to biased estimates that did not contain the true model parameter value. In this regard, the joint inversion of RMT and ERT data resulted in a better constrained model and a reduced weight given to the regularization and estimates' bias.

In Chapter 3, I also compared the uncertainty estimates provided by MCMC inversion and (deterministic) most squares inversion. The results in terms of deviations from the mean model are in agreement but the central values of the uncertainty ranges are not the same, which means that the most squares inversion results may be slightly biased. This problem arises from the fact that the most squares inversion starts from a model that minimizes the objective function, and thus represents the maximum likelihood but, in the general case, not the expected value (i.e., the mean). The most squares inversion is often unsuitable for estimating the uncertainty of all the model parameters since in practice a different and careful inversion needs to be performed for each model cell that is studied.

After treating time-lapse deterministic inversions in Chapter 2, and probabilistic inversions in Chapter 3, I addressed the challenging problem of estimating the three-dimensional spatial distribution of an injected saline water plume in a probabilistic framework (Chapter 4). I applied a time-lapse strategy similar to the one used in Chapter 2 to improve the quality of the time-lapse models. For a fixed number of model parameters, the computational burden of MCMC inversion is significantly increased in three-dimensions due to the time needed to calculate the three-dimensional forward responses. To reduce the computation times, I inverted only for the injected plume's spatial distribution and used the base resistivity model obtained prior to the injection to update the resistivity only in the region where the plumes were proposed. Furthermore, I parameterized the injected water distribution in terms of a reduced Legendre moment decomposition to decrease the number of model parameters to be estimated. The results presented in Chapter 4 show that the approach works well when the base model is correctly characterized. For the real injection experiment, extremely large conductivity changes are needed to explain the time-lapse data. An improper characterization of the base conductivity model could be the reason for the need of such large changes, thus indicating that more efforts should be placed in the characterization of the base model.

The works presented in Chapters 2, 3 and 4 give clear evidence of the importance of including as much prior information as possible in the inversion algorithms to obtain improved subsurface models. In Chapters 3 and 4, which present probabilistic approaches, the prior information was much easier to include. The probabilistic framework offers also more flexibility to implement other types of error distributions such as the exponential distribution, which assimilates the presence of outliers in the data better than the traditional Gaussian distribution. Finally, as demonstrated in Chapter 3, probabilistic inversion also allows to invert for hyper-parameters such as the regularization weight and the standard deviation of the errors. This is very helpful in practice, since usually the errors are assumed to be known and statements of over- or under-fitting the data rely only on the RMS of a fixed error. The application of this methodology to field data showed that previously found models obtained with deterministic inversions were based on an overly-small standard deviation of the errors, which resulted in inversion artifacts. The downside of MCMC inversion related to the computation time needed to reach convergence was partially ameliorated in Chapter 3 by applying model regularizations and in Chapter 4 by proposing a model reduction based on the Legendre moment decomposition of the injected water plume. Both of these methods effectively reduced the number of iterations needed for the MCMC algorithm to converge. Whether a model reduction or model regularization strategy is used, the posterior pdf is affected by these choices and interpretation of the uncertainty estimates should be done acknowledging this influence.

5.0.2 Outlook

Probabilistic inversion performed with MCMC methods is becoming increasingly popular thanks to its ability to correctly treat non-linear inverse problems and quantify model param-

eter uncertainty. The main drawback of this technique is the difficulty to effectively sample the complete space of posterior models, especially when dealing with high parameter dimensions. This, combined with the computationally expensive forward solvers often needed to correctly simulate the physics, make MCMC simulations computationally expensive. Thus, efforts should be put in the search for better performing algorithms to explore the ever increasing parameter dimensionality. In this regard, the use of adaptive MCMC algorithms (Roberts and Rosenthal, 2007; Vrugt *et al.*, 2009; Laloy and Vrugt, 2012) and multiple-try (Liu *et al.*, 2000; Laloy and Vrugt, 2012) techniques as applied in this thesis proved useful for exploring high-parameter dimensions and constitute promising strategies that may become mainstream for geophysical inversions.

The computational resources and mathematical algorithms used for forward computations constantly outperform themselves. However, before forward solvers become efficient enough to routinely compute high-dimensional MCMC inversions, other solutions may be applied to decrease the time needed to compute the forward responses. One possibility would be the use of approximate forward solvers, combined with precise solutions when necessary, in the MCMC algorithm. Many approximations exist for plane-wave EM methods (e.g. Habashy *et al.*, 1993; Virieux *et al.*, 1994; Zhdanov and Fang, 1996; Zhdanov and Hursan, 2000), which could be used in a two-stage MCMC inversion (Christen and Fox, 2005; Efendiev *et al.*, 2005) where the precise forward response is used only if the approximate solution suggests that the proposed model should be accepted. The requirement for this method to converge to the correct posterior is that the likelihood function calculated with the approximate solution represents a smoothed version of the true likelihood calculated with the precise solution. For time-lapse problems, a direct reduction of the response computation times could be achieved by using integral equations, which only need the anomalous component (i.e. the temporal changes) to be discretized. This approach can be applied even in the case of heterogeneous background models (Zhdanov *et al.*, 2006).

As shown in Chapter 4, model reduction techniques decrease the computation times because of the smaller number of model parameters to estimate. They also imply smaller uncertainties of the model parameters due to the variance-resolution trade-off. In the case of time-lapse inversion of an injected water plume, the reduction was done by inverting for the water plume geometry parameterized in terms of a Legendre moment decomposition. For static three-dimensional characterizations, a reduced parameterization that reproduces the expected variations in the subsurface at different scales may not be easy to find. Parameterizations based on orthogonal basis such as the discrete cosine transform (e.g. Linde and Vrugt, 2013) are a possible way to decrease the number of coefficients to invert and may be a first option to tackle three-dimensional inversion of plane-wave EM data.

The inclusion of more refined prior information could also help to further decrease computa-

tion times and model uncertainty. The flexibility offered by MCMC inversion to include prior information is sometimes criticized because this information can be tuned so that the posterior models have some desired properties (Scales and Sneider, 1997). Note that, in the strict sense of Bayes theorem, prior information should only refer to actual information provided independently of the recorded data. Thus, model regularization, as a means to reduce the unrealistic spatial oscillations in model parameter values when there is few data available or an over-parameterized model such as in Chapter 3, could not be considered prior information and should not be implemented as such in Bayesian inversions. In practice, as it was shown in Chapter 3, not including this information may lead to unrealistic models that are very difficult to interpret. Possible improvements regarding the prior information used in MCMC inversion of plane-wave EM data include the use of model structure penalization with respect to a certain pre-conceived model or measure of structure, if such information is available. The incorporation of information from training images was shown to improve the results of the inversion in near-surface studies, for example by generating samples of the prior pdf by sequentially simulating the models according to the image's statistics (e.g. Cordua *et al.*, 2012) or by penalizing deviations from their summary statistics (Lochbüler *et al.*, submitted). Stochastic regularization, as used in the time-lapse deterministic inversion in Chapter 2 could also be implemented.

While the aforementioned possibilities would certainly improve the inversion results, the availability of those types of information is unfortunately not always granted and their use may lead to biased estimates. Complimentary methods such as ERT and RMT, as shown in Chapter 3, help to better constrain the models and should be implemented when possible. Joint inversion of geophysical methods that are sensitive to different physical parameters, such as plane-wave EM methods and seismics, are of primary importance to better characterize the subsurface. The probabilistic framework could help to implement better couplings between the different models. For example, when applying cross-gradient penalizations (Gallardo and Meju, 2004), different norms could be used and the same penalization could be switched off in some regions. Integrated inversions that constrain the subsurface models not only through joint inversion of different geophysical methods but also by incorporating geochemical and petrological data (e.g. Afonso *et al.*, 2013a,b) are starting to be developed. They may be used to directly infer thermal state, water content or even chemical composition in the subsurface. While it is highly important to integrate these different kinds of information to obtain more consistent models, it is also important to further advance in the study of how to link the geophysical parameters with the parameters of interest, that is, the petrophysical relations and the upscaling and downscaling laws. Laboratory experiments constitute a key tool to further advance in these fields.

The different choices of prior information, likelihood function and/or model parameterization and degree of discretization affect the uncertainty estimates. This points to the need for formal

tools that compare and ultimately decide which of those conceptually different possibilities is the most suitable. In this regard, model selection strategies hold a promising potential to use the collected data to falsify or favor certain types of conceptual models over others by comparing their evidence (see Eq. 3.2). A particular type of model selection is the trans-dimensional inversion (Malinverno, 2002) where, given a fixed model parameterization and prior pdf, the degree of discretization is determined within the probabilistic inversion. The trans-dimensional inversion inherently favors models with fewer parameters for equal data fitting, thus a model regularization term is not necessary. This methodology has been applied in one-dimensional inversions of EM (Minsley, 2011) and controlled source EM (Ray and Key, 2012) data. However, two- and three-dimensional inversions seem less straightforward to implement (see Bodin and Sambridge, 2009 for a two-dimensional application to seismic tomography). A more radical model selection is done when comparing not only different degrees of discretization but also different types of model parameterization or prior information (e.g. model regularization). For this purpose, Bayes factors (Kass and Raftery, 1995) can be computed, which are ratios of the "competing" conceptual models' evidences. Bayes factors have been rarely used for hypothesis testing with geophysical data (c.f. Khan and Mosegaard, 2002; Khan *et al.*, 2004; Linde, 2014). More studies should be encouraged in this direction.

Usually, the data used for plane-wave EM inversion are apparent resistivity and phases of the impedance tensor components. These are not the raw data measured in the field but are derived from the measured electric and magnetic time series. Thus, the systematic and random error separation proposed for time-lapse inversion referring to calibration errors, geometrical errors and anything related to the acquisition process should ideally be applied to the raw data. However, the modeling errors coming from the imperfect model discretization, unaccounted anisotropy, or incorrect station positioning in the mesh, should be taken into account with the processed data. This shows that there is still a potential for improvement in time-lapse studies related to the removal of errors prior to the transfer function estimation. Since the EM sources are different for different plane-wave EM methods, the transfer function estimation is also different and the characterization of error propagation of the electric and magnetic fields to apparent resistivity and phase should be also method-dependent.

Improvements in the inversion results with respect to the injection experiment presented in Chapter 4 could be achieved by placing more stations in a grid-based distribution to increase the spatial constraining of the plume. The use of the tipper pointer could also be helpful to better delineate the conductive plume. Given the volumetric nature of the plane-wave EM methods sensitivity to electrical resistivity, it will still remain very difficult to retrieve precise spatial distributions of this property without incorporating further information. Instead of over-interpreting highly discretized models carrying large uncertainties, reduced models are promising strategies to retrieve simple reliable estimates of temporal changes. Future efforts should be put in finding a proper trade-off between model simplicity and data fit, while avoiding

biased estimates. The aforementioned theory of Bayes factors could be of help for this kind of studies.

Bibliography

Afonso, J., Fullea, J., Yang, Y., Connolly, J., and Jones, A. (2013a). 3-D multi-observable probabilistic inversion for the compositional and thermal structure of the lithosphere and upper mantle. II: General methodology and resolution analysis. *Journal of Geophysical Research*, **118**(4), 1650–1676.

Afonso, J., Fullea, J., Griffin, W., Yang, Y., Jones, A., D Connolly, J., and O'Reilly, S. (2013b). 3-D multiobservable probabilistic inversion for the compositional and thermal structure of the lithosphere and upper mantle. I: a priori petrological information and geophysical observables. *Journal of Geophysical Research*, **118**(5), 2586–2617.

Aizawa, K., Ogawa, Y., and Ishido, T. (2009). Groundwater flow and hydrothermal systems within volcanic edifices: Delineation by electric self-potential and magnetotellurics. *Journal of Geophysical Research: Solid Earth (1978–2012)*, **114**(B1).

Aizawa, K., Kanda, W., Ogawa, Y., Iguchi, M., Yokoo, A., Yakiwara, H., and Sugano, T. (2011). Temporal changes in electrical resistivity at Sakurajima volcano from continuous magnetotelluric observations. *Journal of Volcanology and Geothermal Research*, **199**(1), 165–175.

Ajo-Franklin, J. B., Minsley, B. J., and Daley, T. M. (2007). Applying compactness constraints to differential traveltime tomography. *Geophysics*, **72**(4), R67–R75.

Alumbaugh, D. L. and Newman, G. A. (2000). Image appraisal for 2-D and 3-D electromagnetic inversion. *Geophysics*, **65**(5), 1455–1467.

Archie, G. (1942). The electrical resistivity log as an aid in determining some reservoir characteristic. *Transaction of the American Institute of Mining and Metallurgical engineers*, **146**, 54–62.

Avdeev, D. (2007). *3D EM Forward Modeling Using Integral Equations*. Amsterdam: Elsevier.

Avdeev, D. B. (2005). Three-dimensional electromagnetic modelling and inversion from theory to application. *Surveys in Geophysics*, **26**(6), 767–799.

Backus, G. and Gilbert, F. (1970). Uniqueness in the inversion of inaccurate gross earth data. *Philosophical Transactions for the Royal Society of London. Series A, Mathematical and Physical Sciences*, pages 123–192.

Bahr, K. (2000). Percolation in the crust derived from distortion of electric fields. *Geophysical research letters*, **27**(7), 1049–1052.

Bastani, M. (2001). *EnviroMT: A new controlled source/radio magnetotoelluric system*. Ph.D. thesis.

Bedrosian, P. A., Weckmann, U., Ritter, O., Hammer, C. U., Hübert, J., and A., J. (2004). *Electromagnetic monitoring of the Groß Schönebeck stimulation experiment, in Jahrestagung der Deutschen Geophysikalischen Gessellschaft*, volume 64. GFZ, Berlin.

Bergmann, P., Schmidt-Hattenberger, C., Kiessling, D., Rücker, C., Labitzke, T., Henninges, J., Baumann, G., and Schütt, H. (2012). Surface-downhole electrical resistivity tomography applied to monitoring of CO2 storage at ketzin, germany. *Geophysics*, **77**(6), B253–B267.

Berre, I., Lien, M., and Mannseth, T. (2011). Identification of three-dimensional electric conductivity changes from time-lapse electromagnetic observations. *Journal of Computational Physics*, **230**(10), 3915–3928.

Besag, J., Green, P., Higdon, D., and Mengersen, K. (1995). Bayesian computation and stochastic systems. *Statistical science*, pages 3–41.

Beylich, A., Kolstrup, E., Linde, N., Pedersen, L., Thyrsted, T., Gintz, D., and Dynesius, L. (2003). Assessment of chemical denudation rates using hydrological measurements, water chemistry analysis and electromagnetic geophysical data. *Permafrost and Periglacial Processes*, **14**(4), 387–397.

Black, N., Zhdanov, M. S., *et al.* (2009). Monitoring of hydrocarbon reservoirs using marine CSEM method. In *SEG Technical Program Expanded Abstracts: 79th Annual International Meeting*, pages 850–854.

Bodin, T. and Sambridge, M. (2009). Seismic tomography with the reversible jump algorithm. *Geophysical Journal International*, **178**(3), 1411–1436.

Brace, W., Orange, A., and Madden, T. (1965). Effect of pressure on the electrical resistivity of water-saturated crystalline rocks. *Journal of Geophysical Research*, **70**, 5669–5678.

Brenguier, F., Shapiro, N. M., Campillo, M., Nercessian, A., and Ferrazzini, V. (2007). 3-D surface wave tomography of the Piton de la Fournaise volcano using seismic noise correlations. *Geophysical research letters*, **34**(2).

Brenguier, F., Shapiro, N. M., Campillo, M., Ferrazzini, V., Duputel, Z., Coutant, O., and Nercessian, A. (2008). Towards forecasting volcanic eruptions using seismic noise. *Nature Geoscience*, **1**(2), 126–130.

Brugger, J., Long, N., McPhail, D., and Plimer, I. (2005). An active amagmatic hydrothermal system: the Paralana hot springs, Northern Flinders Ranges, South Australia. *Chemical Geology*, **222**(1), 35–64.

Buland, A. and Kolbjørnsen, O. (2012). Bayesian inversion of CSEM and magnetotelluric data. *Geophysics*, **77**(1), E33–E42.

Cagniard, L. (1953). Basic theory of magnetotelluric method of geophysical prospecting. *Geophysics*, **18**, 605–635.

Cantwell, T. (1960). *Detection and analysis of low frequency magnetotelluric signals*. Ph.D. thesis, Massachusetts Institute of Technology.

Chave, A. D. and Jones, A. G. (2012). *The magnetotelluric method: Theory and practice*. Cambridge University Press.

Chave, A. D. and Thomson, D. J. (1989). Some comments on magnetotelluric response function estimation. *Journal of Geophysical Research: Solid Earth (1978–2012)*, **94**(B10), 14215–14225.

Chen, J., Hoversten, G. M., Vasco, D., Rubin, Y., and Hou, Z. (2007). A Bayesian model for gas saturation estimation using marine seismic AVA and CSEM data. *Geophysics*, **72**(2), WA85–WA95.

Chen, J., Kemna, A., and Hubbard, S. S. (2008). A comparison between Gauss-Newton and Markov-chain Monte Carlo–based methods for inverting spectral induced-polarization data for cole-cole parameters. *Geophysics*, **73**(6), F247–F259.

Chen, J., Hoversten, G. M., Key, K., Nordquist, G., and Cumming, W. (2012). Stochastic inversion of magnetotelluric data using a sharp boundary parameterization and application to a geothermal site. *Geophysics*, **77**(4), E265–E279.

Christen, J. A. and Fox, C. (2005). Markov chain Monte Carlo using an approximation. *Journal of Computational and Graphical Statistics*, **14**(4).

Claerbout, J. F. and Muir, F. (1973). Robust modeling with erratic data. *Geophysics*, **38**(5), 826–844.

Constable, S. C., Parker, R. L., and Constable, C. G. (1987). Occam's inversion: A practical algorithm for generating smooth models from electromagnetic sounding data. *Geophysics*, **52**(3), 289–300.

Cordua, K. S., Hansen, T. M., and Mosegaard, K. (2012). Monte Carlo full-waveform inversion of crosshole GPR data using multiple-point geostatistical a priori information. *Geophysics*, **77**(2), H19–H31.

Day-Lewis, F., Chen, Y., and Singha, K. (2007). Moment inference from tomograms. *Geophysical Research Letters*, **34**(22).

Day-Lewis, F. D., Harris, J. M., and Gorelick, S. M. (2002). Time-lapse inversion of crosswell radar data. *Geophysics*, **67**(6), 1740–1752.

deGroot Hedlin, C. and Constable, S. (1990). Occam's inversion to generate smooth, two-dimensional models from magnetotelluric data. *Geophysics*, **55**(12), 1613–1624.

Dietrich, C. and Newsam, G. N. (1997). Fast and exact simulation of stationary Gaussian processes through circulant embedding of the covariance matrix. *SIAM Journal on Scientific Computing*, **18**(4), 1088–1107.

Doetsch, J., Linde, N., and Binley, A. (2010). Structural joint inversion of time-lapse crosshole ERT and GPR traveltime data. *Geophysical Research Letters*, **37**(24), L24404.

Dosso, S. and Oldenburg, D. (1991). Magnetotelluric appraisal using simulated annealing. *Geophysical Journal International*, **106**(2), 379–385.

d'Ozouville, N., Auken, E., Sorensen, K., Violette, S., De Marsily, G., Deffontaines, B., and Merlen, G. (2008). Extensive perched aquifer and structural implications revealed by 3D resistivity mapping in a Galapagos volcano. *Earth and Planetary Science Letters*, **269**(3), 518–522.

Efendiev, Y., Datta-Gupta, A., Ginting, V., Ma, X., and Mallick, B. (2005). An efficient two-stage Markov chain Monte Carlo method for dynamic data integration. *Water Resources Research*, **41**(12).

Egbert, G. D. and Booker, J. R. (1986). Robust estimation of geomagnetic transfer functions. *Geophysical Journal International*, **87**(1), 173–194.

Egbert, G. D. and Kelbert, A. (2012). Computational recipes for electromagnetic inverse problems. *Geophysical Journal International*, **189**(1), 251–267.

Ellis, R. and Oldenburg, D. (1994). Applied geophysical inversion. *Geophysical Journal International*, **116**(1), 5–11.

Everett, M. and Schultz, A. (1993). Two-dimensional nonlinear magnetotelluric inversion using a genetic algorithm. *Journal of Geomagnetism and Geoelectricity*, **45**(9), 1013–1026.

Everett, M. E. (2013). *Near-surface applied geophysics*. Cambridge University Press.

Falgàs, E., Ledo, J., Marcuello, A., and Queralt, P. (2009). Monitoring freshwater-seawater interface dynamics with audiomagnetotelluric data. *Near Surface Geophysics*, **7**(5-6), 391–399.

Farquharson, C. G. (2007). Constructing piecewise-constant models in multidimensional minimum-structure inversions. *Geophysics*, **73**(1), K1–K9.

Farquharson, C. G. and Oldenburg, D. W. (1998). Non-linear inversion using general measures of data misfit and model structure. *Geophysical Journal International*, **134**(1), 213–227.

Fisher, G. and LeQuang, B. (1981). Topography and minimization of the standard deviation in one-dimensional magnetotelluric. *Geophys. JR Astron. Soc*, **67**, 257–278.

Fitterman, D. V. and Stewart, M. T. (1986). Transient electromagnetic sounding for groundwater. *Geophysics*, **51**(4), 995–1005.

Franke, A., Börner, R.-U., and Spitzer, K. (2007). Adaptive unstructured grid finite element simulation of two-dimensional magnetotelluric fields for arbitrary surface and seafloor topography. *Geophysical Journal International*, **171**(1), 71–86.

Gallardo, L. A. and Meju, M. A. (2004). Joint two-dimensional DC resistivity and seismic travel time inversion with cross-gradients constraints. *Journal of Geophysical Research*, **109**(B3).

Gelman, A. and Rubin, D. B. (1992). Inference from iterative simulation using multiple sequences. *Statistical science*, pages 457–472.

Girard, J.-F., Coppo, N., Rohmer, J., Bourgeois, B., Naudet, V., and Schmidt-Hattenberger, C. (2011). Time-lapse CSEM monitoring of the Ketzin (Germany) CO2 injection using 2× MAM configuration. *Energy Procedia*, **4**, 3322–3329.

Goldstein, M. and Strangway, D. (1975). Audio-frequency magnetotellurics with a grounded electric dipole source. *Geophysics*, **40**(4), 669–683.

Grandis, H., Menvielle, M., and Roussignol, M. (1999). Bayesian inversion with Markov chains I. the magnetotelluric one-dimensional case. *Geophysical Journal International*, **138**(3), 757–768.

Grandis, H., Menvielle, M., and Roussignol, M. (2002). Thin-sheet electromagnetic inversion modeling using Monte Carlo Markov Chain (MCMC) algorithm. *Earth, Planets and Space*, **54**(5), 511–522.

Guo, R., Dosso, S. E., Liu, J., Dettmer, J., and Tong, X. (2011). Non-linearity in Bayesian 1-D magnetotelluric inversion. *Geophysical Journal International*, **185**(2), 663–675.

Habashy, T. M., Groom, R. W., and Spies, B. R. (1993). Beyond the Born and Rytov approximations: A nonlinear approach to electromagnetic scattering. *Journal of Geophysical Research: Solid Earth (1978–2012)*, **98**(B2), 1759–1775.

Hasting, M., Albaric, J., Oye, V., Reid, P., Messeiller, M., Llanos, E., Malin, P., Shalev, E., Hogg, M., and Alvarez, M. (2011). Real-time induced seismicity monitoring during wellbore stimulation at Paralana-2 South Australia.

Hastings, W. K. (1970). Monte Carlo sampling methods using Markov chains and their applications. *Biometrika*, **57**(1), 97–109.

Hautot, S., Tarits, P., Perrier, F., Tarits, C., and Trique, M. (2002). Groundwater electromagnetic imaging in complex geological and topographical regions: A case study of a tectonic boundary in the French Alps. *Geophysics*, **67**(4), 1048–1060.

Holland, J. (1992). *Adaptation in natural and artificial systems*. MIT Press, Cambridge, MA.

Hou, Z., Rubin, Y., Hoversten, G. M., Vasco, D., and Chen, J. (2006). Reservoir-parameter identification using minimum relative entropy-based Bayesian inversion of seismic AVA and marine CSEM data. *Geophysics*, **71**(6), O77–O88.

House, L. (1987). Locating microearthquakes induced by hydraulic fracturing in crystalline rock. *Geophysical Research Letters*, **14**(9), 919–921.

Hubbard, S. S. and Rubin, Y. (2005). Introduction to hydrogeophysics. In *Hydrogeophysics*, pages 3–21. Springer.

Jackson, D. D. (1976). Most squares inversion. *Journal of Geophysical Research*, **81**(5), 1027–1030.

Jackson, J. D. (1962). *Classical electrodynamics*, volume 3. Wiley New York etc.

Jeffreys, H. (1998). *The theory of probability*. Oxford University Press.

Jougnot, D. and Revil, A. (2010). Thermal conductivity of unsaturated clay-rocks. *Hydrology and Earth System Sciences*, **14**(1), 91–98.

Kalscheuer, T. and Pedersen, L. B. (2007). A non-linear truncated SVD variance and resolution analysis of two-dimensional magnetotelluric models. *Geophysical Journal International*, **169**(2), 435–447.

Kalscheuer, T., Pedersen, L. B., and Siripunvaraporn, W. (2008). Radiomagnetotelluric two-dimensional forward and inverse modelling accounting for displacement currents. *Geophysical Journal International*, **175**(2), 486–514.

Kalscheuer, T., Juanatey, M. D. l. Á. G., Meqbel, N., and Pedersen, L. B. (2010). Non-linear model error and resolution properties from two-dimensional single and joint inversions of direct current resistivity and radiomagnetotelluric data. *Geophysical Journal International*, **182**(3), 1174–1188.

Kang, S., Seol, S. J., and Byun, J. (2012). A feasibility study of CO2 sequestration monitoring using the mCSEM method at a deep brine aquifer in a shallow sea. *Geophysics*, **77**(2), E117–E126.

Kappler, K., Morrison, H. F., and Egbert, G. (2010). Long-term monitoring of ULF electromagnetic fields at Parkfield, California. *Journal of Geophysical Research*, **115**(B4).

Karaoulis, M., Kim, J.-H., and Tsourlos, P. (2011). 4D active time constrained resistivity inversion. *Journal of Applied Geophysics*, **73**(1), 25–34.

Kass, R. E. and Raftery, A. E. (1995). Bayes factors. *Journal of the American Statistical Association*, **90**(430), 773–795.

Kemna, A., Kulessa, B., and Vereecken, H. (2002). Imaging and characterisation of subsurface solute transport using electrical resistivity tomography (ERT) and equivalent transport models. *Journal of Hydrology*, **267**(3), 125–146.

Key, K. and Weiss, C. (2006). Adaptive finite-element modeling using unstructured grids: The 2D magnetotelluric example. *Geophysics*, **71**(6), G291–G299.

Khan, A. and Mosegaard, K. (2002). An inquiry into the lunar interior: A nonlinear inversion of the Apollo lunar seismic data. *Journal of Geophysical Research*, **107**(E6), 3–1.

Khan, A., Mosegaard, K., Williams, J., and Lognonné, P. (2004). Does the moon possess a molten core? Probing the deep lunar interior using results from LLR and Lunar Prospector. *Journal of Geophysical Research*, **109**(E9).

Khan, A., Connolly, J., and Olsen, N. (2006). Constraining the composition and thermal state of the mantle beneath Europe from inversion of long-period electromagnetic sounding data. *Journal of Geophysical Research*, **111**(B10).

Kim, J.-H., Yi, M.-J., Park, S.-G., and Kim, J. G. (2009). 4-D inversion of DC resistivity monitoring data acquired over a dynamically changing earth model. *Journal of Applied Geophysics*, **68**(4), 522–532.

Kirkpatrick, S., Gellat, C. J., and Vecchi, M. (1983). Optimization by simulated annealing. *Science*, **220**, 671–680.

LaBrecque, D. J. and Yang, X. (2001). Difference inversion of ERT data: A fast inversion method for 3-D in situ monitoring. *Journal of Environmental & Engineering Geophysics*, **6**(2), 83–89.

Laloy, E. and Vrugt, J. A. (2012). High-dimensional posterior exploration of hydrologic models using multiple-try DREAM (ZS) and high-performance computing. *Water Resources Research*, **48**(1).

Laloy, E., Linde, N., and Vrugt, J. (2012). Mass conservative three-dimensional water tracer distribution from Markov chain Monte Carlo inversion of time-lapse ground-penetrating radar data. *Water Resources Research*, **48**(7), W07510.

Last, B. and Kubik, K. (1983). Compact gravity inversion. *Geophysics*, **48**(6), 713–721.

Lesmes, D. P. and Friedman, S. P. (2005). Relationships between the electrical and hydrogeological properties of rocks and soils. In *Hydrogeophysics*, pages 87–128. Springer.

Lien, M. and Mannseth, T. (2008). Sensitivity study of marine CSEM data for reservoir production monitoring. *Geophysics*, **73**(4), F151–F163.

Linde, N. (2014). Falsification and corroboration of conceptual hydrological models using geophysical data. *Wiley Interdisciplinary Reviews: Water*, **1**(2), 151–171.

Linde, N. and Pedersen, L. (2004a). Characterization of a fractured granite using radiomagnetotelluric (RMT) data. *Geophysics*, **69**(5), 1155–1165.

Linde, N. and Pedersen, L. B. (2004b). Evidence of electrical anisotropy in limestone formations using the RMT technique. *Geophysics*, **69**(4), 909–916.

Linde, N. and Vrugt, J. A. (2013). Distributed soil moisture from crosshole ground-penetrating radar travel times using stochastic inversion. *Vadose Zone Journal*, **12**(1).

Linde, N., Binley, A., Tryggvason, A., Pedersen, L., and Revil, A. (2006). Improved hydrogeophysical characterization using joint inversion of cross-hole electrical resistance and ground-penetrating radar traveltime data. *Water Resources Research*, **42**(12), W04410.

Liu, J. S., Liang, F., and Wong, W. H. (2000). The multiple-try method and local optimization in Metropolis sampling. *Journal of the American Statistical Association*, **95**(449), 121–134.

Lochbühler, T., Breen, S. J., Detwiler, R. L., Vrugt, J. A., and Linde, N. (2014). Probabilistic electrical resistivity tomography of a CO2 sequestration analog. *Journal of Applied Geophysics*.

Mackie, R. L., Madden, T. R., and Wannamaker, P. E. (1993). Three–dimensional magnetotelluric modeling using difference equations — Theory and comparisons to integral equation solutions. *Geophysics*, **58**, 215–226.

Malinverno, A. (2000). A Bayesian criterion for simplicity in inverse problem parametrization. *Geophysical Journal International*, **140**(2), 267–285.

Malinverno, A. (2002). Parsimonious Bayesian Markov chain Monte Carlo inversion in a nonlinear geophysical problem. *Geophysical Journal International*, **151**(3), 675–688.

Malinverno, A. and Briggs, V. A. (2004). Expanded uncertainty quantification in inverse problems: Hierarchical bayes and empirical bayes. *Geophysics*, **69**(4), 1005–1016.

Martí, A. (2014). The role of electrical anisotropy in magnetotelluric responses: From modelling and dimensionality analysis to inversion and interpretation. *Surveys in Geophysics*, **35**(1), 179–218.

Maurer, H., Holliger, K., and Boerner, D. E. (1998). Stochastic regularization: Smoothness or similarity? *Geophysical Research Letters*, **25**(15), 2889–2892.

Meju, M. and Hutton, V. (1992). Iterative most-squares inversion: application to magnetotelluric data. *Geophysical journal international*, **108**(3), 758–766.

Menke, W. (1989). Geophysical data analysis: discrete inverse theory. *Academic Press*, **260**.

Metropolis, N. and Ulam, S. (1949). The Monte Carlo method. *Journal of the American Statistical Association*, **44**(247), 335–341.

Metropolis, N., Rosenbluth, A. W., Rosenbluth, M. N., Teller, A. H., and Teller, E. (1953). Equation of state calculations by fast computing machines. *The Journal of Chemical Physics*, **21**(6), 1087–1092.

Metz, B., Davidson, O., De Coninck, H., Loos, M., Meyer, L., *et al.* (2005). Carbon dioxide capture and storage.

Miller, C. R., Routh, P. S., Brosten, T. R., and McNamara, J. P. (2008). Application of time-lapse ERT imaging to watershed characterization. *Geophysics*, **73**(3), G7–G17.

Minsley, B. J. (2011). A trans-dimensional Bayesian Markov chain Monte Carlo algorithm for model assessment using frequency-domain electromagnetic data. *Geophysical Journal International*, **187**(1), 252–272.

Minsley, B. J., Ajo-Franklin, J., Mukhopadhyay, A., and Morgan, F. D. (2011). Hydrogeophysical methods for analyzing aquifer storage and recovery systems. *Groundwater*, **49**(2), 250–269.

Mosegaard, K. and Tarantola, A. (1995). Monte Carlo sampling of solutions to inverse problems. *Journal of Geophysical Research*, **100**(B7), 12431–12447.

Muñoz, G. (2014). Exploring for geothermal resources with electromagnetic methods. *Surveys in Geophysics*, **35**(1), 101–122.

Nabighian, M. N. and Corbett, J. D. (1988). *Electromagnetic Methods in Applied Geophysics: Applications, part A and part B*. Society of Exploration Geophysics.

Nelder, C. (2009). The end of fossil fuel.

Neumann, N., Sandiford, M., and Foden, J. (2000). Regional geochemistry and continental heat flow: implications for the origin of the South Australian heat flow anomaly. *Earth and Planetary Science Letters*, **183**(1), 107–120.

Newman, G. A. and Alumbaugh, D. L. (2000). Three-dimensional magnetotelluric inversion using non-linear conjugate gradients. *Geophysical journal international*, **140**(2), 410–424.

Nix, B. (2005). Radiomagnetotellurik-messungen zur räumlichen und zeitlichen ausbreitung ines grundwasser-tracers.

Nocedal, J. and Wright, S. J. (2006). *Conjugate gradient methods*. Springer.

Oldenburg, D. W. and Li, Y. (1999). Estimating depth of investigation in DC resistivity and IP surveys. *Geophysics*, **64**(2), 403–416.

Orange, A., Key, K., and Constable, S. (2009). The feasibility of reservoir monitoring using time-lapse marine CSEM. *Geophysics*, **74**(2), F21–F29.

Paal, G. (1965). Ore prospecting based on VLF-radio signals. *Geoexploration*, **3**(3), 139–147.

Palacky, G. (1988). Resistivity characteristics of geologic targets. *Electromagnetic methods in applied geophysics*, **1**, 53–129.

Parker, R. (1994). Geophysical inverse theory.

Peacock, J. R., Thiel, S., Reid, P., and Heinson, G. (2012). Magnetotelluric monitoring of a fluid injection: Example from an enhanced geothermal system. *Geophysical Research Letters*, **39**(18).

Peacock, J. R., Thiel, S., Heinson, G. S., and Reid, P. (2013). Time-lapse magnetotelluric monitoring of an enhanced geothermal system. *Geophysics*, **78**(3), B121–B130.

Pedersen, L. B. and Engels, M. (2005). Routine 2D inversion of magnetotelluric data using the determinant of the impedance tensor. *Geophysics*, **70**(2), G33–G41.

Pedersen, L. B., Bastani, M., and Dynesius, L. (2005). Groundwater exploration using combined controlled-source and radiomagnetotelluric techniques. *Geophysics*, **70**(1), G8–G15.

Pérez-Flores, M. A. and Schultz, A. (2002). Application of 2-D inversion with genetic algorithms to magnetotelluric data from geothermal areas. *Earth, Planets and Space*, **54**(5), 607–616.

Petratherm (2012).

Pilkington, M. (1997). 3-D magnetic imaging using conjugate gradients. *Geophysics*, **62**(4), 1132–1142.

Portniaguine, O. and Zhdanov, M. S. (1999). Focusing geophysical inversion images. *Geophysics*, **64**(3), 874–887.

Ramirez, A. L., Nitao, J. J., Hanley, W. G., Aines, R., Glaser, R. E., Sengupta, S. K., Dyer, K. M., Hickling, T. L., and Daily, W. D. (2005). Stochastic inversion of electrical resistivity changes using a Markov Chain Monte Carlo approach. *Journal of Geophysical Research*, **110**(B2).

Ray, A. and Key, K. (2012). Bayesian inversion of marine CSEM data with a trans-dimensional self parametrizing algorithm. *Geophysical Journal International*, **191**(3), 1135–1151.

Reid, P., Messeiller, M., and Llanos, E. (2011). Paralana EGS project-findings from the fracture stimulation. Australian Geothermal Conference.

Ren, Z., Kalscheuer, T., Greenhalgh, S., and Maurer, H. (2013). A goal-oriented adaptive finite-element approach for plane wave 3-D electromagnetic modelling. *Geophysical Journal International*, **194**(2), 700–718.

Robert, C. P. and Casella, G. (2004). *Monte Carlo statistical methods*, volume 319. Citeseer.

Roberts, G. O. and Rosenthal, J. S. (2007). Coupling and ergodicity of adaptive Markov chain Monte Carlo algorithms. *Journal of Applied Probability*, pages 458–475.

Rodi, W. and Mackie, R. L. (2001). Nonlinear conjugate gradients algorithm for 2-D magnetotelluric inversion. *Geophysics*, **66**(1), 174–187.

Rodi, W. L. (1976). A technique for improving the accuracy of finite element solutions for magnetotelluric data. *Geophys. J. R. Astr. Soc.*, **44**, 483–506.

Rosas Carbajal, M., Linde, N., and Kalscheuer, T. (2012). Focused time-lapse inversion of radio and audio magnetotelluric data. *Journal of Applied Geophysics*, **84**, 29–38.

Rosas-Carbajal, M., Linde, N., Kalscheuer, T., and Vrugt, J. A. (2014). Two-dimensional probabilistic inversion of plane-wave electromagnetic data: methodology, model constraints and joint inversion with electrical resistivity data. *Geophysical Journal International*, **196**(3), 1508–1524.

Rubin, Y. (2003). *Applied stochastic hydrology*. Oxford Univ. Press, New York.

Rubin, Y. and Hubbard, S. S. (2005). *Hydrogeophysics*, volume 50. Springer.

Sacchi, M. D. and Ulrych, T. J. (1996). Estimation of the discrete fourier transform, a linear inversion approach. *Geophysics*, **61**(4), 1128–1136.

Sambridge, M. and Mosegaard, K. (2002). Monte Carlo methods in geophysical inverse problems. *Reviews of Geophysics*, **40**(3), 3–1.

Scales, J. A. and Sneider, R. (1997). To Bayes or not to Bayes? *Geophysics*, **62**(4), 1045–1046.

Schamper, C., Rejiba, F., Tabbagh, A., and Spitz, S. (2011). Theoretical analysis of long offset time-lapse frequency domain controlled source electromagnetic signals using the method of moments: Application to the monitoring of a land oil reservoir. *Journal of Geophysical Research*, **116**(B3).

Sen, M. K. and Stoffa, P. L. (1995). *Global optimization methods in geophysical inversion*. Elsevier.

Sen, P. N. and Goode, P. A. (1992). Influence of temperature on electrical conductivity on shaly sands. *Geophysics*, **57**(1), 89–96.

Sen, P. N., Goode, P. A., and Sibbit, A. (1988). Electrical conduction in clay bearing sandstones at low and high salinities. *Journal of Applied Physics*, **63**(10), 4832–4840.

Shearer, P. (1997). Improving local earthquake locations using the L1 norm and waverform cross correlation: Application to the Whittier Narrows, California, aftershock sequence. *J. Geophys. Res.*, **102**(B4), 8269–8283.

Siripunvaraporn, W. and Egbert, G. (2000). An efficient data-subspace inversion method for 2-D magnetotelluric data. *Geophysics*, **65**(3), 791–803.

Siripunvaraporn, W., Egbert, G., Lenbury, Y., and Uyeshima, M. (2005). Three-dimensional magnetotelluric inversion: data-space method. *Physics of the Earth and Planetary Interiors*, **150**(1), 3–14.

Smith, J. T. and Booker, J. R. (1991). Rapid inversion of two-and three-dimensional magnetotelluric data. *Journal of Geophysical Research*, **96**(B3), 3905–3922.

Tarantola, A. (1987). *Inverse problem theory*. Elsevier, Amsterdam.

Tarantola, A. (2005). *Inverse problem theory and methods for model parameter estimation*. SIAM.

Tarantola, A. and Valette, B. (1982). Inverse problems= quest for information. *Journal of Geophysics*, **50**(3), 150–170.

Tarits, P., Jouanne, V., Menvielle, M., and Roussignol, M. (1994). Bayesian statistics of non-linear inverse problems: example of the magnetotelluric 1-D inverse problem. *Geophysical Journal International*, **119**(2), 353–368.

Teague, M. R. (1980). Image analysis via the general theory of moments. *JOSA*, **70**(8), 920–930.

Tester, J. W., Anderson, B. J., Batchelor, A., Blackwell, D., DiPippo, R., Drake, E., Garnish, J., Livesay, B., Moore, M., Nichols, K., *et al.* (2006). The future of geothermal energy. *Massachusetts Institute of Technology*, **358**.

Tezkan, B. (1999). A review of environmental applications of quasi-stationary electromagnetic techniques. *Surveys in Geophysics*, **20**(3-4), 279–308.

Tikhonov, A. (1963). Resolution of ill-posed problems and the regularization method (in Russian). In *Soviet Math. Dokl.*, volume 5, pages 1035–1038.

Ueberhuber, C. W. (1997). *Numerical Computation 1: Methods, Software, and Analysis.*, volume 16. Springer.

USGS (2004).

Vasco, D., Daley, T. M., and Bakulin, A. (2014). Utilizing the onset of time-lapse changes: a robust basis for reservoir monitoring and characterization. *Geophysical Journal International*, page ggt526.

Vasseur, G. and Weidelt, P. (1977). Bimodal electromagnetic induction in non-uniform thin sheets with an application to the northern pyrenean induction anomaly. *Geophysical Journal International*, **51**(3), 669–690.

Vilamajó, E., Queralt, P., Ledo, J., and Marcuello, A. (2013). Feasibility of monitoring the Hontomín (Burgos, Spain) CO2 storage site using a deep EM source. *Surveys in Geophysics*, **34**(4), 441–461.

Virieux, J., Flores-Luna, C., and Gibert, D. (1994). Asymptotic theory for diffusive electromagnetic imaging. *Geophysical Journal International*, **119**(3), 857–868.

Von Neumann, J. (1951). Various techniques used in connection with random digits. *Applied Math Series*, **12**(36-38), 1.

Vozoff, K. (1991). *Electromagnetic methods in applied geophysics*. SEG.

Vrugt, J. A., Ter Braak, C. J., Clark, M. P., Hyman, J. M., and Robinson, B. A. (2008). Treatment of input uncertainty in hydrologic modeling: Doing hydrology backward with Markov chain Monte Carlo simulation. *Water Resources Research*, **44**(12).

Vrugt, J. A., Ter Braak, C., Diks, C., Robinson, B. A., Hyman, J. M., and Higdon, D. (2009). Accelerating Markov chain Monte Carlo simulation by differential evolution with self-adaptive randomized subspace sampling. *International Journal of Nonlinear Sciences and Numerical Simulation*, **10**(3), 273–290.

Wannamaker, P. E. (1991). Advances in three-dimensional magnetotelluric modeling using integral equations. *Geophysics*, **56**(11), 1716–1728.

Wannamaker, P. E. (1997). Tensor CSAMT survey over the Sulphur Springs thermal area, Valles Caldera, New Mexico, United States of America, Part II: Implications for CSAMT methodology. *Geophysics*, **62**(2), 466–476.

Wannamaker, P. E. and Stodt, J. A. (1987). A stable finite element solution for two–dimensional magnetotelluric modelling. *Geophys. J. R. Astr. Soc.*, **88**, 277–296.

Wannamaker, P. E., Hohmann, G. W., and SanFilipo, W. A. (1984). Electromagnetic modeling of three-dimensional bodies in layered earths using integral equations. *Geophysics*, **49**(1), 60–74.

Weidelt, P. (1999). 3-D conductivity models: implications of electrical anisotropy. *Three-dimensional electromagnetics*, **7**, 119–137.

Wirianto, M., Mulder, W., and Slob, E. (2010). A feasibility study of land CSEM reservoir monitoring in a complex 3-D model. *Geophysical Journal International*, **181**(2), 741–755.

www.e-education.edu (2014).

www.swissworld.org (2014).

www.world-nuclear.org (2014).

www.wrd.org (2007).

Zhang, P., Roberts, R., and Pedersen, L. (1987). Magnetotelluric strike rules. *Geophysics*, **52**(3), 267–278.

Zhdanov, M. and Hursan, G. (2000). 3D electromagnetic inversion based on quasi-analytical approximation. *Inverse Problems*, **16**(5), 1297.

Zhdanov, M. S. and Fang, S. (1996). Quasi-linear approximation in 3-D electromagnetic modeling. *Geophysics*, **61**(3), 646–665.

Zhdanov, M. S., Lee, S. K., and Yoshioka, K. (2006). Integral equation method for 3D modeling of electromagnetic fields in complex structures with inhomogeneous background conductivity. *Geophysics*, **71**(6), G333–G345.

Zhdanov, M. S., Endo, M., Black, N., Spangler, L., Fairweather, S., Hibbs, A., Eiskamp, G., and Will, R. (2013). Electromagnetic monitoring of CO2 sequestration in deep reservoirs. *first break*, **31**(2).

Zonge, K. L., Hughes, L. J., and Nabighian, M. N. (1991). *Electromagnetic methods in applied geophysics*. Society of Exploration Geophysicists, SEG.

Zyserman, F. I. and Santos, J. E. (2000). Parallel finite element algorithm for three–dimensional magnetotelluric modelling. *Journal of Applied Geophysics*, **44**, 337–351.

Acknowledgements

It is an honour to thank a number of people who have helped me during my doctoral studies. First of all I would like to thank Niklas Linde, my PhD supervisor. Niklas has been an excellent guide throughout. He has always been there when I needed him, and at the same time he has given me freedom to pursue my own ideas. He has been very supportive and kind when I was going through difficult times. I also thank Niklas for all the trouble he has gone through to convince the UNIL admission department to accept me as a PhD student.

I would also like to thank the rest of my PhD committee: Prof. Juan José Ledo from University of Barcelona, Prof. Klaus Holliger from Lausanne and the President of the committee Prof. René Véron. Together with Niklas, they motivated very interesting discussions about my work during the private defence of my PhD.

Special thanks to Thomas Kalscheuer for all the interesting discussions, the very detailed reviews of my papers, and his unconditional interest in my work. Thomas has also shared with me his code EMILIA, whose tidy and elegant structure allowed me to incorporate all the changes I needed for my first paper. Thanks also to the rest of my co-authors for the fruitful collaborations: Jasper Vrugt, Fabio Zyserman, Jared Peacock and Stephan Thiel.

I am thankful to Philippe Logean, for his help with the computer cluster. Philippe has helped me to compile, debug and implement together so many codes that I lost the count.

Thanks to the people involved in peer-reviewing the individual chapters of this thesis for their constructive comments, including Juan José Ledo from University of Barcelona, Amir Khan from ETH Zurich, Jinsong Chen from Berkeley Lab and other anonymous reviewers. This research was supported by the Swiss National Science Foundation to whom I express my gratitude.

I had a great time enjoying the friendship and the inspiring environment of my colleagues at University of Lausanne. Thanks for the beers, the sports and all the laughs, and for making this place such a good working environment. Special thanks to the ones I shared my office with: Jehanne who helped me so much with French-to-Spanish translations in the beginning, Caro and Laureline for the dancing sessions, Santi and Nico for making me feel Argentina was not that far away, and Ricardo for making us work from time to time.

I am grateful for all the friends I made during these years. A special thought goes to Ani and Ger for giving me shelter during my first two weeks in Lausanne and soon after becoming my family in Switzerland. Thanks to Damien who has been my colleague, friend, and partner and who has been great at all of those.

Finally, thanks to my family and my friends for supporting me in good but also difficult times. I dedicate this work to my father, who passed away during my second year in Lausanne. I would not have got this far without his love and support.